

**The Investigation of Lanthanum Strontium Chromite (LSC) Based Perovskite  
Anodes for Solid Oxide Fuel Cells (SOFCs)**

by

Yifei Sun

A thesis submitted in partial fulfillment of the requirements for the degree of

Doctor of Philosophy

in

Chemical Engineering

Department of Chemical and Materials Engineering  
University of Alberta

© Yifei Sun, 2016

## Abstract

Solid oxide fuel cells (SOFC) can be fueled with diverse raw natural gases which usually contain a carbon source and significant amount of H<sub>2</sub>S. Both of them severely deactivate the Ni-YSZ cermet anode materials and limit their wide applications. Therefore, the potential anode catalysts developed must have excellent coke and sulfur resistances in addition to meeting the general requirements for an anode, including good electrochemical performance as well as chemical stability.

The lanthanum chromite perovskite oxide with desirable mechanical and chemical stabilities in redox atmosphere has been regarded as a good interconnection material candidate for SOFCs stack; it is also a suitable and potential anode material for replacing Ni-YSZ. Thorough investigation has shown that its derivative of strontium doped lanthanum chromite (LSC) exhibited higher electrical conductivity. In order to further enhance the catalytic activity of LSC, this study adopted several strategies to fabricate a series of LSC based perovskite oxide anodes and comprehensively investigated their electrochemical and structural properties.

A series of Ce-doped La<sub>0.7</sub>Sr<sub>0.3</sub>Fe<sub>0.5</sub>Cr<sub>0.5</sub>O<sub>3-δ</sub> (Ce-LSFC) perovskite anode catalysts was firstly synthesized by a modified glycine combustion method. The characterization results illustrate that the pure perovskite structure without formation of CeO<sub>2</sub> could be obtained when the content of Ce is ≤ 10%. Compared with the La<sub>0.7</sub>Sr<sub>0.3</sub>Fe<sub>0.5</sub>Cr<sub>0.5</sub>O<sub>3-δ</sub> anode, the Ce-LSFC anode not only showed much higher catalytic activity toward the oxidation of syngas with less carbon deposition, but also

displayed better regeneration from coking. The enhanced performance was attributed to the more available oxygen vacancies in the lattice and better oxygen mobility after doping with Ce.

It is widely known that chemical deposition is one of the most widely used ways to enhance the electrochemical performance of perovskite oxide anodes for SOFCs. However, the anodes produced still have unsatisfactory activity and experience regenerability problems. For the first time, Ni doped LSC perovskite oxides with A-site deficiency (A-LSCNi) were prepared and it was found that the in-situ exsolution of nano Ni could be facilitated after introducing A-site deficiency. The fuel cell with an A-LSCNi anode showed maximum power density of 460 mW/cm<sup>2</sup> in 5000 ppm H<sub>2</sub>S-H<sub>2</sub> compared to only 135 mW/cm<sup>2</sup> for a fuel cell with a stoichiometric LSCNi anode. Besides, the fuel cell also demonstrates desirable redox stability in sour fuel. The introduction of A-site deficiency can help the formation of highly-mobile oxygen vacancies and remarkably enhance the reducibility of Ni nanoparticles, leading to a significant increase in electronic conductivity and catalytic activity simultaneously.

Based on the results mentioned above, the generality of this idea was extended and Ni and Fe doped A-site deficient LaSrCrO<sub>3</sub> perovskite (A-LSC) bimetallic anode material was successfully fabricated, on which the exsolution of uniformly dispersed nano Ni-Fe alloy could be *in-situ* formed in reducing atmosphere. The prepared bimetallic anode catalyst with highly catalytically active nano Ni-Fe alloy exhibited much improved electrochemical performance in sour hydrocarbon fuel (5000 ppm H<sub>2</sub>S-

syngas) and better carbon deposition resistance compared to the monometallic anode catalyst.

Furthermore, the application of this type of functional catalyst has been extended to the field of heterogeneous catalysis. For the first time, an iron doped lanthanum strontium chromite with A-site deficiency (A-LSCFe) was fabricated and utilized as an effective bi-functional catalyst for the growth of multiple-walls carbon nanotubes (MWCNTs) and solid oxide fuel cells (SOFCs). The introduction of A-site deficiency significantly facilitates the in-situ exsolution of nano iron particles on which a considerable amount of MWCNTs is grown. The material was also used as the anode catalyst for SOFCs and proved to be a very effective anode catalyst in comparison with the stoichiometric material (sto-LSCFe). The exsolved nano iron particles on A-LSCFe provide many more active sites for the oxidation reaction of the fuel, leading to sharp enhancement of the electrochemical performance of the cell. It was also discovered that the growth of MWCNTs with high electron conductivity leads to a further improvement on the electricity output.

The desirable performance and functionality of this series of catalysts offer a bright potential for its promising application in various research fields.

## Preface

Chapter 1 is the introduction, which contains the background knowledge and operation theory of solid oxide fuel cells.

Chapter 2 of the thesis is the literature review for the reported potential anode materials for solid oxide fuel cells.

Chapter 3 briefly introduces the methodologies utilized for the accomplishment of this thesis as well as the various characterization parameters.

Chapter 4 of the thesis has been published as Yi-Fei Sun, Jian-Hui Li, Kart T. Chuang, Jing-Li Luo, Electrochemical performance and carbon deposition resistance of Ce-doped  $\text{La}_{0.7}\text{Sr}_{0.3}\text{Fe}_{0.5}\text{Cr}_{0.5}\text{O}_{3-\delta}$  anode materials for solid oxide fuel cells fed with syngas, *Journal of Power Sources*, 2015, 274(0): 483-487.

Chapter 5 of the thesis has been published as Yifei Sun, Jianhui Li, Yimin Zeng, Babak Shalchi Amirkhiz, Mengni Wang, Yashar Behnamian and Jingli Luo, A-site deficient perovskite: the parent for *in situ* exsolution of high-active, regenerable nano-particles as SOFCs anode, *Journal of Material Chemistry A*, 2015, 3: 11048-11056

Chapter 6 of the thesis has been published as Yi-Fei Sun, Jian-Hui Li, Lin Cui, Bin Hua, Shao-Hua Cui, Jian Li and Jing-Li Luo, A-site-deficiency facilitated *in situ* growth of bimetallic Ni-Fe nano-alloys: a novel coking-tolerant fuel cell anode catalyst : a novel carbon deposition tolerant anode catalyst for solid oxide fuel cells, *Nanoscale*, 2015, 7: 11173-11181.

Chapter 7 of the thesis has been published as Yi-Fei Sun, Jian-Hui Li, Meng-Ni Wang, Bin Hua, Jian Li, and Jing-Li Luo, A-site deficient chromite perovskite with *in-situ* exsolution of nano Fe : A promising bi-functional catalyst bridging between growth of CNTs and SOFCs, Journal of Material Chemistry A, 2015, 3: 14625-14630.

Appendix I of the thesis has been published as Yi-Fei Sun, Jian-Hui Li, Shao-Hua Cui, Karl T. Chuang, Jing-Li Luo, Carbon Deposition and Sulfur Tolerant  $\text{La}_{0.4}\text{Sr}_{0.5}\text{Ba}_{0.1}\text{TiO}_3\text{-La}_{0.4}\text{Ce}_{0.6}\text{O}_{1.8}$  Anode Catalysts for Solid Oxide Fuel Cells, Electrochimica Acta 2015, 151(0): 81-88.

For all of the above work, the coauthors, Meng-Ni Wang and Lin Cui who were summer students helped fabricate some of the samples. The coauthors, Yimin Zeng, Babak Shalchi Amirkhiz, Yashar Behnamian, and Shao-Hua Cui helped conduct part of the SEM and TEM analyses. Dr. Jing Shen helped conduct the  $\text{H}_2$ -TPR experiments. The coauthors, Dr. Bin Hua and Dr. Jian Li helped the analysis of data. Dr. Jing-Li Luo, my supervisor, accompanied with Dr. Jian-Hui Li, provided valuable discussions and feedback on construction of experimental devices, experimental plan and results. She also gave me extremely valuable suggestions and helped in writing, revising and preparing conference presentations, manuscripts and the thesis work. The rest of the research work, such as designing and conducting all the experiments, data collection, data analysis, as well as writing the manuscripts and the thesis are my contributions.

## Acknowledgements

The completion of this thesis was only possible with the selfless help from many individuals and organizations. Here I would like to express my most sincere respect and gratitude to all of them.

First of all, I really hope to express my special thanks to my supervisor, Dr. Jingli Luo for all the academic and financial support she offered to me during the past three years. She taught me how to think of and investigate the scientific questions in the right way, which must benefit the rest of my life. Secondly, I hope to express my appreciation to the CSC program for its long-term financial support. Thirdly, I hope to express my deep appreciations to my supervisor committing members Drs. Thomas H. Etsell and Steven M. Kuznicki for their significant advice during my research progress.

Fourthly, my thanks are given to all the group members including Dr. Jianhui Li, Dr. Bin Hua, Dr. Min Chen, Dr. Shaohua Cui and Dr. Xinwen Zhou, Dr. Xianzhu Fu, Dr. Hong Luo, Yaqian Zhang, Subiao Liu, Xianzong Wang, for their helps, suggestions and discussions. Many thanks also go to Dr. Jing Shen, and scientists from the National Institute of Nanotechnology, University of Alberta, University of Calgary, Canmet Energy in Canada and Xiamen University in China, who helped me for the important characterization and significant data analysis of my samples. Last but not least, my special thanks are given to my parents and my wife Rio Chen who offer unconditional love encouraging me to overcome challenges in the future.

## Table of Contents

The Investigation of Lanthanum Strontium Chromite (LSC) Based Perovskite Anodes for Solid Oxide Fuel Cells (SOFCs) .....	错误!未定义书签。
Abstract .....	i
Preface .....	v
Acknowledgements .....	vii
Table of Contents .....	viii
List of Figures .....	xi
Chapter 1. Introduction.....	1
1.1 The Usage of Fossil Fuel.....	1
1.2 Fuel cell technology .....	3
1.2.1 Types of fuel cells .....	3
1.2.2 SOFCs.....	4
1.3 References .....	9
Chapter 2. Literature review of anode materials for SOFCs .....	11
2.1 Nickel-Based Cermet Anodes .....	11
2.2 Copper-Based Cermet Anodes .....	13
2.3 Perovskite Oxide Anodes .....	14
2.4 Challenges and Goals .....	17
2.5 References .....	18
Chapter 3. Experimental Methodology .....	22
3.1 Synthesis of Materials .....	22
3.2 Fabrication of the cell.....	22
3.3 Electrochemical Test of Anode Materials .....	24
3.4 Characterization of Anode Materials.....	24
Chapter 4. Electrochemical performance and carbon deposition resistance of Ce-doped $\text{La}_{0.7}\text{Sr}_{0.3}\text{Fe}_{0.5}\text{Cr}_{0.5}\text{O}_{3-\delta}$ anode materials for solid oxide fuel cells fed with syngas .....	28
4.1 Introduction .....	28
4.2 Experimental Procedure .....	28

4.3 Results and Discussion .....	29
4.4 Conclusions .....	38
4.5 References .....	39
Chapter 5. A-site deficient lanthanum strontium chromite: the parent for <i>in-situ</i> exsolution of highly-active and regenerable nano-Ni anode for solid oxide fuel cells (SOFCs) .....	41
5.1 Introduction .....	41
5.2 Experimental Procedures:.....	43
5.3 Results .....	43
5.4 Discussion .....	55
5.5 Conclusions .....	59
5.6 References .....	60
Chapter 6. <i>In-situ</i> growth of nano Ni-Fe alloy on A-site deficient Sr doped LaCrO <sub>3</sub> perovskite: A novel carbon deposition and sulfur tolerant anode for solid oxide fuel cells (SOFCs).....	65
6.1 Introduction .....	65
6.2 Experimental Procedure .....	68
6.3 Results .....	69
6.4 Discussion .....	83
6.5 References .....	86
Chapter 7. A-site deficient chromite perovskite with in-situ exsolution of nano Fe : A promising bi-functional catalyst bridging growth of CNTs and SOFCs .....	92
7.1 Introduction .....	92
7.2 Experimental Procedure .....	94
7.3 Results and discussion.....	94
7.4 Conclusions .....	106
7.5 References .....	107
Appendix I :Carbon Deposition and Sulfur Tolerant La <sub>0.4</sub> Sr <sub>0.5</sub> Ba <sub>0.1</sub> TiO <sub>3</sub> -La <sub>0.4</sub> Ce <sub>0.6</sub> O <sub>1.8</sub> Anode Catalysts for Solid Oxide Fuel Cell.....	111
Introduction .....	111
Experimental Procedures.....	114

Results and discussion.....	116
Conclusions .....	131
References.....	132
Bibliography.....	138

## List of Figures

Fig.1-1 The distribution of world energy consumption (Source: Energy Transitions by Cutler Cleveland).....	1
Fig.1-2 The Global Carbon Dioxide Emission from Fossil Fuel Burning.....	2
Fig.1-3 Schematic of SOFC working principle. ....	4
Fig.1-4 A typical I-V curve of fuel cell. ....	7
Fig.2-1 The pathways for syngas production and for coke formation [7].....	12
Fig.2-2 Unit cell of Perovskite oxide[11] .....	14
Fig.3-1 Photo of anode and cathode sides of the fabricated cell .....	23
Fig.3-2 Schematics of SOFCs setup[1].....	24
Fig.4-1 (a) XRD patterns and (b) the position of the (110) diffraction peak vs. x for Ce-LSFC with various concentrations of Ce. ....	30
Fig.4-2 (a) The O <sub>2</sub> -TPD profiles and (b) CO <sub>2</sub> production during TPO analyses for Ce-LSFC with various concentrations of Ce.....	32
Fig.4-3 (a) EIS results for the symmetrical half cells with various anodes in syngas at 800 °C (b) Regeneration tests of LSFC and 5Ce-LSFC in syngas at 800 °C.....	35
Fig.4-4 (a) The I-V and power density curves of SOFC with 5Ce-LSFC anode fed with syngas at 800 °C, (b) The corresponding EIS result and the equivalent circuit used for simulation of the cell, (c) The durability test of the fuel cell fed with syngas at 800 °C.....	37
Fig.5- 1 X-ray diffraction (XRD) patterns and calculated Gibbs free energy of reduction reaction for each element oxide in LSCNi perovskite. (a) XRD patterns of the various fresh and treated materials. Among them, 63LSCNi-15 was reduced in 5% H <sub>2</sub> /N <sub>2</sub> at 800 °C for 4 h and re-oxidized in air at 1300 °C for 3h. (b) XRD patterns of the fresh 63LSCNi-x with Ni contents, x%, of 5% to 20%. (c) The theoretical value of reduction Gibbs free energy for each element oxide in LSCNi-15 perovskite at 800 °C. The data are estimated using HSC 6.0 software. ....	45

Fig.5- 2 Thermogravimetric analysis (TGA), quantity of oxygen non-stoichiometry and characterizations of hydrogen temperature-programmed reduction (H<sub>2</sub>-TPR) of the various catalysts. (a) TGA curves of the fresh LSC, 73LSCNi-15 and 63LSCNi-15 measured in 5% H<sub>2</sub>/N<sub>2</sub> with a flow rate of 20 mL min<sup>-1</sup> from 100 °C to 900 °C at a heating rate of 20 °C min<sup>-1</sup>. (b) The quantity of oxygen non-stoichiometry determined based on the mass change during the TGA test. (c) H<sub>2</sub>-TPR curves of the fresh LSC, 73LSCNi-15 and 63LSCNi-15. All samples were treated with helium at 1000 °C for 30 min before TPR. The flow rate of 10% H<sub>2</sub>/Ar was 10 mL min<sup>-1</sup> and the temperature ramping rate was 10 °C min<sup>-1</sup>.....48

Fig.5- 3 Scanning electron microscopy (SEM), energy-dispersive X-ray spectroscopy (EDX), transmission electron microscopy (TEM), energy filtered TEM (EFTEM) and high angle annular dark field (HAADF) images for 63LSCNi-15 and 73LSCNi-15 samples. SEM images for (a) 63LSCNi-15 and (b) 73LSCNi-15 materials reduced at 800 °C for 4 h. (c) EDX analysis for point 5 and B of TEM image of 63LSCNi-15 on the left side of (c). (d) TEM micrograph of the exsolved nano-particle anchored on bulk material. (e) EFTEM image of a Ni particle. (f) HAADF image of a 63LSCNi-15 particle overlaid with EDX elemental map of Ni-highlighting nanoparticles. ....50

Fig.5- 4 Fuel cell performances with the various anodes in H<sub>2</sub> or 5000 ppm H<sub>2</sub>S-H<sub>2</sub>. Current density–voltage and power density curves for fuel cells with 63LSCNi-15 and 73LSCNi-15 anodes using (a) pure H<sub>2</sub> fuel and (b) 5000 ppm H<sub>2</sub>S-H<sub>2</sub> fuel at 800 °C. (c) EIS for the cells with 63LSCNi-15 and 73LSCNi-15 anodes fueled with 5000 ppm H<sub>2</sub>S-H<sub>2</sub> at 800 °C. (d) The redox test results for 63LSCNi-15-YSZ/YSZ/YSZ-LSCF fuel cell at 800 °C during four 26 h-cycles. In each cycle, the cell was treated with 5000 ppm H<sub>2</sub>S-H<sub>2</sub> for 24 h and then recovered via the in situ treatment of 5% O<sub>2</sub>/N<sub>2</sub> for 2 h (hatched period). Then the fuel was introduced again and the power density was measured after the introduction of fuel for 30 min. (e) The comparison of EIS results for the cell using 63LSCNi-15 anode before and after 4 redox cycle test in (d). ....54

Fig.5- 5 (a) XRD patterns for the materials with various concentrations of A-site or B-site deficiency. (b) The schematic of generation of oxygen vacancies and Ni exsolution process for perovskite with A-site deficiency. The simulated figure was drawn using ChemDraw 8.0. ....	58
Fig.6- 1 XRD patterns for (a) fresh anode materials and (b) reduced anode materials. All materials were reduced in 5% H <sub>2</sub> /N <sub>2</sub> at 800 °C for 4 h. ....	70
Fig.6- 2 . H <sub>2</sub> -TPR profiles for different anode materials. ....	72
Fig.6- 3 . Phase diagram of bimetallic Ni-Fe system <sup>34</sup> . ....	72
Fig.6- 4 TGA curves of the fresh LSCNi, LSCFe and LSCNi-Fe samples measured in 5% H <sub>2</sub> /N <sub>2</sub> . ....	73
Fig.6- 5 TECs of LSCNi-Fe and YSZ materials in air from 400 K to 1200 K. ....	74
Fig.6- 6 Electrical conductivities of various materials in air (a) and in 5%H <sub>2</sub> /N <sub>2</sub> (b) as a function of temperature. ....	76
Fig.6- 7 SEM images for the (a) LSCNi (b) LSCFe and (c) LSCNi-Fe materials reduced at 800oC for 4 h; (d) TEM micrograph of the exsolved nano-particle anchored to the bulk LSCNi-Fe material; (e) EDX analysis for points 1 and 2 on the TEM image shown in (d). (f) and (g) are the SEM images for the LSC materials reduced at 800 oC for 4 h and LSCNi-Fe material before reduction, respectively. ....	78
Fig.6- 8 (a) Current density vs. voltage and power density curves, and (b) electrochemical impedance spectra for fuel cells with LSCNi, LSCFe and LSCNi-Fe anodes using 5000 ppm H <sub>2</sub> S-H <sub>2</sub> fuel at 800 °C. ....	79
Fig.6- 9 (a) Current density vs. voltage and power density curves, and (b) electrochemical impedance spectra for fuel cells with an LSCNi-Fe anode using 5000 ppm H <sub>2</sub> S-syngas fuel at different temperatures. ....	81
Fig.6- 10 Electrochemical impedance spectra of a fuel cell with an LSCNi-Fe anode measured in 5000 ppm H <sub>2</sub> S-syngas between 750°C and 850°C under open-circuit conditions. Arrhenius plot of the resistances measured at different temperatures. ....	81
Fig.6- 11. TPO curves of various materials treated with syngas in 850°C for 24 h. ...	83

Fig 7- 1. XRD patterns of fresh (LSC, A-LSCFe and Sto-LSCFe) and reduced (Re-A-LSCFe) materials.....95

Fig 7- 2. H<sub>2</sub>-TPR results of sto-LSCFe and A-LSCFe materials.....97

Fig 7- 3. TGA results of sto-LSCFe and A-LSCFe materials .....98

Fig 7- 4. The comparison of SEM images of (a) reduced A-LSCFe and (b) Sto-LSCFe materials.....99

Fig 7- 5 SEM images of MWCNTs prepared by decomposition of CH<sub>4</sub> at 600 °C for 4h over pre-reduced (a) A-LSCFe and (b) sto-LSCFe..... 100

Fig 7- 6 TEM images of (a) CNTs with different diameters, (b) segment of a CNT, (c) Fe nano particle encapsulated within a CNT as well as its corresponding EDX scan results, and (d) CNTs composed of well graphitized layers. .... 102

Fig 7- 7 The I-V and power density curve of fuel cells with A-LSCFe and sto-LSCFe anodes in H<sub>2</sub> (a) and in CH<sub>4</sub> (b) at 800 °C, (c) with A-LSCFe anode fed with H<sub>2</sub> at different temperatures, (d) with A-LSCFe anode with and without CNT in H<sub>2</sub> at 700 °C, and (e) The corresponding EIS of the fuel cells with different treatments..... 105

## List of Symbols

MEA	Membrane electrode assembly
EIS	Electrochemical impedance spectra
SOFC	Solid oxide fuel cell
XRD	X-ray diffractometer
XPS	X-ray photoelectron spectroscopy
SEM	Scanning Electron Microscope
EDX	Energy-dispersive X-ray spectroscopy
EELS	Electron energy loss spectrometer
HAADF	High angle annular dark field
TGA	Thermogravimetric analysis
O <sub>2</sub> -TPD	Temperature-programmed desorption of oxygen
H <sub>2</sub> -TPR	Hydrogen temperature programmed reduction
TCD	Thermal conductivity detector
TECs	Thermal expansion coefficients
TPO	Temperature-programmed oxidation
DFT	Density functional theory
TPB	Triple phase boundary
GC	Gas chromatograph
PDF	Diffraction file number
PMMA	Polymethylmethacrylate

YSZ	Yttria-stabilized zirconia
APR	Activation polarization resistance
CCVD	Catalytic chemical vapor deposition
PEG	Polyethylene glycol
CNTs	Carbon nanotubes
MWCNTs	Multiple-walled carbon nanotubes
xCe-LSFC	$\text{La}_{0.7}\text{Sr}_{0.3}\text{Fe}_{0.5}\text{Cr}_{0.5-x}\text{Ce}_x\text{O}_{3-\delta}$
LSM	$\text{La}_{0.8}\text{Sr}_{0.2}\text{MnO}_3$
LSC	$\text{La}_{0.7}\text{Sr}_{0.3}\text{CrO}_{3-\xi}$
73LSCNi <sub>x</sub>	$\text{La}_{0.7}\text{Sr}_{0.3}\text{Cr}_{1-x}\text{Ni}_x\text{O}_{3-\xi}$
63LSCNi <sub>x</sub>	$\text{La}_{0.6}\text{Sr}_{0.3}\text{Cr}_{1-x}\text{Ni}_x\text{O}_{3-\xi}$
LSGM	$\text{La}_{0.8}\text{Sr}_{0.2}\text{Ga}_{0.8}\text{Mg}_{0.2}\text{O}_3$
LSCNi	$(\text{La}_{0.7}\text{Sr}_{0.3})(\text{Cr}_{0.85}\text{Ni}_{0.15})\text{O}_{3-\xi}$
LSCFe	$(\text{La}_{0.7}\text{Sr}_{0.3})(\text{Cr}_{0.85}\text{Fe}_{0.15})\text{O}_{3-\xi}$
LSCNi-Fe	$(\text{La}_{0.7}\text{Sr}_{0.3})(\text{Cr}_{0.85}(\text{Ni}_{0.15}\text{Fe}_{0.15}))\text{O}_{3-\xi}$
A-LSCFe	$\text{La}_{0.6}\text{Sr}_{0.3}\text{Cr}_{0.85}\text{Fe}_{0.15}\text{O}_{3-\xi}$
sto-LSCFe	$\text{La}_{0.7}\text{Sr}_{0.3}\text{Cr}_{0.85}\text{Fe}_{0.15}\text{O}_{3-\xi}$
LSBT	$\text{La}_{0.4}\text{Sr}_{0.6-x}\text{Ba}_x\text{TiO}_3$
LDC	$\text{La}_{0.4}\text{Ce}_{0.6}\text{O}_{1.8}$
LSBT-LDC	$\text{La}_{0.4}\text{Ce}_{0.6}\text{O}_{1.8}$ impregnated $\text{La}_{0.4}\text{Sr}_{0.6-x}\text{Ba}_x\text{TiO}_3$

## Chapter 1. Introduction

### 1.1 The Usage of Fossil Fuel

In the world that we live in, the increasing demand for energy has inspired the need to seek alternative energy sources. Despite the rapid development of solar cells and other advanced technologies to generate energy, most of the energy supplies come from fossil fuels(1). Fig. 1-1 shows the distribution of world energy consumption (Source: Energy Transitions by Cutler Cleveland). Hydroelectric power, nuclear power and renewable energy only supply less than 15% of the total consumption in the world. The use of non-renewable energy sources, such as natural gas, coal and oil, is predominant at present and fossil fuels will remain as the main source of energy, not only at present, but also in the coming future.

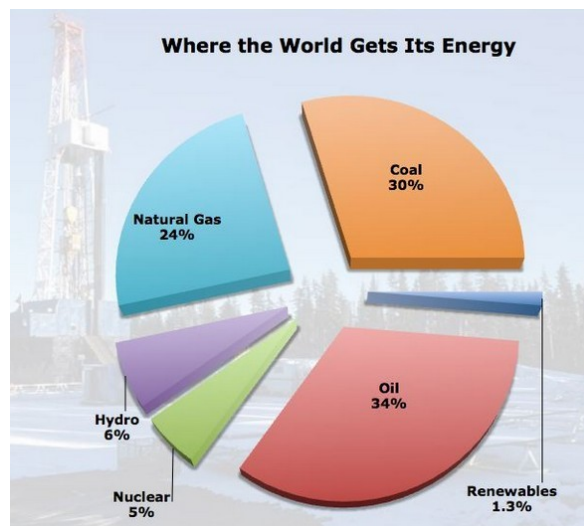


**Fig.1-1 The distribution of world energy consumption (Source: Energy Transitions by Cutler Cleveland).**

While fossil fuel remains as the main stream of energy usage, the environmental problems generated by the usage of fossil fuel are one of the great challenges today. Figure.1-2 shows that the emission of carbon dioxide from burning fossil fuels has maintained its increasing trend for the past several hundred years. In recent years, CO<sub>2</sub> emissions from fossil fuels grew at a rate of 2.6% each year, hitting an all-time high peak amount of 9.7 billion tons in 2012(2). As a result, the problem of global warming is gradually changing the ecological system and may irreversibly damage the environment worldwide.

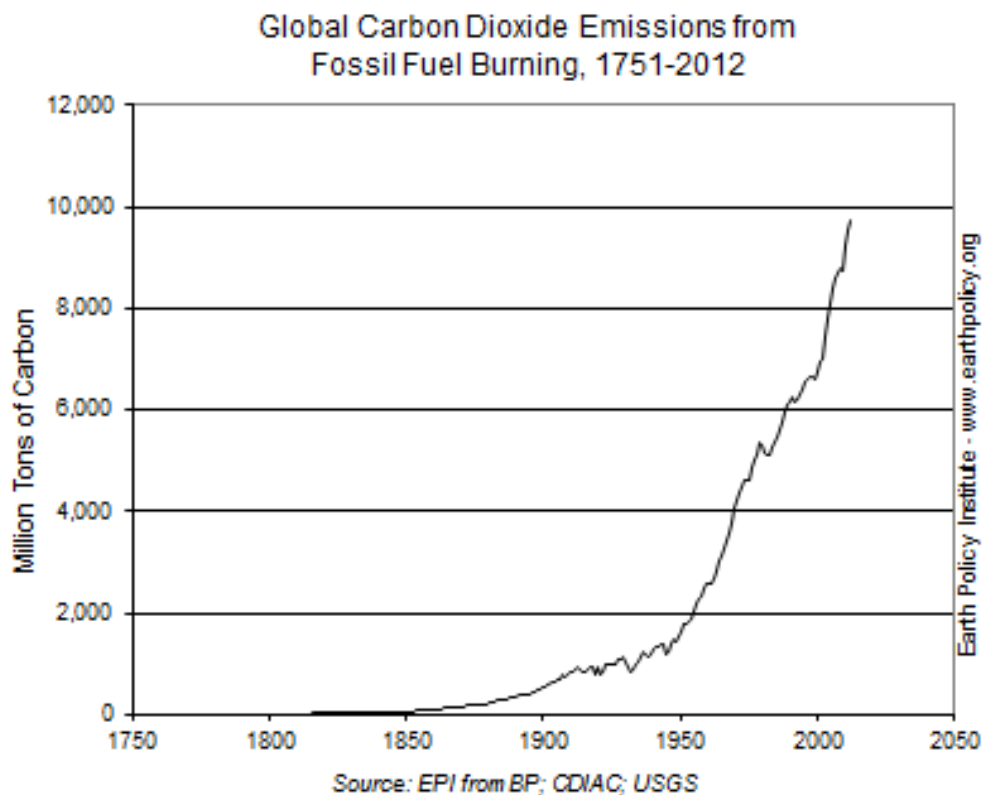


**Fig.1-2 The Global Carbon Dioxide Emission from Fossil Fuel Burning.**

Currently, the direct combustion of fossil fuel in power plants is the main method to generate electricity. However, efficiencies are as low as 40%, limited by

thermodynamic equilibrium. Most of the chemical energy of the fossil fuel is wasted in the form of low grade heat(3).

Since fossil fuels are not renewable and the combustion of fossil fuels is associated with negative environmental consequences, it has become imperative to develop other environmentally friendly technologies that may offer higher efficiency in the utilization of fossil fuels.

## 1.2 Fuel cell technology

Fuel cells are electrochemical devices that can directly convert the chemical energy of fuel into electricity beyond the limitation of the Carnot Cycle. Ideally, as long as the fuel and oxidant are continuously fed, the device will be able to generate electricity continuously. For fuel cells using hydrocarbon as fuel, the emission of carbon dioxide could be reduced by 20-60% because of their highly efficient conversion of the fuel to electricity(4).

### 1.2.1 Types of fuel cells

The fuel cell could be classified into five types(5), including polymer electrolyte membrane, alkaline, phosphoric acid, molten carbonate and solid oxide fuel cells (6).

### 1.2.2 SOFCs

The solid oxide fuel cell (SOFC) is one of the most promising technologies, which operates in the temperature range of 500-1000 °C. Such high operating temperature gives the SOFCs more fuel flexibility(7), e.g., CO could be utilized as fuel to generate electricity. In addition, the high operating temperature could also allow the usage of non-precious metal catalysts, which will significantly reduce the operating cost.

Fig. 1-3 illustrates the schematic of a typical SOFC working principle. The basic SOFCs consist of a dense electrolyte separating two electrodes, connected through an external circuit. For the oxygen-ion conducting SOFCs, the oxygen at the cathode chamber is ionized and oxygen ions then transport to the anode chamber where the oxygen-ions react with the fuel to produce electrons and reaction products. These electrons will be transported to the cathode through the external circuit as electricity.

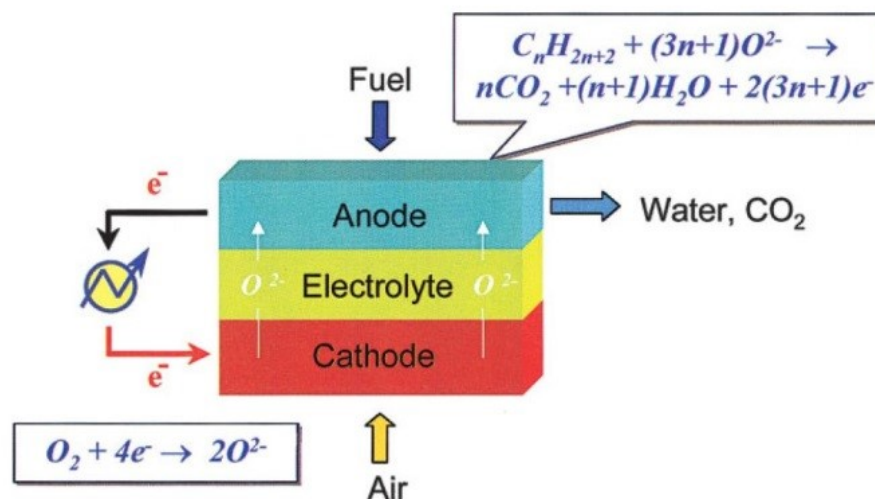


**Fig.1-3 Schematic of SOFC working principle.**

### 1.2.2.1 Thermodynamics

Like other types of energy converters, the useful energy in a SOFC system can be extracted from the chemical reaction and further converted into electricity. The electrical work is equal to the total change in the Gibbs free energy within a closed reaction system.

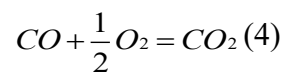
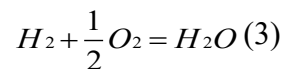
$$W_{electrical} = -\Delta G \quad (1)$$

The maximum electrical energy of the system could be expressed as follows:

$$W_{electrical} = nEF \quad (2)$$

where  $W_{electrical}$  is the available output electrical work and  $n$  is the total number of moles of electrons participating in the reaction,  $F$  is the Faraday constant and  $E$  is the reversible cell potential.

Ideally, the reactions occurring on the anode of the fuel cell fed by syngas are:



There are three factors which will influence the reversible potentials: temperature (T), pressure (P), and concentration (C).

Defining  $E_T$  as the reversible cell voltage at an arbitrary temperature  $T$ , we have:

$$E_T = E_o + \frac{\Delta S}{nF} (T - T_o) \quad (5)$$

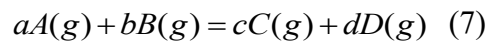
For most fuel cell reactions,  $\Delta S$  is negative. Therefore, the reversible fuel cell voltages will decrease with increasing temperature.

Similarly, at a constant temperature, we can also get the expression as below:

$$\frac{dE}{dP} = -\frac{\Delta V}{nF} \quad (6)$$

Therefore, if the volume change within the system is negative, when the pressure increases, the reversible potential will increase.

Consider the following general electrochemical reaction occurring at constant temperature and pressure,



The Gibbs free energy change is related to the standard reference state,  $\Delta G^\circ$

$$\Delta G = \Delta G^\circ + RT \ln \frac{(p_C / p^\circ)^c (p_D / p^\circ)^d}{(p_A / p^\circ)^a (p_B / p^\circ)^b} \quad (8)$$

where R is the gas constant and p is the partial pressure of each component involved in the reaction on the anode or cathode.

#### 1.2.2.2 Efficiency of Fuel Cell

For all energy generation devices, the thermal efficiency is defined as follows:

$$\varepsilon_{thermo} = \frac{work}{heat} = \frac{\Delta G}{\Delta H} \quad (9)$$

As seen above, the thermal efficiency of the fuel cell is only limited by the cell thermodynamic parameters. That is why most of the fuel cell reactions have relatively higher efficiencies than other types of thermal cycles including combustion.

Another channel for loss of efficiency comes from the loss of voltage; we define the efficiency of voltage as follows:

$$\varepsilon_{voltage} = \frac{V_{working}}{V_{theoretical}} \quad (10)$$

The loss of voltage consists of three parts: activation overpotential, concentration polarization and ohmic loss across the cell. The details of each will be discussed in the next section.

### 1.2.2.3 Fuel cell Performance

The curve in Fig. 1-4 illustrates the relationship between voltage and current for a single fuel cell, which is regarded as one of the most important methods for evaluating the performance of the cell.

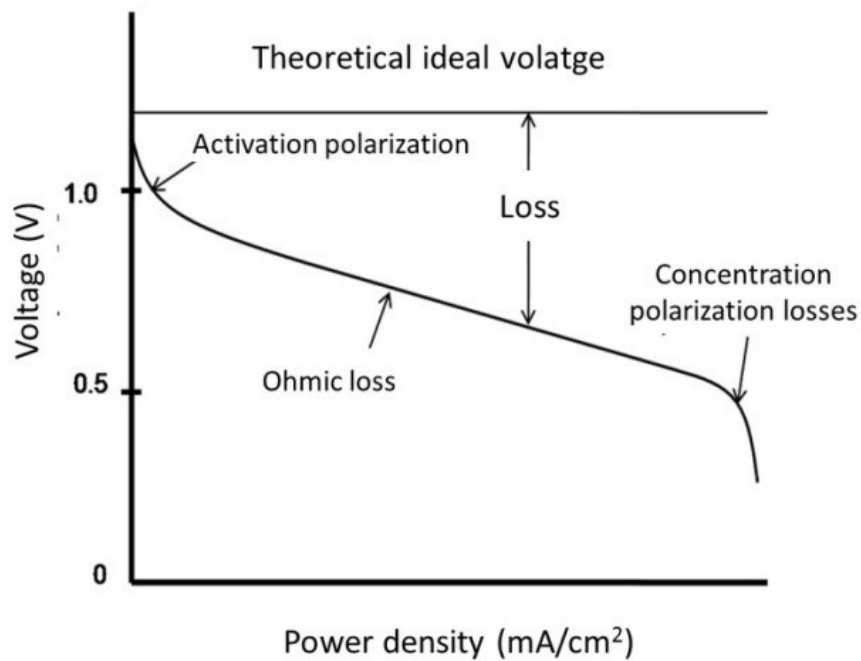


**Fig.1-4 A typical I-V curve of fuel cell.**

Because of the three polarization effects, the voltage will decrease with increasing current. Therefore, the minimization of the three polarization effects helps enhance the performance significantly.

### 1.2.2.3.1 Activation Losses

In the small beginning region of the I-V curve, the activation polarization plays a predominant role for the loss of voltage. The reactions occurring on the electrode are all reversible. At zero current, the reactions reach thermodynamic equilibrium; the forward and reverse reaction rates are identical and the net current density is equal to zero.  $j_{\text{forward}} = j_{\text{backward}} = j_0$ ,  $j_0$  is defined as the exchange current density.

The Butler-Volmer equation describes the relationship between current density,  $j$ , and activation polarization potential,  $\eta_{\text{act}}$  (6).

$$j = j_0 \exp\left\{\frac{\alpha \eta_{\text{act}} zF}{RT}\right\} - j_0 \exp\left\{-\frac{(1-\alpha) \eta_{\text{act}} zF}{RT}\right\} \quad (11)$$

where  $\alpha$  is the transfer coefficient, describing how the change in the electrical potential across the reaction interface affects the size of the forward versus backward activation barriers.

### 1.2.2.3.2 Ohmic Losses

The ohmic losses are mainly due to the resistances of the electrode and electrolyte when the ions and electrons flow through them during the reaction. The ohmic polarization obeys Ohm's Law (8):

$$\eta_{\text{ohm}} = IR_{\text{total}} \quad (11)$$

The contributions from the electrolyte and electrode could be considered separately. To reduce the overall ohmic losses, firstly, it is necessary to reduce the

thickness of the electrolyte, which is the main parameter contributing to the total resistance. Secondly, efforts should be devoted to enhancing the ionic and electronic conductivities of the electrode to minimize its contribution to ohmic losses.

#### 1.2.2.3.3 Concentration Losses

At the end region of the I-V curve, the concentration polarization losses dominate. At very high reaction rate, the fuel transportation rate is not fast enough to provide enough reactants at the reaction sites and, likewise, the slow removal of reaction products from the electrode adds to concentration losses as well.

The rate of mass transport to the electrode surface is described by Fick's first law:

$$i = \frac{nFD(C_B - C_S)}{\delta} \quad (12)$$

where D is the diffusion coefficient of the reactant,  $C_B$  is the concentration in the bulk and  $C_S$  is the concentration at the surface, and  $\delta$  is the thickness of the diffusion layer. When  $C_S$  is equal to zero, the limiting current ( $j_l$ ) is a measure of the maximum transportation rate of the reactant. The concentration polarization can be expressed as:

$$\eta_{conc} = -\frac{RT}{nF} \ln\left(1 - \frac{j}{j_l}\right) \quad (13)$$

## 1.3 References

1. Cowin PI, Petit CTG, Lan R, Irvine JTS, Tao S. Recent Progress in the Development of Anode Materials for Solid Oxide Fuel Cells. *Advanced Energy Materials*. 2011;1(3):314-32.

2. Adams EE. Carbon Emissions. Earth Policy Institute. 2013.
3. Ormerod RM. Solid oxide fuel cells. Chemical Society reviews. 2003;32(1):17-28.
4. Wang W, Ran R, Su C, Guo Y, Farrusseng D, Shao Z. Ammonia-mediated suppression of coke formation in direct-methane solid oxide fuel cells with nickel-based anodes. Journal of Power Sources. 2013;240:232-40.
5. Roushanafshar M, Luo J-L, Chuang KT, Sanger AR. Effect of Hydrogen Sulfide on Electrochemical Oxidation of Syngas for SOFC Applications. ECS Transactions. 2011;35(1):2799-804.
6. Services EG. Fuel Cell Handbook (Fifth Edition) 2000.
7. Alzate-Restrepo V, Hill JM. Effect of anodic polarization on carbon deposition on Ni/YSZ anodes exposed to methane. Applied Catalysis A: General. 2008;342(1-2):49-55.
8. Jung HY, Hong K-S, Jung H-G, Kim H, Kim H-R, Son J-W, et al. SOFCs with Sc-Doped Zirconia Electrolyte and Co-Containing Perovskite Cathodes. Journal of The Electrochemical Society. 2007;154(5):B480.

## Chapter 2. Literature review of anode materials for SOFCs

As discussed above, the activation polarization behavior on both anode and cathode make significant contributions to the total loss of the SOFC performance. An efficient anode material should meet several requirements such as high electronic and ionic conductivities, catalytic activity for fuel oxidation, stability on successive reducing/oxidizing (redox) cycles, thermal and chemical stabilities, and compatibility with electrolytes, including matched thermal expansion coefficients (TEC) (1).

Because any electrochemical reaction occurs only at the interface between electronic conductor and ionic conductor, it is significant to maximize the triple phase boundary (TPB) where the fuel gas, electronic conductor and ionic conductor meet, which can increase the catalytic performance of the anode and decrease the polarization.

### 2.1 Nickel-Based Cermet Anodes

The Ni/YSZ cermet anode material was first developed in 1964. In the next several decades, it always played a predominant role in the SOFCs industry because a cermet consisting of Ni and YSZ has many unique properties as an ideal candidate for the anode material(2). It has high electronic conductivity because of the extremely high conductivity of the metal Ni, reasonable ionic conductivity and high catalytic activity for hydrogen oxidation. For example, Mailley(3) developed NiO-YSZ anode materials using 3% $\text{H}_2\text{O}$ - $\text{H}_2$  as the fuel and obtained a power density of 500  $\text{mW}/\text{cm}^2$  at 800 °C.

It is well known that one of the biggest merits of SOFCs is the flexibility of fuels. However, Ni catalysts suffer carbon deposition, especially when using hydrocarbon fuels(4). Fig. 2-1 shows possible pathways for syngas production and for coke formation on a Ni-YSZ anode. The TEM images also proved the presence of carbon nano fibers (whisker carbon) and graphite carbon on the materials.

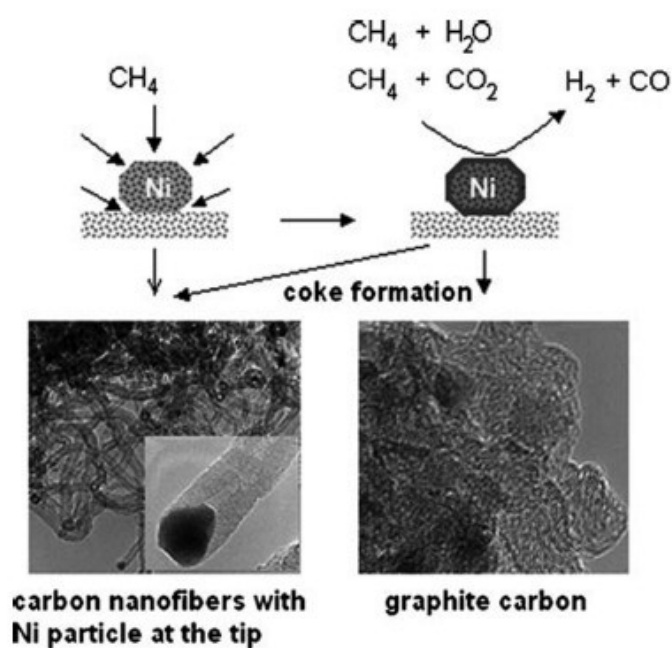


**Fig.2-1 The pathways for syngas production and for coke formation [7].**

Several strategies have been fostered in order to alleviate carbon deposition on Ni-YSZ materials. Restrepo proved that the application of discharging current could reduce the amount of deposited carbon(5). In addition, Shao found that the addition of NH<sub>3</sub> could decrease coke formation rates on Ni-YSZ anodes (2). However, all these methods would significantly reduce the overall efficiency and increase the cost for fabrication.

Another major problem for Ni-YSZ is sulfur poisoning. The raw natural fuel always contains certain amounts of contaminant such as hydrogen sulfide. The

degradation of anode is reversible when the concentration of  $\text{H}_2\text{S}$  is as low as 15 ppm (6). At a concentration as high as 100 ppm, the formation of  $\text{Ni}_3\text{S}_2$  was confirmed and the deactivation of the anode was not recoverable (7).

## 2.2 Copper-Based Cermet Anodes

Cu-based material appears to be a promising anode candidate. It meets the requirements of not catalyzing carbon formation on the anode and being stable at the operating temperature as well as under various oxygen partial pressures. Cu-cermet anodes operate at intermediate temperatures due to the relatively lower melting temperature of Cu. Besides, a variety of bimetallic anodes with better thermal stability, such as Cu-Ni[19], Cu-Cr[20] and Cu-Co[21], has been evaluated at higher operating temperatures.

Cu doped with  $\text{CeO}_2$  was also employed as an anode material.(8). It also exhibits mixed electronic and ionic conductivity in reducing atmospheres due to the reduction of  $\text{Ce}^{4+}$  to  $\text{Ce}^{3+}$ .

However, Cu is a very poor fuel oxidation catalyst. Thus, the performance of Cu-based cermet anodes was unsatisfactory in general. It has been reported that the addition of precious metals such as Ru(9), Pt and Rh(10) by impregnation could noticeably enhance the performance, but the high cost of fabrication can hardly justify its wide application.

## 2.3 Perovskite Oxide Anodes

### 2.3.1 The Crystal Structure of Perovskite

The ideal perovskites have the general formula of  $ABX_3$ , in which the X could be oxygen, chlorine and fluorine. For perovskite oxides, the total charge of A and B is +6. In this structure, an A-site ion, at the corners of the lattice, is usually an alkaline earth or rare earth element. B site ions, at the center of the lattice, could be 3d, 4d, and 5d transitional metal elements (shown in Fig 2-2).

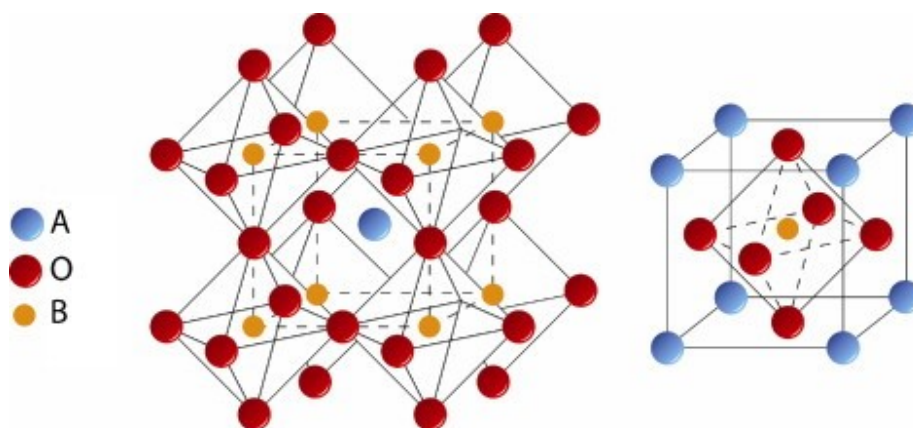


**Fig.2-2 Unit cell of Perovskite oxide[11]**

Generally, the composition of perovskite oxides is quite flexible that numerous compounds can be created through certain amount of doping in A or B sites. Their chemical structures will be distorted and their electrochemical properties, such as electronic conductivity and electrocatalytic capability, could be changed as well. The Goldschmidt tolerance factor could be used as an indicator for the stability and distortion of crystal structures:

$$t = \frac{r_A + r_0}{\sqrt{2}(r_B + r_0)}$$

Oxygen ion vacancies or interstitials could be created by replacing the parent cations with cations of lower or higher valences, via doping. For example, in the case of the perovskite oxide, SrTiO<sub>3</sub>, the substitution of Sr<sup>2+</sup> with La<sup>3+</sup> results in the compensation of charge to meet the charge neutrality. In a reducing atmosphere, the oxygen in the lattice could then be removed to generate oxygen vacancies, resulting in an increase of ionic conductivity. So far, three types of perovskite structure anode materials have been developed which showed promising performance and acceptable level of stability using hydrocarbon as the feed.

### 2.3.2 Vanadium Based Perovskite

The La<sub>x</sub>Sr<sub>1-x</sub>VO<sub>3-δ</sub> anode material has proven to be a good candidate for SOFCs using H<sub>2</sub>S-containing fuel because it shows good resistance against sulfur(11). Danilovic (12) found that Ce<sub>0.9</sub>Sr<sub>0.1</sub>VO<sub>3</sub> showed good performance using H<sub>2</sub>S-containing CH<sub>4</sub> as the fuel, although its performance in CH<sub>4</sub> alone was not as satisfactory. Also, the La<sub>0.8</sub>Sr<sub>0.2</sub>Cr<sub>0.97</sub>V<sub>0.03</sub>O<sub>3</sub> (13) exhibited low activity for the CH<sub>4</sub> reforming reaction, but its activity increased sharply upon increasing the reaction temperature.

### 2.3.3 Titanium Based Perovskite

Maria et al.(14) adjusted the ratio of different elements in  $\text{La}_x\text{Sr}_{1-x}\text{TiO}_3$  ( $x= 0.1, 0.2, 0.3, 0.35$  and  $0.4$ ) perovskite and found the important effect of oxidation reduction cycling on their thermal and electrical properties. The study on Y-doped  $\text{SrTiO}_3$  ( $\text{SY}_x\text{T}$ ) ( $x = 0.02, 0.04, 0.06, 0.08, 0.10$ ) prepared by solid state method (15) showed that yttrium doping could improve the conductivity and sinterability of the material. It was also reported that the La and Cr doped  $\text{SrTiO}_3$  (LSCT) could improve the conductivity and decrease the activation energy for conduction in a reducing atmosphere (16).

### 2.3.4 Chromium Based Perovskite

$\text{LaCrO}_3$  was firstly utilized as the interconnect material for SOFCs. Then, Sr-doped  $\text{LaMnO}_3$  was developed and proven to be a good candidate for the cathode material. However, this material is not stable in reducing atmospheres. Therefore, further element substitution is necessary in order to enhance its conductivity, activity and stability. The  $\text{La}_{0.75}\text{Sr}_{0.25}\text{Cr}_{0.5}\text{Fe}_{0.5}\text{O}_{3-\delta}$  was fabricated and showed good catalytic activity for the oxidation of  $\text{H}_2$  and methane (17). The lanthanum chromites doped with strontium and ruthenium developed by Sauvet(18) exhibited good stability using hydrocarbon fuel for 200 hours under operating conditions. No carbon deposition and degradation could be detected. However, the  $\text{La}_{0.8}\text{Sr}_{0.2}\text{Cr}_{0.97}\text{V}_{0.03}\text{O}_3$  anode material reported by Primdahl (19) showed that the polarization resistance value was an order

of magnitude higher than that of Ni-YSZ materials, and its stability in reducing atmospheres was poor as well.

#### 2.4 Challenges and Goals

A variety of fuels have been examined as energy source candidates for SOFCs, such as natural gas, diesel fuel, alcohols, ammonia and syngas. Syngas is a relatively cheap, but quite important fuel. Normally, the raw syngas always contains trace amounts of H<sub>2</sub>S stemming from the sulfur in fossil fuels. As a result, the traditional metal-based anode catalysts, such as Ni-YSZ cermet, are easily poisoned even though the concentration of H<sub>2</sub>S is as low as 100 ppm. Also the degradation of SOFC is usually irreversible (20). Another main problem of using syngas as fuel for SOFCs is carbon deposition on the anode (21). Although certain amounts of carbon deposition could enhance the electronic conductivity to some extent(22), the active sites will be blocked by carbon and the chemical structure of the catalyst would be damaged. Therefore, the electrochemical performance will be negatively affected to a great extent, and the overall efficiency of the fuel cell system will significantly decrease.

As the alternative anode materials substituting for Ni-YSZ cermets, the perovskite oxides with good ionic conductivity exhibit much better sulfur and carbon deposition resistance. However, their electronic conductivity as well as this catalytic activity are still unsatisfying. Therefore, developing carbon/sulfur tolerant perovskite oxide anode

catalysts with good electrochemical performance for the SOFCs fed with syngas becomes the primary mission of the present study.

The primary goal of this study is to investigate and develop strontium doped lanthanum chromite based (LSC) perovskite oxide SOFC anode materials which meet the targeted requirements of high performance as well as S and C resistances. Suitable anode materials are synthesized by different methods. The structural and electrochemical properties of these materials are characterized by various characterization technologies. Furthermore, the electrochemical performances of the fuel cells with different prepared anodes are tested in sweet and sour fuels. In addition, carbon deposition resistance and sulfur tolerance of the optimized anode materials are studied in detail.

## 2.5 References

1. Ge X-M, Chan S-H, Liu Q-L, Sun Q. Solid Oxide Fuel Cell Anode Materials for Direct Hydrocarbon Utilization. *Advanced Energy Materials*. 2012;2(10):1156-81.
2. Wang W, Su C, Wu Y, Ran R, Shao Z. Progress in Solid Oxide Fuel Cells with Nickel-Based Anodes Operating on Methane and Related Fuels. *Chemical reviews*. 2013.
3. Mailley SC, Kelaidopoulou A, Siddle A, Dicks AL, Holtappels P, Hatchwell CE, et al. Electrocatalytic activity of a  $\text{Gd}_2\text{Ti}_{0.6}\text{Mo}_{1.2}\text{Sc}_{0.2}\text{O}_{7-\delta}$  anode towards

- hydrogen and methane electro-oxidation in a solid oxide fuel cell. *Ionics*. 2000;6(5-6):331-9.
4. Hui S, Roller J, Yick S, Zhang X, Decès-Petit C, Xie Y, et al. A brief review of the ionic conductivity enhancement for selected oxide electrolytes. *Journal of Power Sources*. 2007;172(2):493-502.
  5. Alzate-Restrepo V, Hill JM. Effect of anodic polarization on carbon deposition on Ni/YSZ anodes exposed to methane. *Applied Catalysis A: General*. 2008;342(1-2):49-55.
  6. Choi YM, Compson C, Lin MC, Liu M. A mechanistic study of H<sub>2</sub>S decomposition on Ni- and Cu-based anode surfaces in a solid oxide fuel cell. *Chemical Physics Letters*. 2006;421(1-3):179-83.
  7. Grgicak CM, Green RG, Du W-F, Giorgi JB. Synthesis and Characterization of NiO-YSZ Anode Materials: Precipitation, Calcination, and the Effects on Sintering. *Journal of the American Ceramic Society*. 2005;88(11):3081-7.
  8. Gross MD, Vohs JM, Gorte RJ. A study of thermal stability and methane tolerance of Cu-based SOFC anodes with electrodeposited Co. *Electrochimica Acta*. 2007;52(5):1951-7.
  9. Cimenti M, Hill JM. Direct utilization of ethanol on ceria-based anodes for solid oxide fuel cells. *Asia-Pacific Journal of Chemical Engineering*. 2009;4(1):45-54.

10. McIntosh S, Vohs JM, Gorte RJ. Effect of Precious-Metal Dopants on SOFC Anodes for Direct Utilization of Hydrocarbons. *Electrochemical and Solid-State Letters*. 2003;6(11):A240.
11. Aguilar L, Zha S, Cheng Z, Winnick J, Liu M. A solid oxide fuel cell operating on hydrogen sulfide (H<sub>2</sub>S) and sulfur-containing fuels. *Journal of Power Sources*. 2004;135(1–2):17-24.
12. Danilovic N, Luo J-L, Chuang KT, Sanger AR. Effect of substitution with Cr<sup>3+</sup> and addition of Ni on the physical and electrochemical properties of Ce<sub>0.9</sub>Sr<sub>0.1</sub>VO<sub>3</sub> as a H<sub>2</sub>S-active anode for solid oxide fuel cells. *Journal of Power Sources*. 2009;194(1):252-62.
13. Vernoux P, Guillodo M, Fouletier J, Hammou A. Alternative anode material for gradual methane reforming in solid oxide fuel cells. *Solid State Ionics*. 2000;135(1–4):425-31.
14. Marina OA, Canfield NL, Stevenson JW. Thermal, electrical, and electrocatalytical properties of lanthanum-doped strontium titanate. *Solid State Ionics*. 2002;149(1–2):21-8.
15. Sun X-F, Guo R-S, Li J. Preparation and properties of yttrium-doped SrTiO<sub>3</sub> anode materials. *Ceramics International*. 2008;34(1):219-23.
16. Canales-Vázquez J, Ruiz-Morales JC, Marrero-López D, Peña-Martínez J, Núñez P, Gómez-Romero P. Fe-substituted (La,Sr)TiO<sub>3</sub> as potential electrodes

for symmetrical fuel cells (SFCs). *Journal of Power Sources*. 2007;171(2):552-7.

17. Tao S, Irvine JTS. Synthesis and Characterization of  $(\text{La}_{0.75}\text{Sr}_{0.25})\text{Cr}_{0.5}\text{Mn}_{0.5}\text{O}_{3-\delta}$ , a Redox-Stable, Efficient Perovskite Anode for SOFCs. *Journal of The Electrochemical Society*. 2004;151(2):A252.

18. Sauvet A. Catalytic activity for steam methane reforming and physical characterisation of  $\text{La}_{1-x}\text{Sr}_x\text{Cr}_{1-y}\text{Ni}_y\text{O}_{3-\delta}$ . *Solid State Ionics*. 2004;167(1-2):1-8.

19. Primdahl S, Hansen JR, Grahl-Madsen L, Larsen PH. Sr-Doped  $\text{LaCrO}_3$  Anode for Solid Oxide Fuel Cells. *Journal of The Electrochemical Society*. 2001;148(1):A74-A81.

20. Jung S, Lu C, He H, Ahn K, Gorte RJ, Vohs JM. Influence of composition and Cu impregnation method on the performance of  $\text{Cu}/\text{CeO}_2/\text{YSZ}$  SOFC anodes. *Journal of Power Sources*. 2006;154(1):42-50.

21. Jin Y, Yasutake H, Yamahara K, Ihara M. Suppressed Carbon Deposition Behavior in Nickel/Yttria-Stabilized Zirconia Anode with  $\text{SrZr}_{0.95}\text{Y}_{0.05}\text{O}_{3-\alpha}$  in Dry Methane Fuel. *Journal of The Electrochemical Society*. 2010;157(1):B130.

22. Park CY, Azzarello FV, Jacobson AJ. The oxygen non-stoichiometry and electrical conductivity of  $\text{La}_{0.7}\text{Sr}_{0.3}\text{Cu}_{0.2}\text{Fe}_{0.8}\text{O}_3$ . *Journal of Materials Chemistry*. 2006;16(36):3624.

## Chapter 3. Experimental Methodology

### 3.1 Synthesis of Materials

A modified glycine combustion method has been applied for preparing the perovskite anodes. Stoichiometric amounts of metal nitrates are weighed and dissolved in deionized water. Then, certain amounts of glycine are added into the solution; the molar ratio of glycine to the total metal cation content is 2:1. The solution is stirred thoroughly and then heated on a hot plate until self-combustion happens. The powders are then calcined at elevated temperatures to form a pure perovskite structure.

### 3.2 Fabrication of the cell

Fuel cells were fabricated using commercial YSZ disks (FCM, “fuelcellmaterials.com”) as electrolyte. The cathode was a mixture of equal weights of YSZ powder (TOSOH Company) and functional cathode catalyst. The anode was prepared through mixing equal weights of YSZ and the prepared anode materials. Both cathode and anode inks were prepared from oxide powders dispersed in terpineol mixed with 10% polyethylene glycol (PEG) as a screen printing binder. The electrode inks were deposited onto the YSZ electrolyte disc using screen printing to form a (MEA), and then the cell was sintered at high temperature to form a good bond between the

electrodes and electrolyte. Platinum paste and gold paste were painted onto the cathode side and anode side, respectively, to serve as the current collectors.

Single cell tests were performed in a vertical furnace with a coaxial two-tube (inlet and outlet) set-up. The outlet tube was directly sealed (Ceramabond 503, Aremco Products) to the outer edge of the anode side of the single cell electrolyte to avoid leakage of fuel gas and oxygen. A Thermolyne F79300 tubular furnace was used to heat the cell. Hydrogen or hydrogen mixed with 5000 ppm H<sub>2</sub>S (5000 ppm H<sub>2</sub>S-H<sub>2</sub>) (Praxair) was fed as the fuel at a rate of 75 mL min<sup>-1</sup>. The electrochemical performance of the fuel cell was measured using a Solartron 1287 instrument with a 2588 frequency response analyzer. The polarization resistance of the cell was estimated based on electrochemical impedance spectra (EIS) measured at the open circuit voltage with a AC potential signal of ±10 mV amplitude and a frequency range of 1 MHz to 0.1 Hz.

Fig. 3-1 shows the anode and cathode sides of a typical fabricated cell.

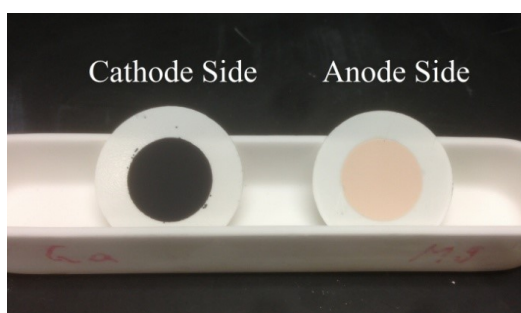


**Fig.3-1 Photo of anode and cathode sides of the fabricated cell**

### 3.3 Electrochemical Test of Anode Materials

Two coaxial alumina tubes (containing an inlet and an outlet) are used as electrode compartments to place MEA. The ceramic sealant is applied to seal the outlet to the outer edge directly on the anode side to prevent the leakage of fuel. Gold wires welded to a gold mesh contacting the electrode go through the inlet and are connected to the testing instrument. The fuel is fed to the anode chamber at a certain flow rate and the cathode chamber is open to air directly. Fig. 3-2 shows the schematics of the SOFCs setup using YSZ as the electrolyte.

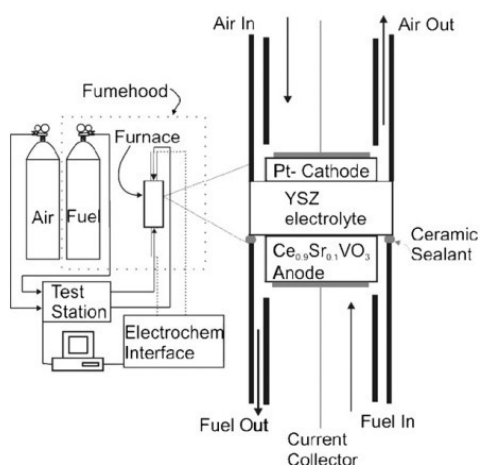


**Fig.3-2 Schematics of SOFCs setup[1]**

### 3.4 Characterization of Anode Materials

The phase structures of synthesized powders were identified using a Rigaku Rotaflex XRD with Co Ka radiation and the data were analyzed using JADE software.

N<sub>2</sub> adsorption/desorption isotherms are recorded at 77 K on an automated micromeritics Tri-Star 3020 apparatus. Surface areas are calculated using the multipoint BET equation.

XPS was performed using a Kratos Analytical AXIS 165. A monochromatic Al K $\alpha$  source ( $h\nu = 1486.6$  eV) was used with a power of 210 W and base pressure of  $3 \times 10^{-8}$  Pa in the analytical chamber. Spectra were referenced to the C 1s binding energy of 284.6 eV, and were fitted using Gaussian-Lorentzian peak shapes and Shirley baselines.

The micromorphology of the materials was examined using a JEOL 6301F SEM. TEM characterizations were conducted using a JEOL JEM 2100 transmission electron microscope with EDX detector and a JEOL 2100 TEM with EELS mapping capabilities (operated at 200 kV accelerating voltage). HAADF with EDX elemental mapping was used to identify the chemistry of the samples. For TEM analysis, the generated powders were dispersed in alcohol solution. One drop of the prepared suspension was deposited on a carbon-coated TEM Cu grid and dried in air before TEM characterization. The reduced samples for SEM/TEM analysis were prepared in dry 5% H<sub>2</sub>/N<sub>2</sub> at a temperature of 800 °C for 4 h.

TGA measurements were conducted using a TA Instruments SDT Q600 under 5% H<sub>2</sub>/N<sub>2</sub> or air from 100 °C to 900 °C with a flow rate of 20 mL min<sup>-1</sup> and a heating rate of 20 °C min<sup>-1</sup>.

O<sub>2</sub>-TPD measurements were performed using a Micromeritics AutoChem II 2920 instrument connected to a ThermoStar GSD 301 T2 mass spectrometer. 100 mg of each of the anode materials was placed in a quartz reactor, pretreated under 20% O<sub>2</sub> - N<sub>2</sub> with a flow rate of 20 mL min<sup>-1</sup> at 550 °C for 2 h and cooled down to room temperature under the same composition flow. Then, the samples were treated in pure He with a flow rate of 10 mL min<sup>-1</sup> and at the temperatures from 25 °C to 900 °C with a ramp of 5 °C min<sup>-1</sup>. In order to obtain complete desorption, the catalysts were maintained at 900 °C for 15 min.

H<sub>2</sub>-TPR was performed using an AutoChem II 2920 instrument (Micromeritics, USA) equipped with a thermal conductivity detector (TCD). All samples were treated with helium at 1000 °C for 30 min before TPR. The flow rate for analysis was 10% H<sub>2</sub>/Ar at 10 mL min<sup>-1</sup> and the temperature ramping rate was 10 °C min<sup>-1</sup>.

TECs were measured on rectangular-shaped bar samples (5 mm\*5 mm\*20 mm) from room temperature to 900 °C at a heating rate of 5 °C min<sup>-1</sup> by using a dilatometer instrument. (NETZSCH).

Van der Pauw four-point method was used to measure electrical conductivity of the synthesized samples by ProbStat instruments in the air.

TPO method was employed to characterize and quantify carbon deposition on the anode materials after various treatments. The samples were put in an alumina tube that was loaded into the TPO apparatus and exposed to a flow of 10% O<sub>2</sub> balanced with He at 50 mL/min for 1 h. The temperature was then

increased from room temperature to 850 °C at 20 °C /min and the effluents were analyzed with a mass spectrometer (Thermo star 301). The signals monitored during the TPO experiment included  $m/z = 44$  ( $\text{CO}_2$ ),  $m/z = 28$  ( $\text{CO}$  only, excluding the contributions of the residual  $\text{N}_2$  and  $\text{CO}_2$ ),  $m/z = 32$  ( $\text{O}_2$ ),  $m/z = 18$  ( $\text{H}_2\text{O}$ ),  $m/z = 34$  ( $\text{H}_2\text{S}$ ),  $m/z = 60$  ( $\text{COS}$ ),  $m/z = 64$  ( $\text{SO}_2$ ) and  $m/z = 76$  ( $\text{CS}_2$ ). Prior to the TPO analysis, the mass spectrometer signals were calibrated using gas mixtures of known concentrations.

A series of redox cycles on the cell was performed at 800 °C, with each cycle being conducted through the following steps: (1) the cell was treated with 5000 ppm  $\text{H}_2\text{S-H}_2$  for 24 h; (2) switched off the anode gas supply and exposed the anode to 5%  $\text{O}_2/\text{N}_2$  for 2 h; (3) the fuel of 5000 ppm  $\text{H}_2\text{S-H}_2$  was introduced again until the fuel cell reached a steady state. The power density data were measured after the introduction of the fuel for 30 min.

## **Chapter 4. Electrochemical performance and carbon deposition resistance of Ce-doped $\text{La}_{0.7}\text{Sr}_{0.3}\text{Fe}_{0.5}\text{Cr}_{0.5}\text{O}_{3-\delta}$ anode materials for solid oxide fuel cells fed with syngas**

### 4.1 Introduction

Cerium (Ce) has been widely exploited for SOFCs as a performance promoter because of its mixed oxidation states of +III/+IV. It has been shown that modification by Ce could effectively suppress carbon deposition at the Ni/YSZ anode(1). It was also reported that significant improvement in electrochemical properties could be obtained by A-site substitution with Ce for  $\text{La}_{0.75}\text{Sr}_{0.25}\text{Mn}_{0.5}\text{Cr}_{0.5}\text{O}_{3-\delta}$  (LSCM) (2). Therefore, investigation of the effect of Ce dopant in  $\text{La}_{0.75}\text{Sr}_{0.25}\text{Fe}_{0.5}\text{Cr}_{0.5}\text{O}_{3-\delta}$  on electrochemical performance and resistance against carbon deposition appears to be a promising research field.

In this paper, a series of Ce-doped  $\text{La}_{0.7}\text{Sr}_{0.3}\text{Fe}_{0.5}\text{Cr}_{0.5}\text{O}_{3-\delta}$  (Ce-LSFC) perovskite anode catalysts was firstly synthesized by a modified glycine combustion method. The structural characteristics and electrochemical performances of Ce-LSFC with various Ce concentrations were studied in detail.

### 4.2 Experimental Procedure

A modified glycine nitrate combustion method was used to fabricate the Ce-LSFC anode material. Stoichiometric amounts of  $\text{La}(\text{NO}_3)_3 \cdot 6\text{H}_2\text{O}$ ,  $\text{Sr}(\text{NO}_3)_2$ ,  $\text{Fe}(\text{NO}_3)_3 \cdot 9\text{H}_2\text{O}$ ,  $\text{Cr}(\text{NO}_3)_3 \cdot 9\text{H}_2\text{O}$ ,  $\text{Ce}(\text{NO}_3)_3 \cdot 6\text{H}_2\text{O}$  and glycine were first dissolved in deionized water.

The molar ratio of glycine to the total content of the metal cations was 2:1. The solution was stirred and then heated on a hot plate until self-combustion occurred. The powders were ground and calcined at 1200 °C for 2 h to form different anode materials  $\text{La}_{0.7-x}\text{Sr}_{0.3}\text{Ce}_x\text{Fe}_{0.5}\text{Cr}_{0.5}\text{O}_{3-y}$  (denoted as 100xCe-LSFC).

#### 4.3 Results and Discussion

The XRD patterns for all Ce doped LSFC are shown in Figure 4-1(a). The results confirmed the presence of single phase perovskite structure in the samples with the Ce concentration  $\leq 10\%$ . As the content of Ce reached 20%, the diffraction peak of the  $\text{CeO}_2$  phase appeared, located at  $28.5^\circ$ ,  $47.7^\circ$  and  $56.6^\circ$  (3). The results indicate that the Ce could not be totally doped into the A-site of LSFC perovskite at such a high content. It is also found from Figure 4-1(a) that the substitution for La by Ce led to a slight shift of all the XRD peaks to the higher angles. Vegard's law was applied to estimate the solubility limit of Ce in LSFC. A plot of the position of (110) diffraction peak for Ce-LSFC as a function of x, the concentration of Ce, is shown in Figure 4-1(b). The result predicted that the limiting value of x was 0.09. The statistic of the structural parameters of various materials calculated from Rietveld refinements using the XRD pattern data demonstrated that the cell volume decreased with the amount of Ce substitution, which could be explained by the fact that the radii of Ce ( $\text{Ce}^{3+}$  for 148 pm,  $\text{Ce}^{4+}$  for 128 pm) are smaller than that of La ( $\text{La}^{3+}$  for 150 pm)(4).

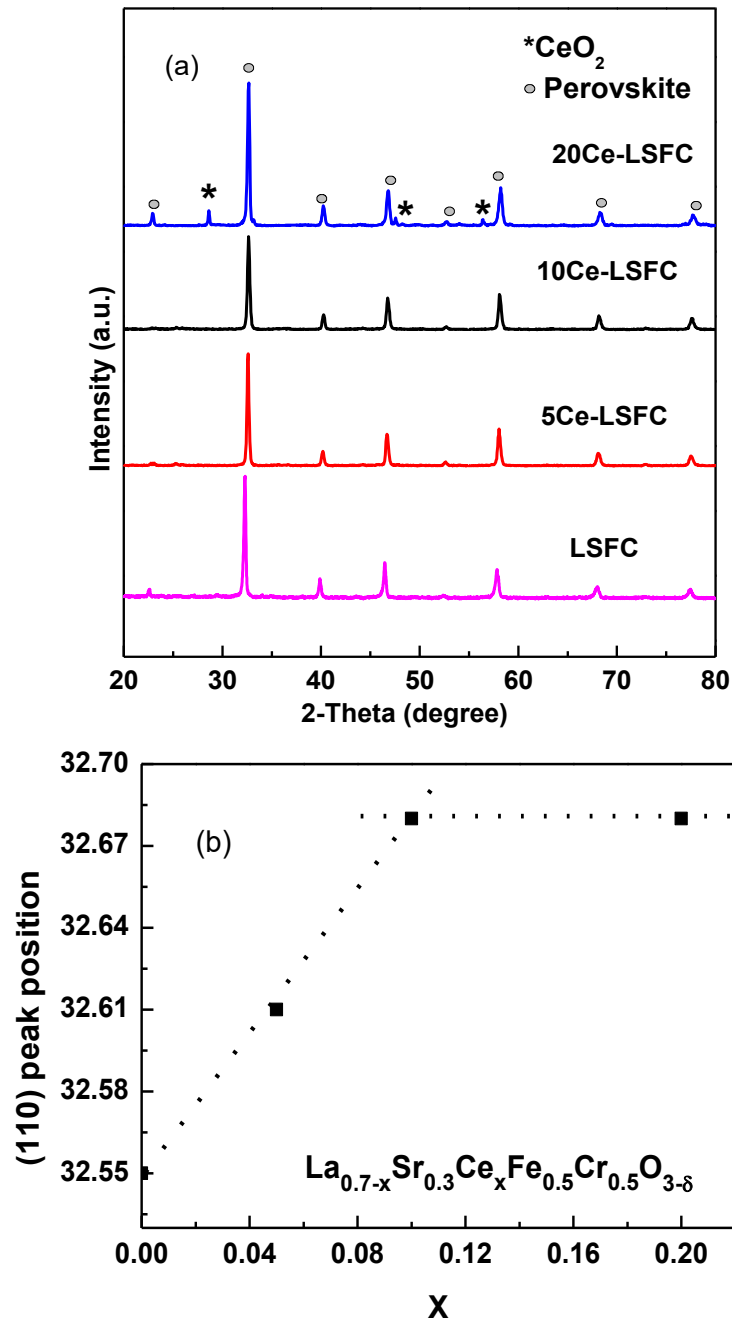


**Fig.4-1 (a) XRD patterns and (b) the position of the (110) diffraction peak vs. x for Ce-LSFC with various concentrations of Ce.**

The  $\text{O}_2$ -TPD profiles shown in Figure 4-2(a) demonstrate the different kinds of desorbed oxygen corresponding to the distinct temperature dependent oxygen evolution peaks. Generally, two kinds of oxygen were reported (denoted as  $\alpha$ - $\text{O}_2$  and  $\beta$ - $\text{O}_2$ ). The  $\alpha$ - $\text{O}_2$  desorbed below 550 °C could be regarded as the surface absorbed oxygen species

(5). The strength of the bond between the absorbed oxygen and cations was relatively weak. The A or B-site doped perovskite oxides will form some oxygen vacancies to maintain neutralization, which could be thought as an important way to increase the absorption of oxygen of the materials (6). Therefore, it could be inferred that the low temperature peaks observed below 550 °C were due to absorbed oxygen in lattice vacancies as well as surface-adsorbed oxygen. The two higher temperature peaks could be ascribed to  $\beta$ -O<sub>2</sub> which stemmed from the bulk of the structure. Although the results in this study do not allow a definitive assignment to the source of each  $\beta$ -O<sub>2</sub>, they were also both thought to be associated with the partial reduction of transition metal cations in B-sites (7) as the  $\beta$ -O<sub>2</sub> was diffusing to the surface, which could serve as an indicator of the mobility of oxygen.

Comparison of the three curves in Figure 4-2 (a) shows that the doping of Ce resulted in a shift of the first desorption peak to a lower temperature range, which could be explained by the difference of electronegativity between Ce and lanthanum (1.12 for Ce and 1.1 for La). Previous work has illustrated that such a phenomenon occurred with increasing content of less electronegative rare earths in the material (8). It has also been shown that the presence of Ce significantly increased the peak area for the desorbed  $\alpha$ -O<sub>2</sub>, indicating an increasing amount of oxygen vacancies.

In addition, the desorption temperature and peak area of  $\beta$ -O<sub>2</sub> were found to be strongly dependent on the content with Ce. Both desorption peaks of  $\beta$ -O<sub>2</sub> shifted to lower temperature ranges after doping of Ce, implying enhanced mobility of oxygen in

the bulk material. Additionally, the larger total peak area of  $\beta$ -O<sub>2</sub> for higher Ce doped material indicated a larger amount of mobile oxygen species.

The results of the TPO profile are displayed in Figure 4-2(b). All samples were treated with syngas at 800 °C for 24 h. The TPO peak of CO<sub>2</sub> shifted to the lower temperature zone for the material doped with Ce, meaning that the deposited carbon became more reactive and could be removed more easily. Through integrating the peak area, the amount of carbon deposited on the anode of 5Ce-LSFC was four times smaller than that on LSFC, indicating that the cerium could effectively suppress the appearance of carbon deposition.

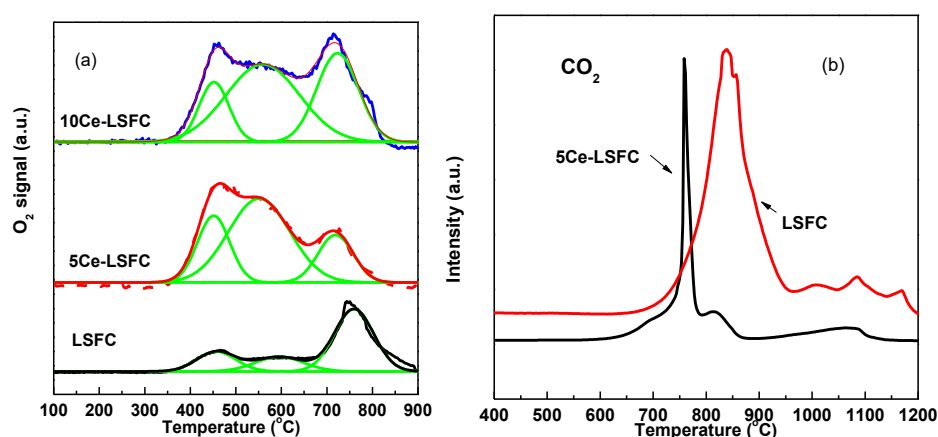


**Fig.4-2 (a) The O<sub>2</sub>-TPD profiles and (b) CO<sub>2</sub> production during TPO analyses for Ce-LSFC with various concentrations of Ce**

The catalytic activities of Ce-doped LSFC materials toward the oxidation of syngas were determined by measuring the impedance of symmetrical half cells at different temperatures and the results measured at OCV are shown in Figure 4-3(a) for the cells with Ce-doped LSFC-based anodes. The ohmic resistance was removed from the impedance data in order to make a comparison of the catalytic activities for the

different anode materials. Obviously, the Ce doped materials had much smaller activation polarization resistance (APR) compared with that of un-doped LSFC. At 800 °C, the 5Ce-LSFC showed APR of  $0.25 \Omega \text{ cm}^2$ , 40% smaller than that of 10Ce-LSFC, and four times smaller than that of the LSFC anode. The results of XRD in Figure 4-1(a) indicate that when the content of Ce reached 20 %, the diffraction peak of  $\text{CeO}_2$  was detected. However, with a doping level as low as 10 %, the exsolution of  $\text{CeO}_2$  might also occur with a particle size under the detection limitation of XRD. This speculation was confirmed by the results shown in Figure 4-1(b), in which the doping level of Ce in LSFC is estimated to be 0.09. Previous literature has also demonstrated that the excessive addition of  $\text{CeO}_2$  in  $\text{La}_{0.8}\text{Sr}_{0.2}\text{MnO}_3$  (9),  $\text{La}_{0.6}\text{Sr}_{0.4}\text{CoO}_3$  (9) and  $\text{La}_{0.95}\text{Ni}_{0.6}\text{Fe}_{0.4}\text{O}_3$  (10) perovskites decreased the electrical conductivities of the materials. The presence of ceria as a secondary phase in the perovskite structure oxide could block conduction paths between perovskite grains and suppress electronic conductivity of two-phase compositions (11). Hence, in our investigation, it can be inferred that a certain amount of  $\text{CeO}_2$  in the 10Ce-LSFC anode may reduce the total conductivity of the material, which was one of the reasons for the reduced electrochemical performance of the cell.

Because the 5Ce-LSFC showed much better electrochemical performance than 10Ce-LSFC, the comparison of the capabilities of regeneration for 5Ce-LSFC and LSFC anodes is shown in Figure 4-3 (b). The samples were treated with syngas at 800 °C for 24 h, the fuel was then switched to  $\text{H}_2$  for the 24 h at the same temperature, and

the syngas was switched back as the fuel for the next 24 h. It was discovered that in the first 24 h, carbon deposition formed on the anode resulted in an increase in the activation resistance polarization of LSFC from 1.4 to 6.1  $\Omega \text{ cm}^2$ , while during the same period of time, the value of 5Ce-LSFC increased from 0.27 to 1.73  $\Omega \text{ cm}^2$ . It is obvious that the doping of Ce can significantly slow down the degradation of anode catalytic activity. During the regeneration by in-situ introducing  $\text{H}_2$  for 24 h, the carbon deposition on the anode was removed. It was found that the values of LSFC and 5Ce-LSFC drop down to 2.3  $\Omega \text{ cm}^2$  and 0.30  $\Omega \text{ cm}^2$ , respectively. Compared with original values at 0 h, the increment of the value for LSFC was 50%, almost five times larger than the increment of 5Ce-LSFC. Such a difference indicated that the carbon deposition on 5Ce-LSFC could be removed more easily and completely. Within the next 24 h after the regeneration, the value of LSFC showed fourfold increase from 2.3  $\Omega \text{ cm}^2$  to 9.3  $\Omega \text{ cm}^2$  whereas the value of 5Ce-LSFC only increased to 1.98  $\Omega \text{ cm}^2$ . Compared with the values at 48 h and 72 h, the growth rates of LSFC and 5Ce-LSFC were 48% and 14%, respectively. These results proved that the doping of Ce enhances the tolerance toward carbon deposition and the capability of regeneration.

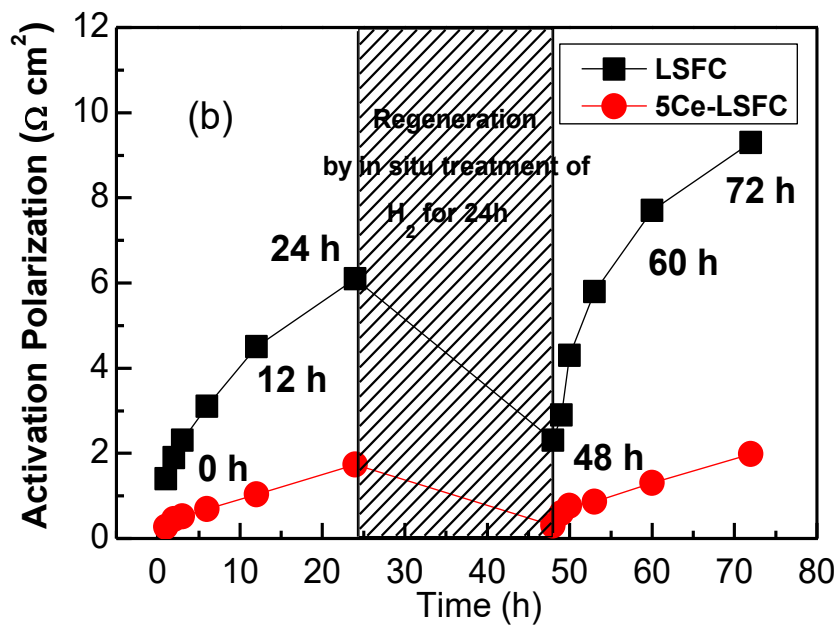
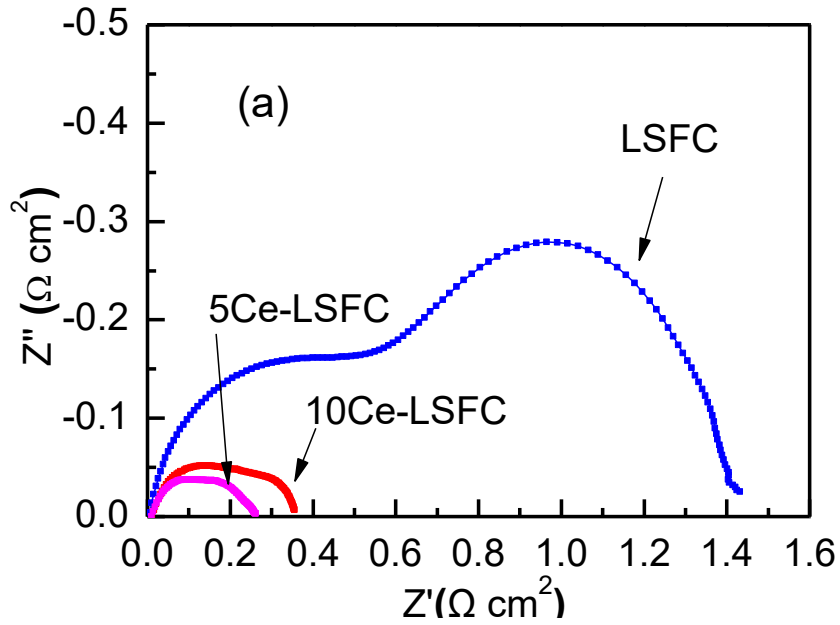


**Fig.4-3 (a) EIS results for the symmetrical half cells with various anodes in syngas at 800 °C (b) Regeneration tests of LSFC and 5Ce-LSFC in syngas at 800 °C.**

The electrochemical performance of the SOFC with 5Ce-LSFC anode using YSZ as electrolyte was evaluated in syngas at 800 °C. The corresponding I-V and power

density curves are shown in Figure 4-4 (a). It can be found that the cell has an open-circuit potential of around 0.96 V, near the value determined by Nernst Equation. At 800 °C, the SOFC with 5Ce-LSFC anode had a maximum current density and power density of around 0.95 A cm<sup>-2</sup> and 0.27 W cm<sup>-2</sup>, respectively. Figure 4-4(b) shows the EIS result of the cell with a 5Ce-LSFC anode. The equivalent circuit used for simulating the EIS results using Z-View software is also given in Figure 4-4 (b). The values of all the components of ohmic resistance, anode polarization resistance and cathode polarization were obtained. The high frequency intercept was attributed to the ohmic resistance,  $R_s$ , of around 0.45Ω cm<sup>2</sup> associated with the 0.3 mm thick YSZ electrolyte. The cathode activation polarization resistance,  $R_1$ , was 0.16Ω cm<sup>2</sup>, this is consistent with a result in the literature that LSM-YSZ cathodes yield an activation polarization resistance of around 0.15 Ω cm<sup>2</sup> (12). The simulated equivalent circuit also showed the anode polarization resistance,  $R_2$ , of 0.25 Ω cm<sup>2</sup>. These results indicate that the 5Ce-LSFC showed high catalytic activity for the oxidation of syngas and could be regarded as a promising anode candidate for SOFCs using hydrocarbon fuel.

A durability test was performed with the 5Ce-LSFC anode in syngas at 800 °C and a potential of 0.7 V for 20 hours. As shown in Figure 4-4 (c), the fuel cell generated an initial current density of around 0.36 A cm<sup>-2</sup>. However, a slight and gradual current density drop was detected in the 20 hours of the durability test, which may be attributed to the formation of carbon deposition

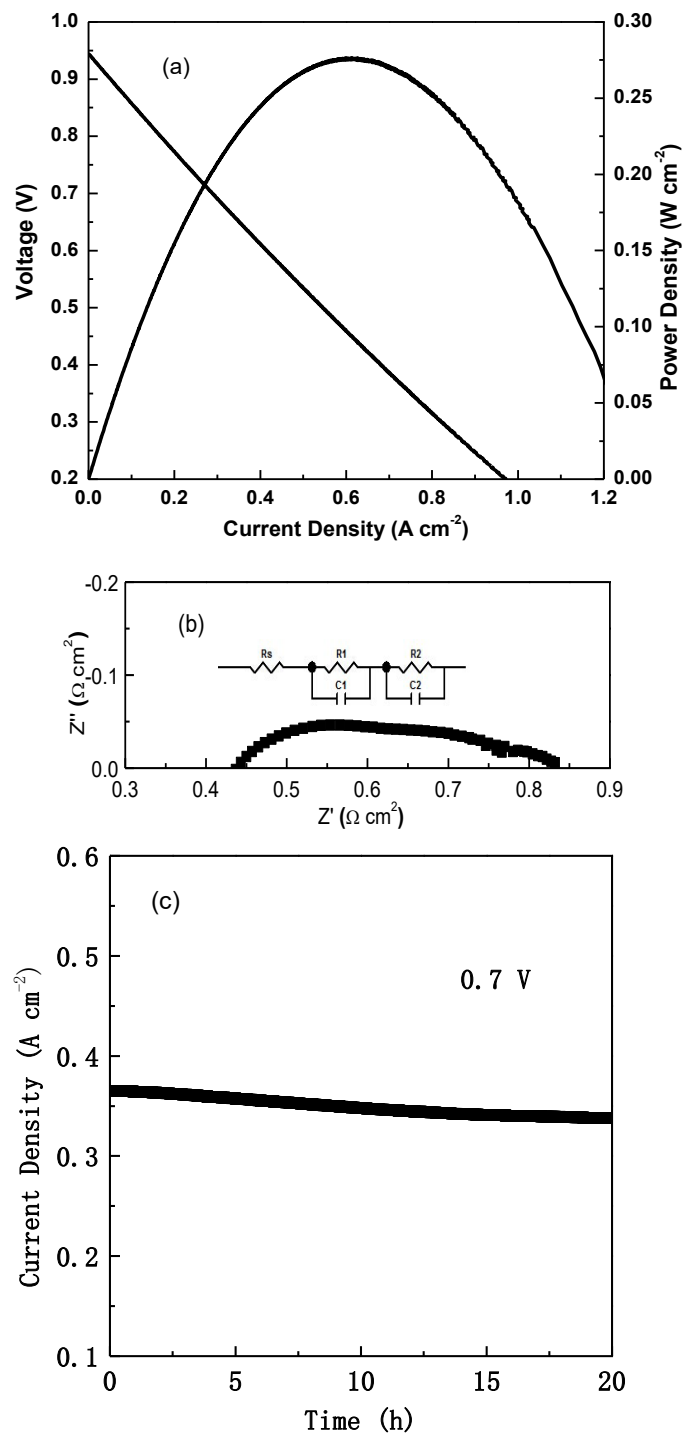


**Fig.4-4 (a) The I-V and power density curves of SOFC with 5Ce-LSFC anode fed with syngas at 800 °C, (b) The corresponding EIS result and the equivalent circuit used for simulation of the cell, (c) The durability test of the fuel cell fed with syngas at 800 °C.**

stemming from the side reactions of syngas. Nevertheless, this degradation can be recovered as shown from the results of the regeneration test in which the activation polarization resistance of the 5Ce- LSFC anode increased in the prolonged test but can be regenerated by the in-situ introduction of H<sub>2</sub>.

#### 4.4 Conclusions

In summary, a modified glycine combustion method was applied to synthesize Ce-LSFC perovskite anode catalysts which showed better catalytic activity for oxidizing syngas in comparison with LSFC anodes. In addition, it can be inferred that the better capability of the carbon deposition removal of the Ce-doped materials may be due to the increased oxygen vacancies amount and mobility of lattice oxygen.

## 4.5 References

1. Chen XJ, Khor KA, Chan SH. Suppression of Carbon Deposition at CeO<sub>2</sub>-Modified Ni/YSZ Anodes in Weakly Humidified CH<sub>4</sub> at 850°C. *Electrochemical and Solid-State Letters*. 2005;8(2):A79-A82.
2. Lay E, Benamira M, Pirovano C, Gauthier G, Dessemond L. Effect of Ce-Doping on the Electrical and Electrocatalytical Behavior of La/Sr Chromo-Manganite Perovskite as New SOFC Anode. *Fuel Cells*. 2012;12(2):265-74.
3. Périllat-Merceroz C, Gauthier G, Roussel P, Huvé M, Gélin P, Vannier R-N. Synthesis and Study of a Ce-Doped La/Sr Titanate for Solid Oxide Fuel Cell Anode Operating Directly on Methane. *Chemistry of Materials*. 2011;23(6):1539-50.
4. Shannon RD, Prewitt CT. Effective ionic radii in oxides and fluorides. *Acta Crystallographica Section B*. 1969;25(5):925-46.
5. Levasseur B, Kaliaguine S. Effects of iron and cerium in La<sub>1-y</sub>Ce<sub>y</sub>Co<sub>1-x</sub>Fe<sub>x</sub>O<sub>3</sub> perovskites as catalysts for VOC oxidation. *Applied Catalysis B: Environmental*. 2009;88(3-4):305-14.
6. Seiyama T, Yamazoe N, Eguchi K. Characterization and activity of some mixed metal oxide catalysts. *Industrial & Engineering Chemistry Product Research and Development*. 1985;24(1):19-27.

7. Choi H, Fuller A, Davis J, Wielgus C, Ozkan US. Ce-doped strontium cobalt ferrite perovskites as cathode catalysts for solid oxide fuel cells: Effect of dopant concentration. *Applied Catalysis B: Environmental*. 2012;127(0):336-41.
8. Levasseur B, Kaliaguine S. Effect of the rare earth in the perovskite-type mixed oxides  $AMnO_3$  (A=Y, La, Pr, Sm, Dy) as catalysts in methanol oxidation. *Journal of Solid State Chemistry*. 2008;181(11):2953-63.
9. Konyshева E, Francis SM, Irvine JTS. Crystal Structure, Oxygen Nonstoichiometry, and Conductivity of Mixed Ionic–Electronic Conducting Perovskite Composites with  $CeO_2$ . *Journal of The Electrochemical Society*. 2010;157(1):B159.
10. Konyshева E, Irvine JTS. Electronic conductivity of modified  $La_{0.95}Ni_{0.6}Fe_{0.4}O_{3-\delta}$  perovskites. *Journal of Power Sources*. 2009;193(1):175-9.
11. Tuller HL, Nowick AS. Defect Structure and Electrical Properties of Nonstoichiometric  $CeO_2$  Single Crystals. *Journal of The Electrochemical Society*. 1979;126(2):209-17.
12. Nielsen J, Hjelm J. Impedance of SOFC electrodes: A review and a comprehensive case study on the impedance of LSM:YSZ cathodes. *Electrochimica Acta*. 2014;115(0):31-45.

## **Chapter 5. A-site deficient lanthanum strontium chromite: the parent for *in-situ* exsolution of highly-active and regenerable nano-Ni anode for solid oxide fuel cells (SOFCs)**

### 5.1 Introduction

To increase the activity of perovskite, active metal catalysts are introduced as catalytic nanoparticles dispersing on the external surface and porous inner surface of perovskite-based anodes (1, 2). These functional materials are usually synthesized using either wet impregnation method(3, 4) or chemical deposition technology(5-7) to generate a structure with catalytic particles attached to the surface of support material through a calcination process at high temperatures. However, these methods are time consuming and may lead to problems of uncontrolled particle sizes and unexpected aggregation of particles(8). Recently, a more advanced and effective way has been developed to introduce nano particles on perovskite oxides, by which the active elements (transition metals(8, 9) or precious metal(2, 10)) are doped into B-sites and then partly *in-situ* exsolved out of the lattice as active nanoparticles in reducing atmospheres. The produced nano-catalysts provide more active sites and larger specific surface area to facilitate catalytic reactions. In comparison to the wet impregnation and chemical deposition technologies, this method is time-efficient and can generate nanoparticles with many even dispersion. Besides, the problem of grain coarsening

could be also effectively alleviated due to the strong interaction between the nanoparticle and the matrix.

Most of the previous investigations on the application of exsolution in preparing perovskite anodes mainly focused on the stoichiometric perovskite oxide with  $A/B = 1$ , in which only limited reducible cations were exsolved out, leading to restricted electrochemical performance. Two recent studies on  $\text{La}_{0.52}\text{Sr}_{0.28}\text{Ni}_{0.06}\text{Ti}_{0.94}\text{O}_3$  perovskite oxides(11) and Fe/Ni-doped  $\text{La}_{0.2}\text{Sr}_{0.25}\text{Ca}_{0.45}\text{TiO}_3$  (LSCTA) perovskite(12) suggest that more cations can be preferentially exsolved on the surface of the perovskite matrix when the composition of a perovskite oxide is altered to  $A/B < 1$ . It is likely that the A-site deficient could provide an alternative promising way to “decorate” the perovskite structure with well-dispersed functional nano-particles.

However, to the best of our knowledge, no work has been done so far to assess the electrochemical performance of A-site deficient perovskite anode in SOFCs. It also remained unclear whether the functional materials of this type would have desirable redox stability in sour fuel. Therefore, the objective of this work is to address the above issues and find a more promising way to fabricate new functional perovskite materials for industrial SOFC application. In this paper, Ni-doped LSC (strontium doped lanthanum chromite) perovskite anode with A-site deficiency was prepared using the exsolution method and its microstructural properties, electrochemical performances and redox stability in sour fuel were characterized and compared with those of the anode of stoichiometric composition.

## 5.2 Experimental Procedures:

The glycine nitrate combustion method was used to fabricate the  $\text{La}_{0.7}\text{Sr}_{0.3}\text{CrO}_{3-\xi}$ ,  $\text{La}_{0.7}\text{Sr}_{0.3}\text{Cr}_{1-x}\text{Ni}_x\text{O}_{3-\xi}$  and  $\text{La}_{0.6}\text{Sr}_{0.3}\text{Cr}_{1-x}\text{Ni}_x\text{O}_{3-\xi}$  anode materials for fuel cell test, denoted as LSC, 73LSCNi-x and 63LSCNi-x [where x (mol%) = 0, 5, 10, 15 and 20], respectively. In addition, the  $\text{La}_{0.7}\text{Sr}_{0.3}\text{Cr}_{0.85}\text{O}_{3-\xi}$ ,  $\text{La}_{0.6}\text{Sr}_{0.3}\text{Cr}_{0.85}\text{O}_{3-\xi}$ ,  $\text{La}_{0.7}\text{Sr}_{0.3}\text{Cr}_{0.85}\text{Ni}_{0.05}\text{O}_{3-\xi}$ ,  $\text{La}_{0.6}\text{Sr}_{0.3}\text{Cr}_{0.85}\text{Ni}_{0.05}\text{O}_{3-\xi}$ ,  $\text{La}_{0.7}\text{Sr}_{0.3}\text{Cr}_{0.85}\text{Ni}_{0.1}\text{O}_{3-\xi}$ , and  $\text{La}_{0.6}\text{Sr}_{0.3}\text{Cr}_{0.85}\text{Ni}_{0.1}\text{O}_{3-\xi}$  materials were also fabricated using the same method and denoted as 73LSC, 63LSC, 73LSCNi-5, 63LSCNi-5, 73LSCNi-10 and 63LSCNi-10, respectively.

## 5.3 Results

The crystalline structures of the materials with or without Ni doping were examined using XRD and are shown in Figure 5-1(a). The  $\text{La}_{0.7}\text{Sr}_{0.3}\text{CrO}_{3-y}$  (LSC),  $\text{La}_{0.7}\text{Sr}_{0.3}\text{Cr}_{0.85}\text{Ni}_{0.15}\text{O}_{3-\xi}$  (73LSCNi-15) and  $\text{La}_{0.6}\text{Sr}_{0.3}\text{Cr}_{0.85}\text{Ni}_{0.15}\text{O}_{3-\xi}$  (63LSCNi-15) exhibit perovskite structure with orthorhombic unit cells of space group Pnma (62). All of the main peaks are matched well with those of  $\text{LaCrO}_3$  (JCPDS no.24-1016), indicating that neither B-site doping of Ni in 63LSCNi-15 (or in 73LSCNi-15) nor A-site deficiency in 63LSCNi-15 has any influence on the crystalline structure of perovskite. The reason is that A-site vacancies may act as one kind of dopant with different sizes from those of host cations, similar to accommodation of cation substitution. As shown in Figure 5-1(a), 63LSCNi-15 still maintained a single-phase

perovskite structure after being exposed to 5% H<sub>2</sub>/N<sub>2</sub> at 800 °C for 4 h, and metallic Ni diffraction peaks were present at 44.5° and 52°, indicating the Ni reduction that occurred in the perovskite lattice(13). After re-oxidation in air under calcination condition, the material showed pure perovskite structure again without the formation of impurity phases such as Ni and/or NiO (Figure 5-1(a)), which means that the exsolved metallic Ni was, once again, dissolved into the perovskite lattice. This also implies that the A-site deficient material would have good redox structural stability.

As shown in Figure 5-1(b), the doping with Ni ( $\leq 15$  mol %) had no influence on the formation of a pure perovskite structure in the A-site deficient materials with orthorhombic symmetry. For 63LSCNi-20, the formation of NiO was detected at the diffraction peaks of 37° and 43° (consistent with the other observation(14)), further confirming that the solubility limit of nickel in stoichiometric LSC perovskite with stoichiometry shall be  $< 20$  mol%(10). Otherwise, excessive doping of Ni can result in the formation of NiO after redox cycles. When below the solubility limit, only metallic Ni was detected and the corresponding XRD observations were consistent with the calculated free energy changes of the oxide reductions in LSCNi perovskite as shown in Figure 5-1 (c). It is clear that the NiO shall be the only reducible oxide in perovskite because of its negative Gibbs free energy ( $- 46.47$  kJ mol<sup>-1</sup>) at 800 °C, while other metal oxides have positive Gibbs free energies.

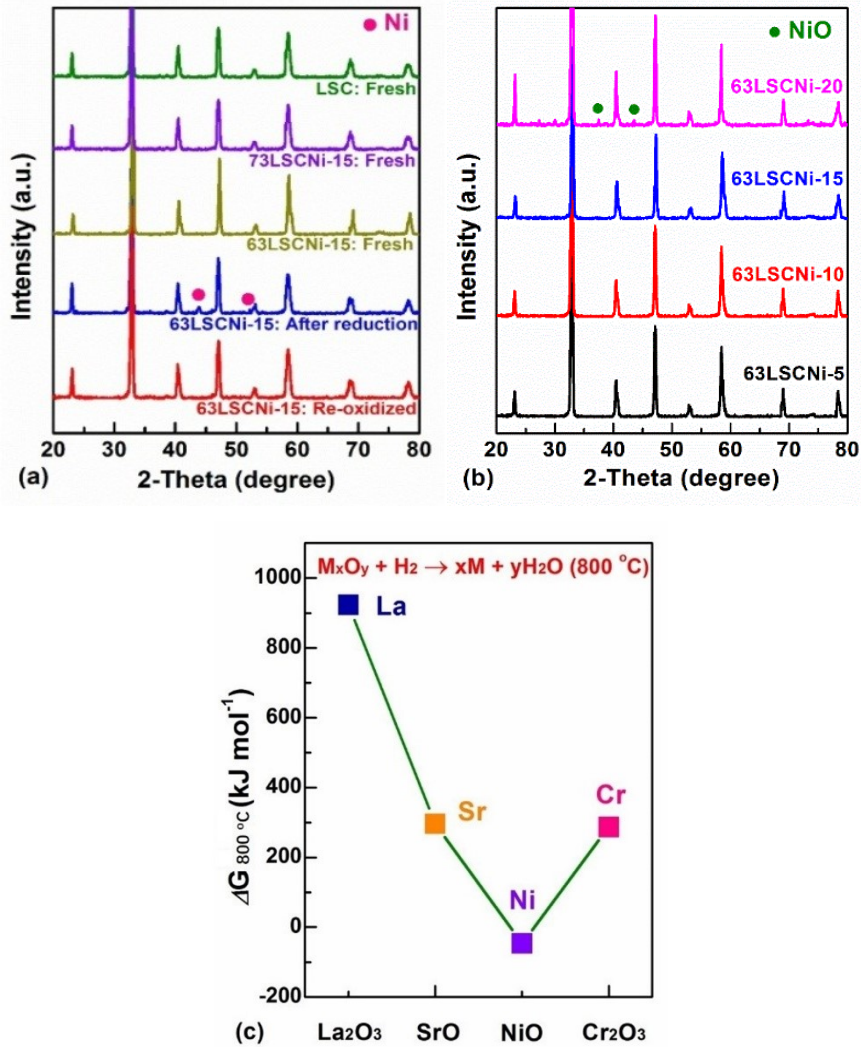


**Fig.5- 1 X-ray diffraction (XRD) patterns and calculated Gibbs free energy of reduction reaction for each element oxide in LSCNi perovskite. (a) XRD patterns of the various fresh and treated materials. Among them, 63LSCNi-15 was reduced in 5% H<sub>2</sub>/N<sub>2</sub> at 800 °C for 4 h and re-oxidized in air at 1300 °C for 3h. (b) XRD patterns of the fresh 63LSCNi-x with Ni contents, x%, of 5% to 20%. (c) The theoretical value of reduction Gibbs free energy for each element oxide in LSCNi-15 perovskite at 800 °C and standard atmosphere pressure. The data are estimated using HSC 6.0 software.**

Oxygen vacancies play a significant role in the conductivity and catalytic activity of a perovskite material. Thermogravimetric analysis was applied to measure the amount of oxygen vacancies in different materials from 100 °C to 900 °C with a heating rate of 20 °C min<sup>-1</sup> in 5% H<sub>2</sub>/N<sub>2</sub> and the results are shown in Figure 5-2(a). The LSC was the most stable material with the lowest weight loss (0.1%) during the measurement, while the formation of oxygen vacancies in 73LSCNi-15 started at a temperature of ~ 620 °C and the total weight loss was about 0.4%. In contrast with the cases of LSC and 73LSCNi-15, the A-site deficient 63LSCNi-15 started to lose weight at 515 °C and exhibited the highest oxygen vacancy content as its weight loss was close to ~ 2.5%. Such a remarkable difference indicates that the A-site deficiency could lead to high conductivity of the material.

Since weight loss accompanies the reduction process, the mass changes during the TGA tests could be used to estimate the quantity of oxygen non-stoichiometry,  $\xi$ . Results in Figure 5-2(b) indicate that  $\xi$  increased from 0.025 to 0.1 after doping of Ni in B-sites of LSC, which was much less than that of the non-stoichiometric A-site composition ( $\xi = 0.32$ ). Thus, it can be quantitatively inferred that the deficiency in A-sites can help the formation of oxygen vacancies in the perovskite structure and enhance the mobility of lattice oxygen. Thus, the catalytic activity of the material can also be facilitated. The high value of  $\xi$  for perovskite with A-site deficiency is likely because A-site deficiency can limit the number of intrinsic Schottky defects, which in turn facilitate the diffusion and removal of lattice oxygen in reducing atmosphere.

To investigate the reducibility of this series of Ni-doped LSC, the TPR analysis was applied on each sample and the results are shown in Figure 5-2(c). There was no obvious peak in the pattern of the LSC sample, suggesting that the  $\text{La}_{0.7}\text{Sr}_{0.3}\text{CrO}_3$  might not be reduced at up to 900 °C, which was consistent with the TGA measurements. The improvement in the reducibility of the Ni-substituted compositions was observed for both 63LSCNi-15 and 73LSCNi-15, indicated by multiple peaks of different Ni states. Previous studies(15, 16) show that the reduction of Ni-substituted LSC perovskite likely occurs through two main steps: (1) the  $\alpha$ -peak at the temperature of  $\sim 500$  °C from reduction of  $\text{Ni}^{3+}$  into  $\text{Ni}^{2+}$ ; and (2) the  $\beta$ -peak at the temperature of  $\sim 600$  °C, associated with reduction of  $\text{Ni}^{2+}$  into metallic  $\text{Ni}^0$ . With the introduction of A-site deficiency in the perovskite lattice, the reducibility of Ni was remarkably facilitated. As shown in the Figure 5-2 (c), the first reduction peak shifted from 532 °C to 492 °C, and the second reduction peak from 602 °C to 577 °C. Moreover, the ratio of the  $\beta$ -peak area to  $\alpha$ -peak area was around 0.67 for 63LSCNi-15, higher than that (0.25) for 73LSCNi-15, a clear indication that A-site deficiency could facilitate the reduction of  $\text{Ni}^{2+}$  to Ni to generate more Ni nano particles.

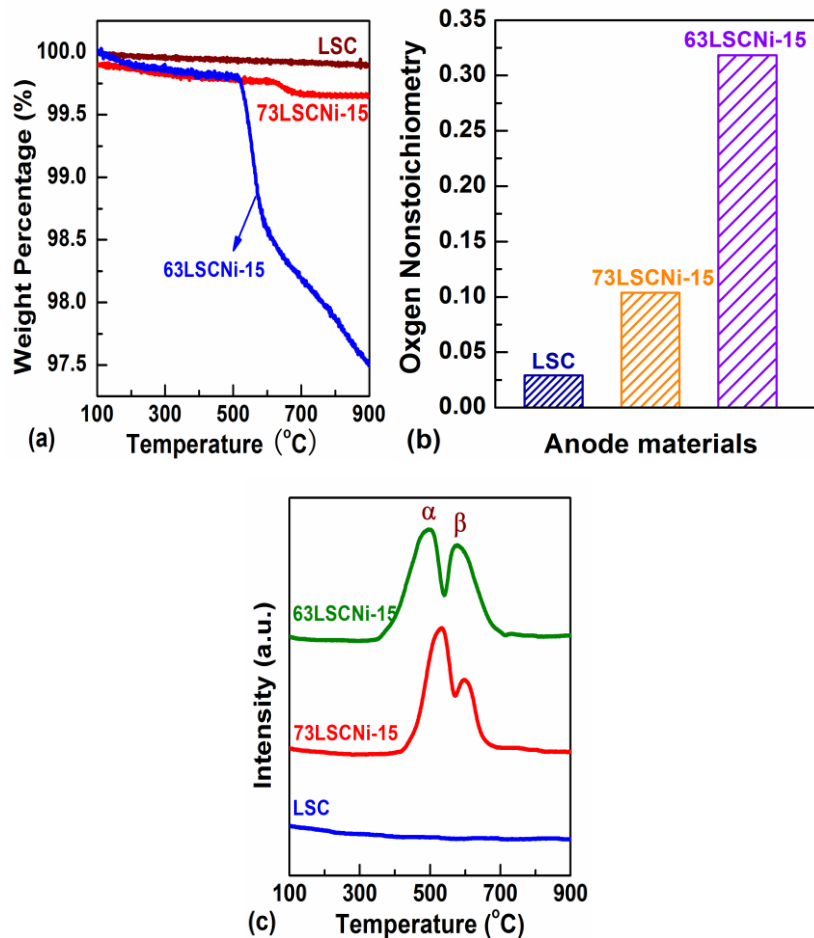


**Fig.5- 2 TGA, quantity of oxygen non-stoichiometry and characterizations of H<sub>2</sub>-TPR of the various catalysts. (a) TGA curves of the fresh LSC, 73LSCNi-15 and 63LSCNi-15 measured in 5% H<sub>2</sub>/N<sub>2</sub> with a flow rate of 20 mL min<sup>-1</sup> from 100 °C to 900 °C at a heating rate of 20 °C min<sup>-1</sup>. (b) The quantity of oxygen non-stoichiometry determined based on the mass change during the TGA test. (c) H<sub>2</sub>-TPR curves of the fresh LSC, 73LSCNi-15 and 63LSCNi-15. All samples were treated with helium at 1000 °C for 30 min before TPR. The flow rate of 10% H<sub>2</sub>/Ar was 10 mL min<sup>-1</sup> and the temperature ramping rate was 10 °C min<sup>-1</sup>.**

SEM and TEM characterization in Figure 5-3 reveal the influence of A-site deficiency on the exsolution of Ni nano particles. After being reduced at 800 °C for 4 h,

numerous metallic Ni nanoparticles were formed on the A-site deficient 63LSCNi surface [Figure 5-3 (a)], but only limited Ni particles were produced on the stoichiometric composite [Figure 5-3 (b)], even though the doping content of Ni in B-sites of the samples was the same (15%). Such a difference indicates that the A-site deficient perovskite is more prone to exsolution of B-site species than the stoichiometric one.

The chemical compositions of the nano particles anchored on the surface of bulk material and the bulk material were examined using EDX analysis and the results are shown in Figure 5-3(c). It is clear that the chemical composition of the bulk (point B) was quite different from the nano particle (point 5) where a much stronger Ni peak was found.

Detailed structural characterization of the nano particle using TEM technique is depicted in Figure 5-3(d). A clear lattice image was observed only for the particles whose arrangement of atom planes was parallel with the direction of the electron beam. The spacing between two adjacent lattice fringes was 0.206 nm, close to the (111) planes of fcc Ni (JCPDS 01-1258,  $d(111) = 0.2030$  nm). Figure 5-3(e) shows the Ni mapping obtained from the energy loss windows centered at the C K-ionization edge at 855 eV, and confirms that the exsolution of nano particle was composed of metallic Ni. Figure 5-3(f) shows the HAADF image of a 63LSCNi-15 particle

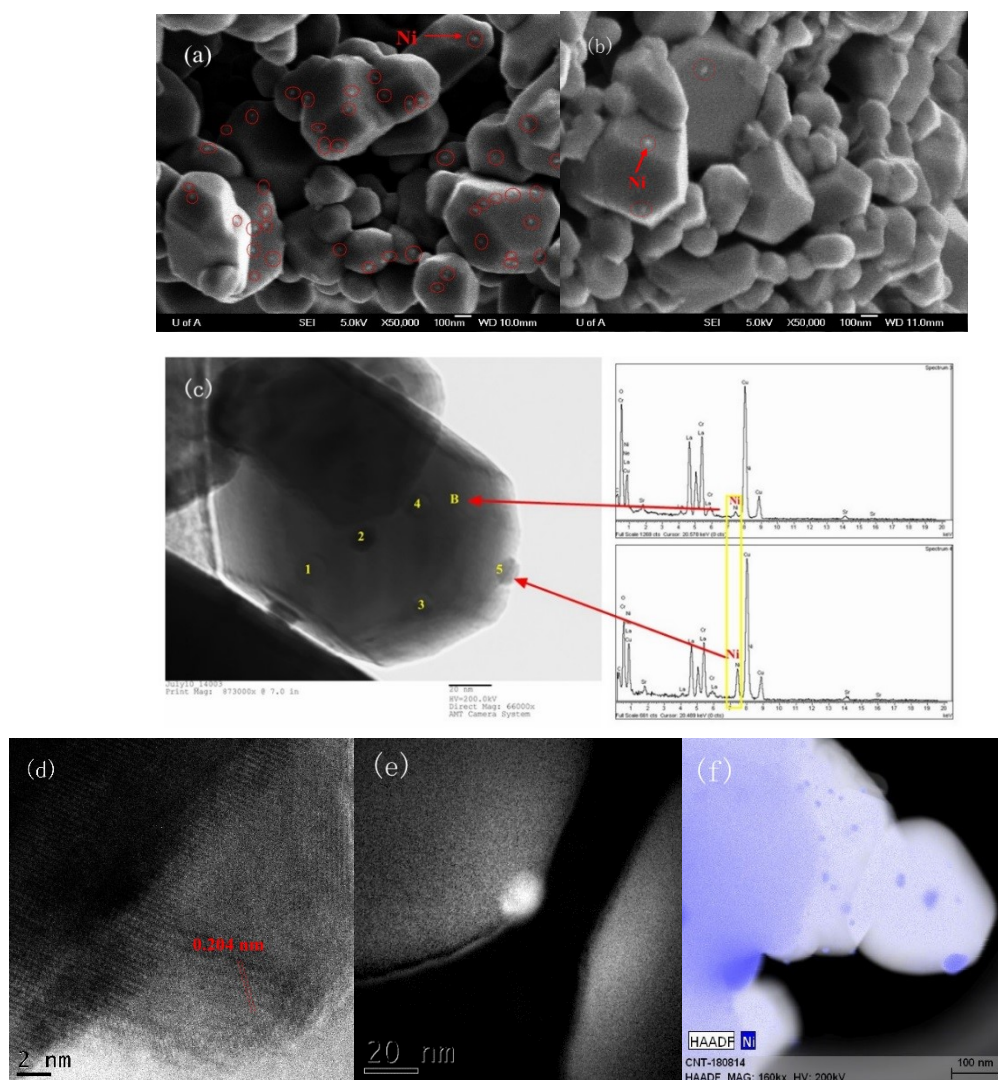


**Fig.5- 3 Scanning electron microscopy (SEM), energy-dispersive X-ray spectroscopy (EDX), transmission electron microscopy (TEM), energy filtered TEM (EFTEM) and high angle annular dark field (HAADF) images for 63LSCNi-15 and 73LSCNi-15 samples. SEM images for (a) 63LSCNi-15 and (b) 73LSCNi-15 materials reduced at 800 °C for 4 h. (c) EDX analysis for point 5 and B of TEM image of 63LSCNi-15 on the left side of (c). (d) TEM micrograph of the exsolved nano-particle anchored on bulk material. (e) EFTEM image of a Ni particle. (f) HAADF image of a 63LSCNi-15 particle overlaid with EDX elemental map of Ni-highlighting nanoparticles.**

overlaid with EDX elemental map of Ni-highlighting nanoparticles. The presence of well-dispersed bright spots with high density corresponds to the exsolved Ni nanoparticles on the perovskite scaffold, which is consistent with the observations described above.

To assess the electrochemical performance of 63LSCNi-15 and 73LSCNi-15 anodes, the I-V and power density curves of the fuel cells with 63LSCNi-15 and 73LSCNi-15 anodes were measured using H<sub>2</sub> and 5000 ppm H<sub>2</sub>S-H<sub>2</sub> as the fuels at 800 °C and the results are shown in Figures 5-4 (a) and (b), respectively.

In H<sub>2</sub> fuel, the maximum power density of the cell with 63LSCNi anode was 309 mW cm<sup>-2</sup>, which was about four times higher than that obtained from the 73LSCNi anode. By comparison of Figures 5-4 (a) and (b), it is clear that the addition of H<sub>2</sub>S enhanced the anode activity and provided better cell performance. The maximum power density of the 63LSCNi-15 cell tested in 5000 ppm H<sub>2</sub>S-H<sub>2</sub> at 800 °C was about 460 mW cm<sup>-2</sup> with the maximum current density higher than 1200 mA cm<sup>-2</sup>. The SOFCs with a 73LSCNi-15 anode only generated a power density output of 135 mW cm<sup>-2</sup> with the maximum current density < 300 mA cm<sup>-2</sup>. The promoting effect of H<sub>2</sub>S for the oxidation of H<sub>2</sub> on perovskite-based anodes for SOFCs has been demonstrated and discussed elsewhere (17-19). One possible mechanism is that H<sub>2</sub>S may serve as an effective carrier for H<sub>2</sub> to react with oxygen ions through forming H-S-O since the decomposition of H<sub>2</sub>S (363 KJ mol<sup>-1</sup>) is easier than that via breaking the H-H bond (436 KJ mol<sup>-1</sup>) directly.

Figure 5-4(c) shows the corresponding EIS of 73LSCNi-15 and 63LSCNi-15 fuel cells fueled with 5000 ppm H<sub>2</sub>S-H<sub>2</sub> at 800 °C. All the EIS data were obtained only after the cell had reached steady state. Obviously, both anode catalysts were active for the conversion of H<sub>2</sub>, and the introduction of A-site deficiency significantly improved the cell performance. The electrolyte resistance of each cell was ~ 0.3 Ω cm<sup>2</sup>. The activation polarization resistance of the 63LSCNi-15 anode measured in 5000 ppm H<sub>2</sub>S-H<sub>2</sub> at 800 °C was about 0.26 Ω cm<sup>2</sup> that was only 1/6 of that of 73LSCNi-15, meaning that the A-site deficiency could remarkably improve the electrochemical performance of the anode because of the larger amount of Ni particles with high catalytic activity.

It is well recognized that one of the biggest challenges for Ni-based cermet anodes is its poor redox stability. Although the anode material is kept in reducing atmospheres during operation, the re-oxidation of Ni to NiO could occur because of imperfect sealing of the anode chamber or unexpected shutdown of the operating system. As the accumulated NiO occupies more volume than Ni particles,(20) such dimensional change after redox cycles would result in the formation and propagation of micro-cracks across the anode and electrolyte, leading to degraded performance or full failure of the SOFC cell. Based on the XRD characterization (Figure 5-1), it can be seen that A-site deficient materials exhibited high structural redox stability upon exposure to oxidizing and reducing atmospheres.

To test the redox stability of the 63LSCNi-15 anode in H<sub>2</sub>S containing fuel, the cell was periodically treated with 5000 ppm H<sub>2</sub>S-H<sub>2</sub> at 800 °C for 24 h, followed by a

recovery process of *in situ* treatment in 5% O<sub>2</sub>/N<sub>2</sub> for 2 h. The reason behind using oxygen treatment is that it can be more effective than H<sub>2</sub>O in terms of removing the sulfur atoms adsorbed onto the Ni surface(21). Subsequently, the fuel of 5000 ppm H<sub>2</sub>S-H<sub>2</sub> was introduced for 30 min to reach a stable state before the next cycle test. Figure 5-4 (e) shows the maximum power density of the cell with 63LSCNi-15 anode in four redox cycles with total test duration of more than 100 h. In the first cycle, the cell had an initial power density of 460 mW cm<sup>-2</sup> and final density of 340 mW cm<sup>-2</sup> after 24 h treatment in 5000 ppm H<sub>2</sub>S-H<sub>2</sub>. The degradation may be due to the sintering of exsolved metal nanoparticles and the coverage of active sites by sulfur. After the cell was treated in an oxidizing atmosphere for 2 h, the cell performance was restored to the initial power density level (~ 460 mW cm<sup>-2</sup>), as shown in the Figure 5-4(e), suggesting that the exsolved nanoparticle could re-dissolve into the lattice to return to its oxidized state and the absorbed sulfur be oxidized and removed. When the fuel was introduced again, the nano Ni particle re-exsolved out of the lattice again and the performance can be completely regenerated. During the four redox cycles, the cell could be fully recovered by *in situ* treatment without noticeable degradation in power generation.

Figure 5-4(e) is the EIS spectra of 63LSCNi-15 anode before and after four redox cycles at 800 °C. No obvious increase in the polarization resistance or the ohmic resistance was found. The results confirmed that the catalyst could be fully regenerated and the microstructure of 63LSCNi-15 is strongly tolerant to redox cycles. Otherwise, cracks would occur across the cell, resulting in an increase in ohmic resistance.

To evaluate the generality of this strategy, Co and Fe doped LSC perovskite anodes were also prepared using the same experimental procedure stated in this paper and their electrochemical performances were assessed in 5000 ppm H<sub>2</sub>S-H<sub>2</sub> (not shown in Figures). The results clearly reiterate that the A-site deficient perovskite anodes exhibit much better catalytic activity than those without A-site deficiency. Therefore, this approach is a promising way to synthesize a variety of functional perovskite materials with high electrochemical performance and attractive redox stability.

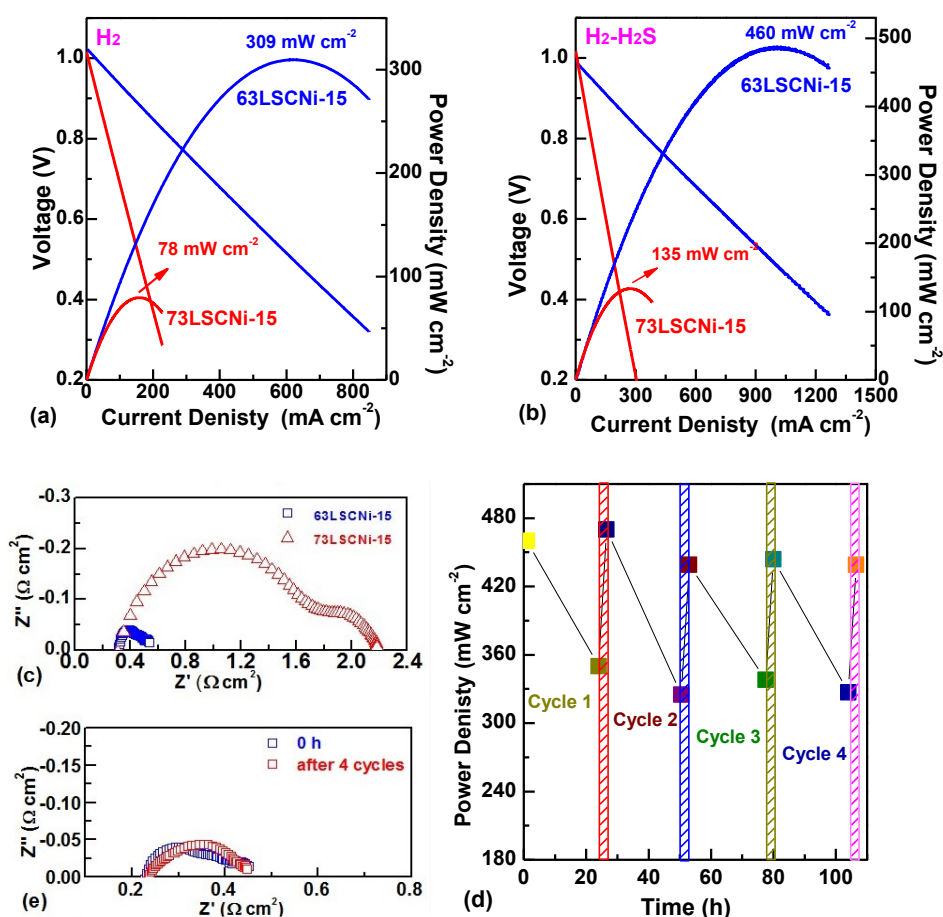


**Fig.5- 4 Fuel cell performances with the various anodes in H<sub>2</sub> or 5000 ppm H<sub>2</sub>S-H<sub>2</sub>. Current density–voltage and power density curves for fuel cells with 63LSCNi-15 and 73LSCNi-15 anodes using (a) pure H<sub>2</sub> fuel and (b) 5000 ppm**

**H<sub>2</sub>S-H<sub>2</sub> fuel at 800 °C. (c) EIS for the cells with 63LSCNi-15 and 73LSCNi-15 anodes fueled with 5000 ppm H<sub>2</sub>S-H<sub>2</sub> at 800 °C. (d) The redox test results for 63LSCNi-15-YSZ/YSZ/YSZ-LSCF fuel cell at 800 °C during four 26 h-cycles. In each cycle, the cell was treated with 5000 ppm H<sub>2</sub>S-H<sub>2</sub> for 24 h and then recovered via the in situ treatment of 5% O<sub>2</sub>/N<sub>2</sub> for 2 h (hatched period). Then the fuel was introduced again and the power density was measured after the introduction of fuel for 30 min. (e) The comparison of EIS results for the cell using 63LSCNi-15 anode before and after 4 redox cycle test in (d).**

#### 5.4 Discussion

An excellent anode material for SOFCs should meet the requirements of high catalytic activity for oxidation of fuel, high ionic and electronic conductivities, and good redox stability. In our investigation, the enhancement of electrochemical performance of 63LSCNi-15 anode could be firstly attributed to the exsolution of the widely dispersed nano Ni particles. The introduction of A-site deficiency alters the stoichiometric composition to help the exsolution of Ni in B-site. For A-site deficient anode, the main driving force of Ni exsolution is the decrease in Gibbs free energy [Figure 5-1(c)] through the reduction of Ni from its oxidized state in the chromite lattice. Then, Ni precipitates onto its surface in a reducing atmosphere since Ni is thermodynamically unstable in the LaCrO<sub>3</sub> lattice at 800 °C and P<sub>O<sub>2</sub></sub><10<sup>-14</sup> atm (10).

The single-phase LSC is expected to tolerate only a few percentages of A-site or B-site non-stoichiometry. The stoichiometric materials with a certain amount of exsolution of B-site cations would be reasonably regarded as ones with B-site deficiency. To compare the tolerance of different anode materials to B-site deficiency, XRD characterizations were conducted on the stoichiometric and non-stoichiometric materials with different concentrations of B-site deficiency, the results are shown in Figure 5-5 (a). The initial concentrations of Ni in A-site deficient material ( $\text{La}_{0.6}\text{Sr}_{0.3}\text{Cr}_{0.85}\text{Ni}_{0.15}\text{O}_{3-\xi}$ ) and in stoichiometric material ( $\text{La}_{0.7}\text{Sr}_{0.3}\text{Cr}_{0.85}\text{Ni}_{0.15}\text{O}_{3-\xi}$ ) are assumed to be equal to 15%. Once 5%, 10% or 15% of Ni in stoichiometric materials was exsolved, the B-site deficiency could form, and the materials were denoted as  $\text{La}_{0.7}\text{Sr}_{0.3}\text{Cr}_{0.85}\text{Ni}_{0.1}\text{O}_{3-\xi}$  (73LSCNi-10),  $\text{La}_{0.7}\text{Sr}_{0.3}\text{Cr}_{0.85}\text{Ni}_{0.05}\text{O}_{3-\xi}$  (73LSCNi-5) and  $\text{La}_{0.7}\text{Sr}_{0.3}\text{Cr}_{0.85}\text{O}_{3-\xi}$  (73LSC). Similarly, the A-site deficient materials with various Ni contents could be denoted as  $\text{La}_{0.6}\text{Sr}_{0.3}\text{Cr}_{0.85}\text{Ni}_{0.1}\text{O}_{3-\xi}$  (63LSCNi-10),  $\text{La}_{0.6}\text{Sr}_{0.3}\text{Cr}_{0.85}\text{Ni}_{0.05}\text{O}_{3-\xi}$  (63LSCNi-5) and  $\text{La}_{0.7}\text{Sr}_{0.3}\text{Cr}_{0.85}\text{O}_{3-\xi}$  (63LSC). From the XRD patterns, it can be seen that the LSCNi with A-site deficiency exhibited pure perovskite structure with the B-site deficiency concentration up to 15% and there was no diffraction peak of any impurity, i.e., the 63LSCNi-15 material can maintain perovskite structure even with the exsolution of all the Ni. On the contrary, diffraction peaks of La/Sr-enriched phase ( $\text{LaSrO}_{2.5}$ ) were found for stoichiometric material with B-site deficiency concentration higher than 5%, implying that the theoretical maximum exsolution capability for stoichiometric material is 5%. Previous research has revealed

that the 73LSCNi-5 material could still sustain the perovskite structure after treatment in H<sub>2</sub>/Ar at 900 °C without the formation of impurity phases (22). My experiment confirmed this conclusion that the maximum capacity of B-site deficiency for stoichiometric perovskite is 5%. Therefore, it can be inferred that exsolution of more Ni on A-site deficient perovskite is favorable.

In addition to facilitation of the exsolution of catalytically active nano-Ni, the promoted diffusion of oxygen in the lattice could be regarded as another important reason for the enhancement of performance. Figure 5-5(b) is a schematic of the generation of oxygen vacancies and the exsolution process for perovskite with A-site deficiency. During the treatment in a reducing atmosphere, the oxygen vacancies would be introduced, which destabilized the perovskite lattice and resulted in the spontaneous exsolution of B-site species. Another possible process is that the oxygen vacancies and B-site cation vacancies could also be simultaneously introduced by the treatment in a reducing atmosphere and then the metal oxide could be converted to corresponding metal exsolved from the lattice. As shown in Figure 5-2 (b), the amount of oxygen vacancies in A-site deficient perovskite was much higher than that in the perovskite with stoichiometric composition, leading to better ionic conductivity as well as a larger amount of exsolved Ni. It is worth mentioning that the exsolution of metallic Ni would also increase electronic conductivity of the material, which in turn makes a contribution to the better performance of the material. The enhanced conductivity of A-site deficient materials will be confirmed in our future work.

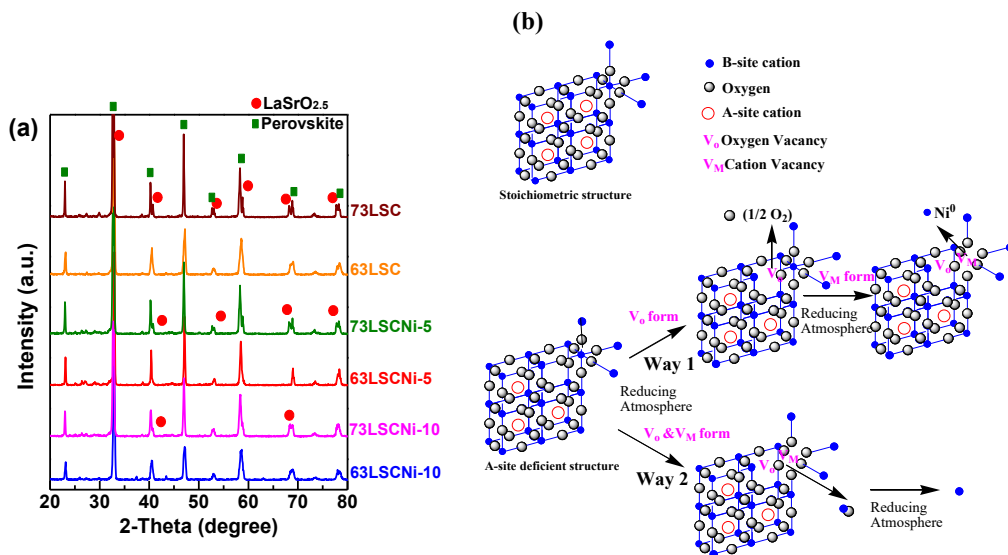


**Fig.5- 5 (a) XRD patterns for the materials with various concentrations of A-site or B-site deficiency. (b) The schematic of generation of oxygen vacancies and Ni exsolution process for perovskite with A-site deficiency. The simulated figure was drawn using ChemDraw 8.0.**

Last but not least, previous research has shown that the A-site deficient perovskite sinters much better and yields larger grains which provide more available hopping sites for cations and further promote ion diffusion (23). Thus, another reason for the excellent performance of the A-site deficient perovskite is that the diffusion of nickel ions could be facilitated, resulting in more metallic nickel particles being exsolved out.

Compared to the traditional Ni-based anode materials, the A-site deficient perovskite not only exhibits comparable electrochemical performance but also shows desirable redox stability in sour fuel; achieving both in sour fuel was once considered one of great challenges for the Ni/YSZ anode. The XRD results have demonstrated that after exposure to an oxidizing atmosphere, the reduced materials were turned into perovskite again without the formation of impurities, indicating that the exsolved

metallic Ni had dissolved into the perovskite lattice. The phenomenon of the movement of Ni into and out of the lattice upon redox cycling was also found by other researchers (7, 24, 25). The unique characteristic of redox stability of the material in both sweet and sour gases reported in this work suggests that it may be applicable to utilize redox cycling to fully recover performance loss for fuel cells after prolonged reaction.

## 5.5 Conclusions

Ni-doped LSC perovskite oxide anodes with A-site deficiency were successfully prepared. The A-site deficiency plays a key role in driving the exsolution of Ni in B-sites, resulting in a significant enhancement in the diffusion of lattice oxygen and the exsolution of Ni<sup>2+</sup> to metallic Ni<sup>0</sup>. The A-site deficient LSCNi materials exhibit promising electrochemical performance and attractive redox stability in 5000 ppm H<sub>2</sub>S-H<sub>2</sub>. Furthermore, the generality of this anode preparation method can be applied for the exsolution of other active transition metals. Therefore, this approach presents a promising way to greatly improve the catalytic properties and stability of electrode materials. The significance of the material characteristics presented in this paper lies in the much broader application potential of the methodology for fabricating next generation electrode materials in the fields of energy conversion and energy storage in general.

## 5.6 References

1. Tanaka H, Taniguchi M, Uenishi M, Kajita N, Tan I, Nishihata Y, et al. Self-regenerating Rh- and Pt-based perovskite catalysts for automotive-emissions control. *Angewandte Chemie*. 2006;45(36):5998-6002.
2. Nishihata Y, Mizuki J, Akao T, Tanaka H, Uenishi M, Kimura M, et al. Self-regeneration of a Pd-perovskite catalyst for automotive emissions control. *Nature*. 2002;418(6894):164-7.
3. Jiang SP. Nanoscale and nano-structured electrodes of solid oxide fuel cells by infiltration: Advances and challenges. *International Journal of Hydrogen Energy*. 2012;37(1):449-70.
4. Lee S, Kim G, Vohs JM, Gorte RJ. SOFC Anodes Based on Infiltration of  $\text{La}_{0.3}\text{Sr}_{0.7}\text{TiO}_3$ . *Journal of The Electrochemical Society*. 2008;155(11):B1179.
5. Lu J, Fu B, Kung MC, Xiao G, Elam JW, Kung HH, et al. Coking- and sintering-resistant palladium catalysts achieved through atomic layer deposition. *Science*. 2012;335(6073):1205-8.
6. Lintanf A. Pt/YSZ electrochemical catalysts prepared by electrostatic spray deposition for selective catalytic reduction of NO by C<sub>3</sub>H<sub>6</sub>. *Solid State Ionics*. 2008;178(39-40):1998-2008.

7. Adijanto L, Balaji Padmanabhan V, Kungas R, Gorte RJ, Vohs JM. Transition metal-doped rare earth vanadates: a regenerable catalytic material for SOFC anodes. *Journal of Materials Chemistry*. 2012;22(22):11396-402.
8. Arrivé C, Delahaye T, Joubert O, Gauthier G. Exsolution of nickel nanoparticles at the surface of a conducting titanate as potential hydrogen electrode material for solid oxide electrochemical cells. *Journal of Power Sources*. 2013;223:341-8.
9. Vert VB, Melo FV, Navarrete L, Serra JM. Redox stability and electrochemical study of nickel doped chromites as anodes for H<sub>2</sub>/CH<sub>4</sub>-fueled solid oxide fuel cells. *Applied Catalysis B: Environmental*. 2012;115-116:346-56.
10. Kobsiriphat W, Madsen BD, Wang Y, Shah M, Marks LD, Barnett SA. Nickel- and Ruthenium-Doped Lanthanum Chromite Anodes: Effects of Nanoscale Metal Precipitation on Solid Oxide Fuel Cell Performance. *Journal of The Electrochemical Society*. 2010;157(2):B279.
11. Neagu D, Tsekouras G, Miller DN, Menard H, Irvine JT. In situ growth of nanoparticles through control of non-stoichiometry. *Nature chemistry*. 2013;5(11):916-23.
12. Yaqub A, Janjua NK, Savaniu C, Irvine JTS. Synthesis and characterization of B-site doped La<sub>0.20</sub>Sr<sub>0.25</sub>Ca<sub>0.45</sub>TiO<sub>3</sub> as SOFC anode materials. *International Journal of Hydrogen Energy*. (0).

13. Wang Y, Wang L, Gan N, Lim Z-Y, Wu C, Peng J, et al. Evaluation of Ni/Y<sub>2</sub>O<sub>3</sub>/Al<sub>2</sub>O<sub>3</sub> catalysts for hydrogen production by autothermal reforming of methane. *International Journal of Hydrogen Energy*. 2014;39(21):10971-9.
14. Li W, Reimers JN, Dahn JR. In situ x-ray diffraction and electrochemical studies of Li<sub>1-x</sub>NiO<sub>2</sub>. *Solid State Ionics*. 1993;67(1-2):123-30.
15. Jahangiri A, Aghabozorg H, Pahlavanzadeh H. Effects of Fe substitutions by Ni in La-Ni-O perovskite-type oxides in reforming of methane with CO<sub>2</sub> and O<sub>2</sub>. *International Journal of Hydrogen Energy*. 2013;38(25):10407-16.
16. Rida K, Peña MA, Sastre E, Martinez-Arias A. Effect of calcination temperature on structural properties and catalytic activity in oxidation reactions of LaNiO<sub>3</sub> perovskite prepared by Pechini method. *Journal of Rare Earths*. 2012;30(3):210-6.
17. Cui S-H, Li J-H, Zhou X-W, Wang G-Y, Luo J-L, Chuang KT, et al. Cobalt doped LaSrTiO<sub>3-δ</sub> as an anode catalyst: effect of Co nanoparticle precipitation on SOFCs operating on H<sub>2</sub>S-containing hydrogen. *Journal of Materials Chemistry A*. 2013;1(34):9689.
18. Roushanafshar M, Luo J-L, Vincent AL, Chuang KT, Sanger AR. Effect of hydrogen sulfide inclusion in syngas feed on the electrocatalytic activity of LST-YDC composite anodes for high temperature SOFC applications. *International Journal of Hydrogen Energy*. 2012;37(9):7762-70.

19. Li J-H, Fu X-Z, Luo J-L, Chuang KT, Sanger AR. Application of BaTiO<sub>3</sub> as anode materials for H<sub>2</sub>S-containing CH<sub>4</sub> fueled solid oxide fuel cells. *Journal of Power Sources*. 2012;213:69-77.
20. Ettler M, Timmermann H, Malzbender J, Weber A, Menzler NH. Durability of Ni anodes during reoxidation cycles. *Journal of Power Sources*. 2010;195(17):5452-67.
21. Wang J-H, Liu M. Surface regeneration of sulfur-poisoned Ni surfaces under SOFC operation conditions predicted by first-principles-based thermodynamic calculations. *Journal of Power Sources*. 2008;176(1):23-30.
22. Sauvet AL, Irvine JTS. Catalytic activity for steam methane reforming and physical characterisation of La<sub>1-x</sub>Sr<sub>x</sub>Cr<sub>1-y</sub>Ni<sub>y</sub>O<sub>3-δ</sub>. *Solid State Ionics*. 2004;167(1-2):1-8.
23. Neagu D, Irvine JTS. Enhancing Electronic Conductivity in Strontium Titanates through Correlated A and B-Site Doping. *Chemistry of Materials*. 2011;23(6):1607-17.
24. Tanaka H, Taniguchi M, Uenishi M, Kajita N, Tan I, Nishihata Y, et al. Self-Regenerating Rh- and Pt-Based Perovskite Catalysts for Automotive-Emissions Control. *Angewandte Chemie International Edition*. 2006;45(36):5998-6002.
25. Bierschenk DM, Potter-Nelson E, Hoel C, Liao Y, Marks L, Poepelmeier KR, et al. Pd-substituted (La,Sr)CrO<sub>3-δ</sub>-Ce<sub>0.9</sub>Gd<sub>0.1</sub>O<sub>2-δ</sub> solid oxide fuel cell

anodes exhibiting regenerative behavior. *Journal of Power Sources*.  
2011;196(6):3089-94.

## **Chapter 6. *In-situ* growth of nano Ni-Fe alloy on A-site deficient Sr doped LaCrO<sub>3</sub> perovskite: A novel carbon deposition and sulfur tolerant anode for solid oxide fuel cells (SOFCs)**

### 6.1 Introduction

Various strategies have been applied to modify and enhance the performance of Ni based anodes and the addition of a second metal was widely investigated (1-3), which can tune catalytic performances through alternation and modification of electronic or structural parameters of the anode materials (4). Usually, the host and guest metals can form a bimetallic alloy which shows a synergetic effect or bi-functional effect (5-8). Among the various metal additions, iron has been widely studied not only because of its easy accessibility but also its effective performance in enhancing the catalytic activity of Ni-based anodes. Pasciak and co-workers reported that anode supported SOFCs with Ni-Fe ( Ni:Fe. 3:1 in molar ratio) bimetal and gadolinia-doped ceria (GDC) composite anodes could generate the highest power density of 1.33 W cm<sup>-2</sup> at 650 °C (9). Ishihara investigated the NiO-Fe<sub>3</sub>O<sub>4</sub> (Ni:Fe, 90:10 in molar ratio) and Sm-doped ceria (SDC) composite anode and found that the maximum power density of the single cell with Sr and Mg-doped LaGaO<sub>3</sub> (LSGM) thin film electrolyte and Sm<sub>0.5</sub>Sr<sub>0.5</sub>CoO<sub>3</sub> (SSC55) cathode could achieve 1.95 W cm<sup>-2</sup> at 600 °C (10). Lu et al. (11) reported the performance YSZ electrolyte supported SOFC with Ni-Fe alloy (Ni:Fe, 7:3 in molar ratio) anode and La<sub>0.8</sub>Sr<sub>0.2</sub>MnO<sub>3</sub> (LSM) cathode showed a

maximum power density of  $0.4 \text{ Wcm}^{-2}$  at  $900 \text{ }^\circ\text{C}$ . In addition to its promoting effect for electrocatalytic activity, an appropriate amount of additive iron to a Ni-based anode has also been proven to enhance the tolerance against carbon deposition, while the cells were running on hydrocarbon fuels. The addition of 10% Fe to a Ni+GDC anode significantly enhanced the stability of the cell to reach 50 h without degradation. In contrast, Ni-GDC showed obvious potential drop after 12 hours operation under the same condition (12). Gao et al. (13) found that the  $\text{Ni-Fe-La}_{0.8}\text{Sr}_{0.2}\text{Ga}_{0.8}\text{Mg}_{0.115}\text{Co}_{0.085}\text{O}_3$  anodes showed good activity and stability for dimethyl ether (DME) oxidation without obvious coke deposition. Fiuza et al.(14) also found that adding iron to nickel to form a Fe-Ni/YSZ-GDC anode could obviously inhibit carbon deposition for in ethanol steam reforming reaction. In the meanwhile, the investigation also revealed that the preparation method also had big influence on the tolerance of the material against carbon deposition. Consequently, it can be inferred that the fabrication method may also play a key role on the performance of an alloy electrode.

Previous researches have demonstrated a variety of synthesis methods for Ni-Fe alloy catalysts including the physical mixing method, the Pechini method and the glycine nitrite process (GNP) (11, 12, 14), which showed the advantages of low cost and simple synthesis process. However, these methods can only fabricate catalysts with the particles in the scale of micrometer, which limits the surface area and restricts the number of active sites. Consequently, the catalytic performances are usually low. The impregnation method is another kind of widely used and effective way (15). However,

the promotion effect of Fe on Ni was significantly influenced by the infiltration processes, such as heat-treatment temperature, and distribution of loading of the infiltrated phase. Besides, the different interactions between infiltrated phase and scaffold lead to discrepancies in the enhancing effect, which is another big issue to be addressed via optimization. Therefore, the infiltration method still faces the problems of complicated or even uncontrollable processes.

Recently, an advanced strategy has been developed and applied to prepare perovskite oxides with the decoration of uniform-distributed nano metallic particles. In this process, diverse reducible elements could be doped into the B-site during the calcination process and partly in-situ exsolved out of the lattice in a reducing atmosphere. It is reported that this method has been successfully used to synthesize  $\text{La}_{0.52}\text{Sr}_{0.28}\text{Ni}_{0.06}\text{Ti}_{0.94}\text{O}_3$  perovskite oxides(16) and Fe and Ni doped  $\text{La}_{0.2}\text{Sr}_{0.25}\text{Ca}_{0.45}\text{TiO}_3$  (LSCTA) perovskite (17) which all exhibited the exsolution of a large amount of nano particles on the surface of the perovskite oxide in a reducing atmosphere. The investigations also revealed that the exsolution phenomenon on A-site deficient perovskite has the promising perspective to be utilized in designing the catalysts for a wide range of fields including electrodes materials for SOFCs. Previous work done by our group has illustrated that Ni could preferably exsolve on A-site deficient lanthanum strontium chromite perovskite and these functional materials showed much higher electrochemical performance in sweet and sour fuel than stoichiometric materials. However, up to this date, all the research efforts have focused

on the A-site deficient perovskite with monometallic dopant and no investigation on the perovskite decorated with nano alloy particle has been published.

Therefore, in this study, a series of A-site deficient perovskite anode catalysts with Ni and Fe dopants has been synthesized and their electrochemical performances in different fuels were evaluated. In addition, the characteristics of Ni-Fe bimetallic catalysts were also investigated in detail in order to fully understand the synergetic effect between Ni and Fe in nano alloy.

## 6.2 Experimental Procedure

The glycine nitrate combustion method was used to fabricate the Ni- and/or Fe-doped lanthanum strontium chromite anode materials, which are denoted as LSCNi, LSCFe and LSCNi-Fe, respectively. The Ni, Fe or Ni-Fe (mol ratio of Ni:Fe = 3:1) dopant contents in the total B-site cations were equal to 15 mol%. Certain amounts of  $\text{La}(\text{NO}_3)_2 \cdot 6\text{H}_2\text{O}$ ,  $\text{Sr}(\text{NO}_3)_2$ ,  $\text{Ni}(\text{NO}_3)_2 \cdot 6\text{H}_2\text{O}$ ,  $\text{Fe}(\text{NO}_3)_3 \cdot 9\text{H}_2\text{O}$ ,  $\text{Cr}(\text{NO}_3)_3 \cdot 9\text{H}_2\text{O}$  and glycine were first dissolved in deionized water. The molar ratio of glycine to the total content of the metal cations was 2:1. The solution was stirred thoroughly and then heated on a hot plate at 500°C until self-combustion occurred. The powders were ground and further calcined at 1100°C for 3 h to generate different anode materials. The designations of each material are shown as follow: LSCNi for  $(\text{La}_{0.7}\text{Sr}_{0.3})(\text{Cr}_{0.85}\text{Ni}_{0.15})\text{O}_{3-x}$ , LSCFe for  $(\text{La}_{0.7}\text{Sr}_{0.3})(\text{Cr}_{0.85}\text{Fe}_{0.15})\text{O}_{3-x}$ , and LSCNi-Fe for  $(\text{La}_{0.7}\text{Sr}_{0.3})(\text{Cr}_{0.85}(\text{Ni}_3\text{Fe}_1)_{0.15})\text{O}_{3-x}$ , respectively.

### 6.3 Results

The XRD patterns for the fresh anode materials are shown in Figure 6-1(a). It is clearly shown that both the monometallic dopant and bimetallic dopants have no influence on the chemical structure of the material. Additionally, all materials exhibit a perovskite structure without impurities. The XRD profiles of all reduced materials are shown in Figure 6-1 (b), and the materials are denoted as R-LSCNi, R-LSCFe and R-LSCNi-Fe. It is shown that after reduction in 5% H<sub>2</sub>/N<sub>2</sub> at 800 °C for 4 h, a metallic Fe phase was detected for R-LSCFe only as indexed in the figure. For the R-LSCNi sample, a diffraction peak that can be attributed to metallic Ni was observed in the XRD profile. It is known that Fe and Ni are adjacent to each other in the periodic table, thus, they can easily form a solid solution phase with various ratios. For the R-LSCNi-Fe sample with Ni:Fe=3:1, The diffraction peak belonging to an intermetallic compound of Awaruite FeNi<sub>3</sub> (JCPDS38-0419) was found in the structure. Combined with the XRD patterns for LSCNi and LSCFe, it can be inferred that the metallic Fe and Ni may firstly form on the LSCNi-Fe sample and then generate the alloy.

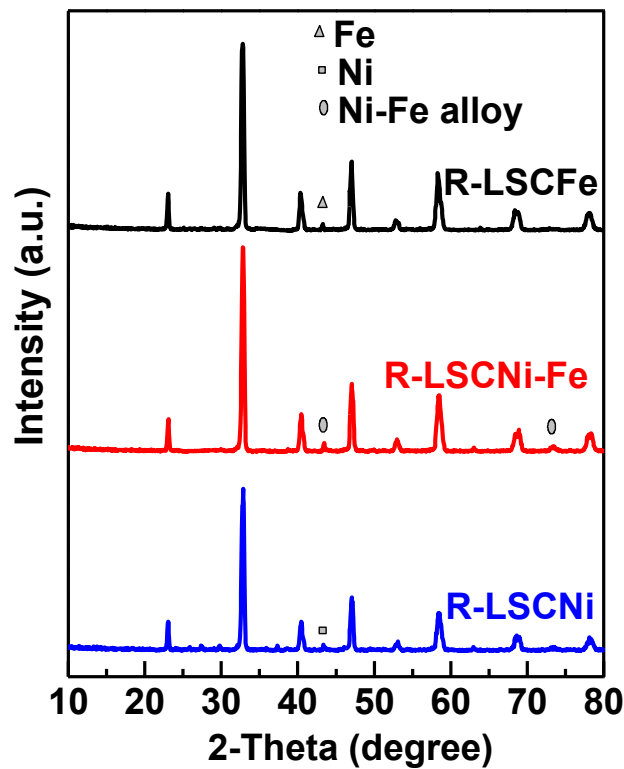
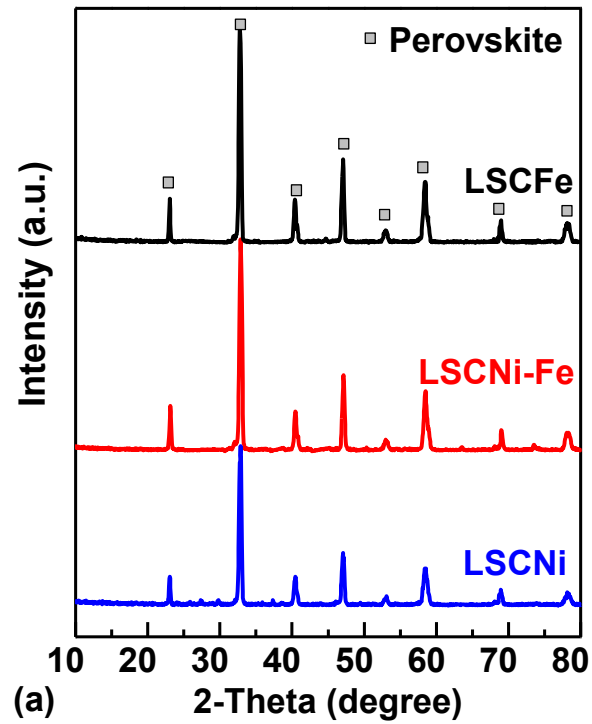


Fig.6-1 XRD patterns for (a) fresh anode materials and (b) reduced anode materials. All materials were reduced in 5% H<sub>2</sub>/N<sub>2</sub> at 800 °C for 4 h.

### 3.2 H<sub>2</sub>-TPR

The reducibility of Fe and Ni in each perovskite oxide and the synergistic effect between Fe and Ni were characterized using H<sub>2</sub>-TPR technology, and the corresponding results are plotted in Figure 6-2. The curve of LSCNi exhibits two H<sub>2</sub> consumption peaks at ~520 °C and 620°C. It has been previously reported that the reduction behavior of Ni consists of two stages including an  $\alpha$ -peak at a lower temperature (~500 °C) due to the reduction of Ni<sup>3+</sup> into Ni<sup>2+</sup>, and a  $\beta$ -peak at a higher temperature (~600 °C) that is associated with the reduction of Ni<sup>2+</sup> into metallic Ni [29, 30]. For Fe-doped perovskite, the reduction profile for the LSCFe sample shows three groups of multiple peaks from 400°C to 600°C, which can be attributed to the reduction of Fe<sup>3+</sup> to Fe<sup>2+</sup>, Fe<sup>2+</sup> to Fe<sup>0</sup> and Fe<sup>3+</sup> to Fe<sup>0</sup>, respectively [31]. With the addition of Fe to Ni, the Ni-Fe bimetallic material only exhibits one H<sub>2</sub> consumption peak at ~500°C. This phenomenon indicates that the formation of the Ni-Fe composite significantly changes the reduction behavior of the Ni and Fe oxides, and the two different metals were reduced simultaneously, which should be regarded as evidence for the formation of the alloy for the bimetallic catalysts [32, 33].

Theoretically, based on the Ni-Fe phase diagram in Figure 6-3 [34], at least one regular alloy with the composition of Ni<sub>3</sub>Fe could be formed under this experimental condition. However, under the same condition, alloys with the composition of NiFe and Ni<sub>3</sub>Fe<sub>2</sub> and Ni<sub>2</sub>Fe have also been reported [35-37]. A previous report has demonstrated that a significant fraction of iron on supported catalysts could be alloyed with nickel

simply after treatment in H<sub>2</sub> [38]. Consequently, it can be inferred that the formation of alloy under this experimental condition is favorable.

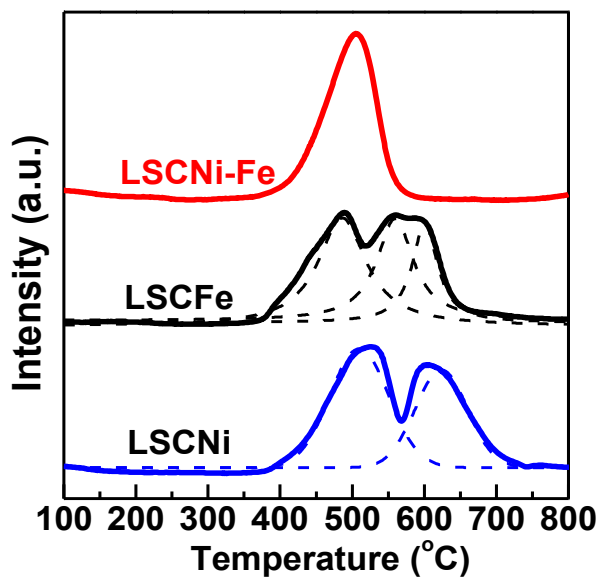


Fig.6-2 . H<sub>2</sub>-TPR profiles for different anode materials.

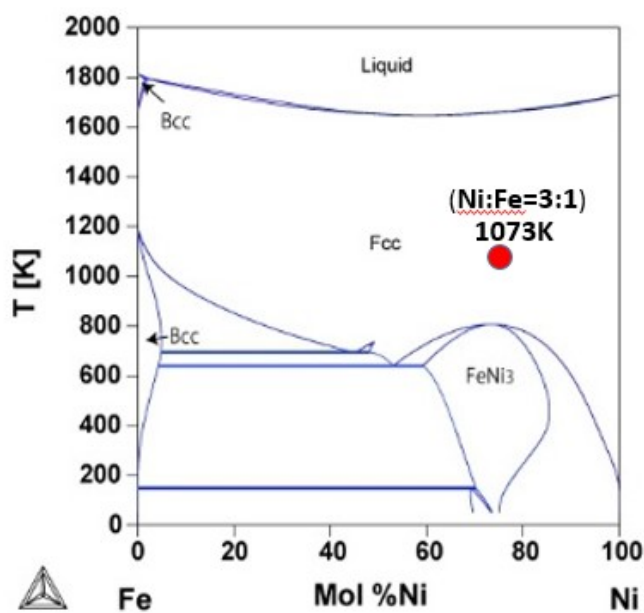
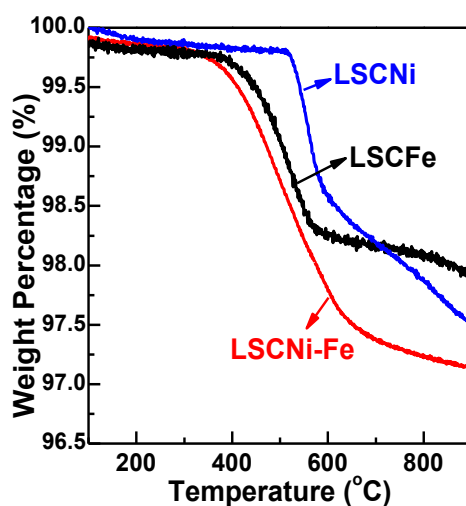


Fig.6-3 . Phase diagram of bimetallic Ni-Fe system<sup>34</sup>.

### 3.3 TGA

The TGA measurements for the different samples were conducted in 5% H<sub>2</sub>/N<sub>2</sub> from 100°C to 900°C, and the corresponding curves are shown in Figure 6-4. The weight loss is primarily due to the formation of oxygen vacancies, namely the reduction of metal oxide and escape of oxygen ions. The LSCNi sample started to lose weight at 515°C and showed a total weight loss of ~2.5%. The results of the LSCFe material show that its weight loss began at ~400°C and exhibited a total weight loss percentage of 2%. In comparison, the formation process of oxygen vacancies from the lattice of LSCNi-Fe started at a temperature similar to that of LSCFe. However, the total weight loss percentage is close to 3%, which is significantly higher than that of LSCFe and LSCNi. These results indicate that the formation of an alloy facilitates the formation of oxygen vacancies and further benefits the exsolution of both Ni and Fe.



**Fig.6-4 TGA curves of the fresh LSCNi, LSCFe and LSCNi-Fe samples measured in 5% H<sub>2</sub>/N<sub>2</sub>.**

### 3.4 TEC

During SOFC operation, the cell experiences high temperatures for a prolonged period of time. Therefore, the TECs of the electrode and the electrolyte should be similar in order to minimize the thermal stress in the SOFC stacks as much as possible. To determine the mechanical compatibility of the fabricated bimetallic perovskite anodes with the YSZ electrolyte used in a fuel cell, a thermal expansion measurement was performed in air. Figure 6-5 shows the TECs for the fabricated anode and the YSZ electrolyte from 400 K to 1200 K. The TEC of the YSZ electrolyte is shown to be  $\sim 11 \times 10^{-6} \text{ K}^{-1}$  throughout the temperature range regardless of the oxygen partial pressure; the LSCNi-Fe is shown to have a TEC of  $\sim 10.7 \times 10^{-6} \text{ K}^{-1}$ , which is similar to that of the YSZ, indicating that the LSCNi-Fe anode is a suitable candidate for use as an SOFC electrode.

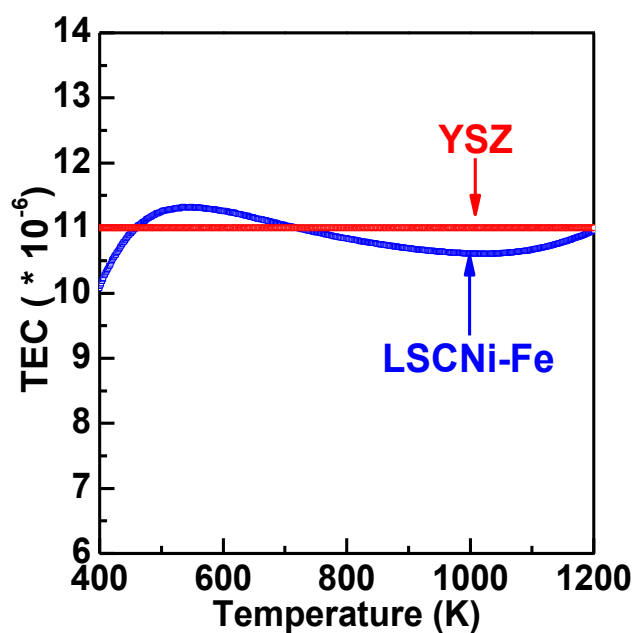
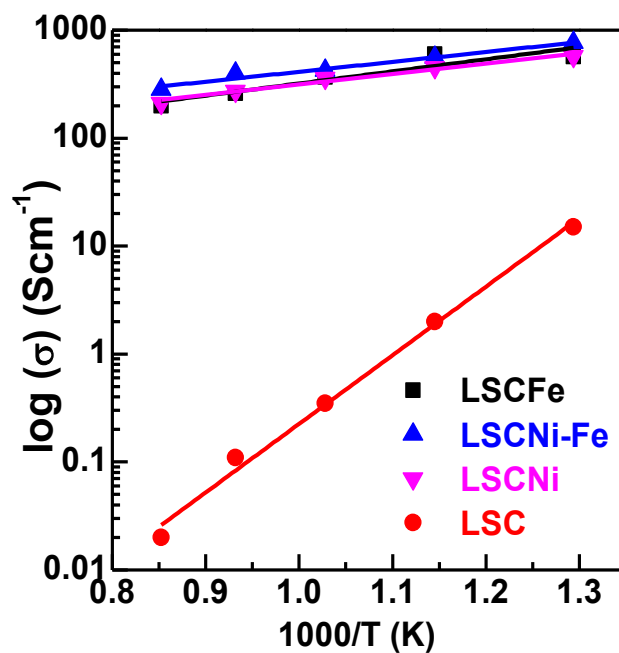


Fig.6-5 TECs of LSCNi-Fe and YSZ materials in air from 400 K to 1200 K.

### 3.5 Conductivity

The electrical conductivities of the materials in air are shown in Figure 6-6 as a function of temperature. For comparison, data for LSC without any substitutions are also included in Figure 6-6(a). In each test, the measurement was conducted for 30 minutes to reach equilibrium. Additionally, as expected, all samples exhibited a linear metallic conductivity behavior, suggesting that the electrical conductivity behavior is a thermally activated process that obeys the small polaron conductivity mechanism

The enhanced electrical conductivity of all doped materials can be simply explained by the formation of oxygen vacancies after the substitution of low valence metals (e.g.,  $\text{Ni}^{2+}$  and  $\text{Fe}^{2+}$ ) for  $\text{Cr}^{3+}$ , which facilitates the transportation of electrons. It is also shown that the LSCNi-Fe material shows a higher conductivity at higher temperatures compared to LSCNi and LSCFe. A similar phenomenon has been reported with Co- and Ni-Co-doped  $\text{La}_{0.85}\text{Sr}_{0.15}\text{CrO}_3$  perovskite [39]. It is postulated that the higher conductivity is related to the interaction between the Ni and Fe ions with higher mobilities at elevated temperature.



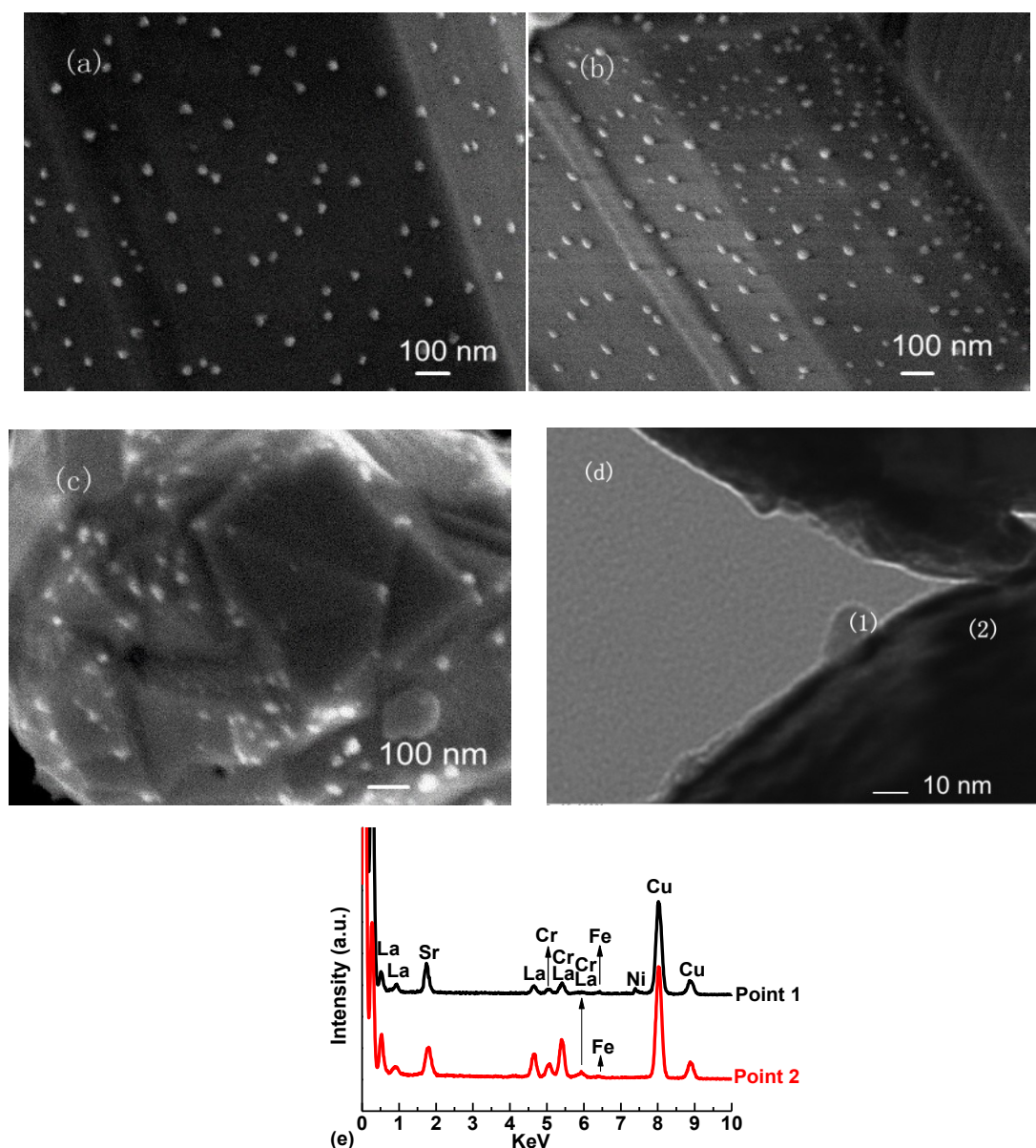
**Fig.6-6 Electrical conductivities of various materials in air (a) and in 5% $H_2/N_2$  (b) as a function of temperature.**

### 3.6 SEM and TEM

The SEM images of the reduced LSCNi, LSCFe and LSCNi-Fe samples are shown in Figure 6-7 (a), (b) and (c), respectively. All samples have been pre-treated in 5%  $H_2-N_2$  at 800°C for 4 h and all the reduced samples show well-distributed nano particles covering the surface of the perovskite matrix. The average diameter of the particles is ~25 to 30 nm. In comparison, figures 6-7(f) and (g) exhibit the SEM images for LSC materials reduced at 800 °C for 4h and LSCNi-Fe material before reduction. Clearly, no exsolution of any metallic nano particles could be found on the surface the materials.

A TEM image for the LSCNi-Fe sample is shown in Figure 6-7 (d). Exsolution of the nano alloy particles with diameter of ~25 nm is shown at the edge of the perovskite parent. The presence and distribution of Ni and Fe within one individual alloy particle

were further verified using the TEM-EDX spectrum. As shown in Figure 6-7 (e), the chemical composition of the bulk material (point 2) was significantly different from the nano particle (point 1), where the significant peaks can be attributed to Ni and Fe, indicating the presence of the Ni-Fe alloy. By comparison, the intensities of the peaks for Fe and Ni are relatively weak. The SEM and TEM results thus agree with the XRD and H<sub>2</sub>-TPR results, which indicates the presence of the Ni-Fe alloy.



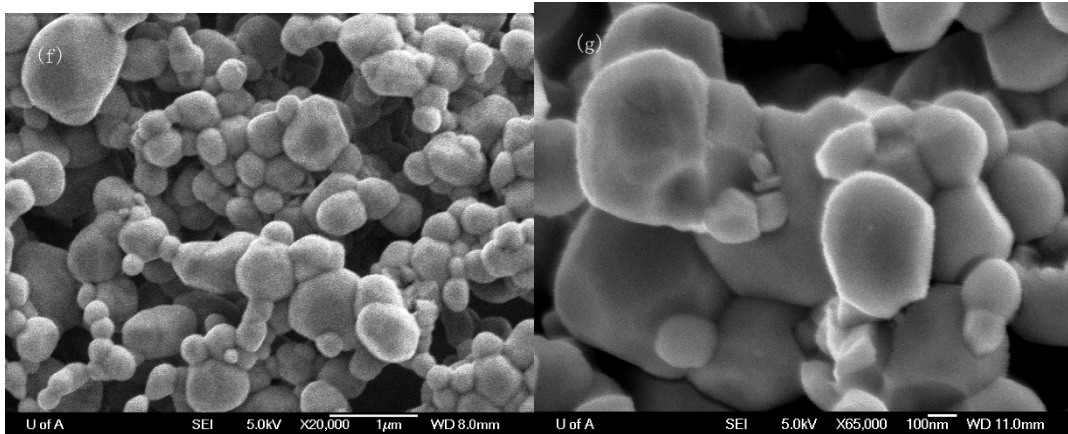


**Fig.6-7 SEM images for the (a) LSCNi (b) LSCFe and (c) LSCNi-Fe materials reduced at 800oC for 4 h; (d) TEM micrograph of the exsolved nano-particle anchored to the bulk LSCNi-Fe material; (e) EDX analysis for points 1 and 2 on the TEM image shown in (d). (f) and (g) are the SEM images for the LSC materials reduced at 800 oC for 4 h and LSCNi-Fe material before reduction, respectively.**

### 3.7 Electrochemical performance

The detailed I-V and power density curves for the fuel cells with different anodes operating in 5000 ppm H<sub>2</sub>S-H<sub>2</sub> are shown in Figure 6-8(a). The maximum power densities (MPD) of the fuel cells with a LSCNi anode and a LSCFe anode were 460 mW cm<sup>-2</sup> with a maximum current density (MCD) of ~1300 mA cm<sup>-2</sup>, and 360 mW cm<sup>-2</sup> with an MCD of ~1000 mA cm<sup>-2</sup>, respectively. In comparison, a fuel cell with a LSCNi-Fe bimetallic anode could generate an MPD of 560 mW cm<sup>-2</sup> with an MCD of ~1700 mA cm<sup>-2</sup>. These results imply that all of the tested anode catalysts have sufficient catalytic activities for the oxidation of hydrogen.

To create a clear comparison of the electrochemical performances of the various cells tested, the EIS of the cells fueled with 5000 ppm H<sub>2</sub>S-H<sub>2</sub> at 800°C under OCV conditions were also measured and are shown in Figure 6-8(b). At the same reaction conditions were also measured and are shown in Figure 6-8(b). At the same reaction temperature, the electrolyte resistance of each cell was  $\sim 0.3 \Omega \text{ cm}^2$ . The activation polarization resistances of the LSCNi, LSCFe and LSCNi-Fe fuel cells were 0.35, 0.25 and  $0.2 \Omega \text{ cm}^2$ , respectively, indicating that the addition of Fe to Ni decreases the activation polarization resistance of the anode. This is likely the primary reason for the observed improvement in electrochemical performance.

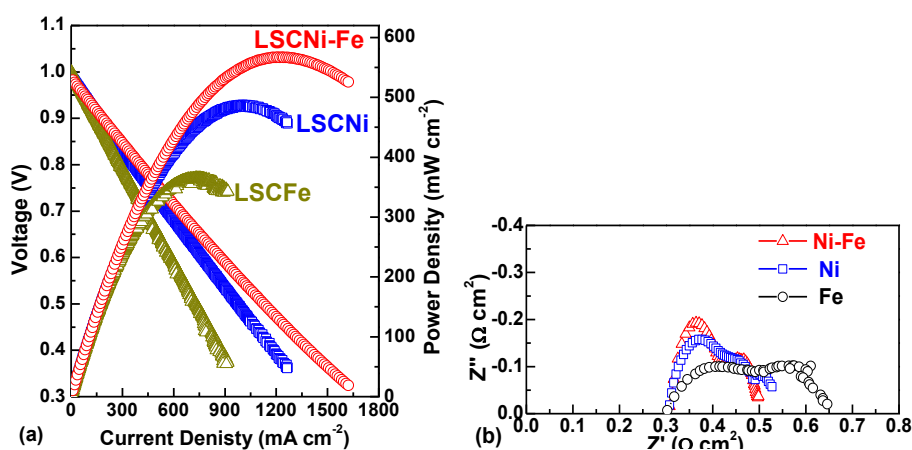


**Fig.6-8 (a) Current density vs. voltage and power density curves, and (b) electrochemical impedance spectra for fuel cells with LSCNi, LSCFe and LSCNi-Fe anodes using 5000 ppm H<sub>2</sub>S-H<sub>2</sub> fuel at 800°C.**

The electrochemical performances of LSCNi-Fe fuel cells fed with 5000 ppm H<sub>2</sub>S-syngas are demonstrated by the I-V and power density curves shown in Fig. 6-9 (a). The OCV values at each temperature are similar to their theoretical values. As the reaction temperature rose from 750°C to 850°C, the MPD output and MCD values

increased from 210 to 400 mW cm<sup>-2</sup> and from 680 mA cm<sup>-2</sup> to 1300 mA cm<sup>-2</sup>, respectively. These results demonstrate that the LSCNi-Fe anode has good activity to catalyze the oxidation reaction of syngas.

The impedance data of a single cell with an LSCNi-Fe anode measured under OCV conditions between 750 to 850°C are given in Figure 6-9 (b). The best fitting results to the equivalent circuit of LR<sub>Ω</sub>(R<sub>1</sub>Q<sub>1</sub>)(R<sub>2</sub>Q<sub>2</sub>) for all EIS have been obtained, where R<sub>Ω</sub> represents the pure ohmic resistance. Each of the parallel circuits with resistance R<sub>i</sub> and constant phase element Q<sub>i</sub> accounts for the respective depressed semicircle going from high to low frequencies. A parasitic inductance L was added to consider the contribution of the equipment. This fitting result indicates that two different electrode processes corresponding to the high- and low-frequency arcs control the electrochemical reaction. The total polarization resistance of the cell (R<sub>p</sub>) can be expressed by the sum of R<sub>1</sub> and R<sub>2</sub>. The fitted impedance parameters of the cell at different temperatures under OCV conditions are plotted in Figure 6-10. The apparent activation energies of the polarization resistances in the low and high frequency ranges and the total polarization resistance were calculated to be 22.4, 98.4 and 62.1 KJ mol<sup>-1</sup>, respectively. The apparent activation energy of the ohmic resistance was found to be 49.5 KJ mol<sup>-1</sup>. These activation energy results further show that the increase in cell performance was primarily due to the electrochemical kinetics of the electrode.

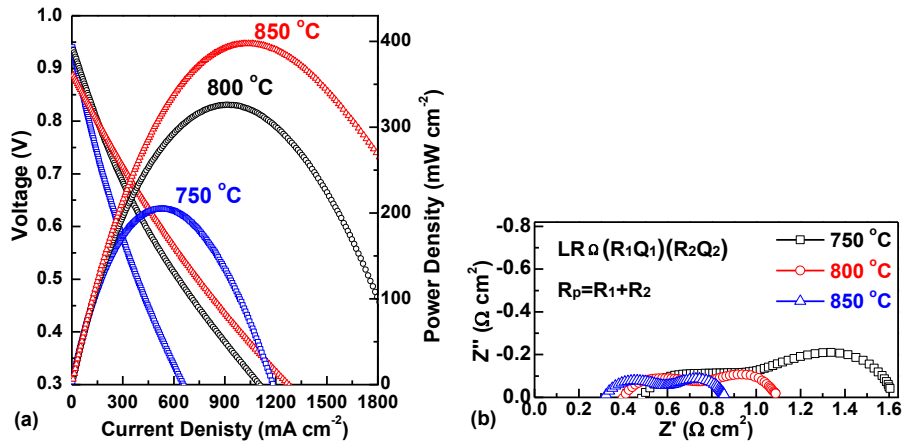


**Fig.6-9 (a) Current density vs. voltage and power density curves, and (b) electrochemical impedance spectra for fuel cells with an LSCNi-Fe anode using 5000 ppm H<sub>2</sub>S-syngas fuel at different temperatures.**

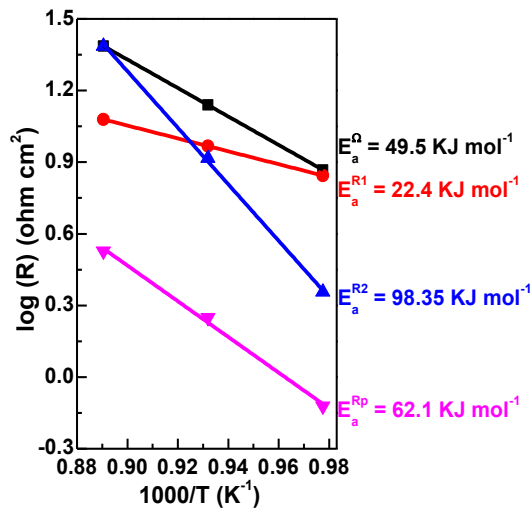


**Fig.6- 10 Electrochemical impedance spectra of a fuel cell with an LSCNi-Fe anode measured in 5000 ppm H<sub>2</sub>S-syngas between 750°C and 850°C under open-circuit conditions. Arrhenius plot of the resistances measured at different temperatures.**

### 3.8 Resistance against carbon deposition

In addition to the catalytic activity, the resistance to carbon deposition is another important parameter for the evaluation of the functional anode materials used in

hydrocarbon fuels. Previous studies have claimed that Ni is prone to carbon deposition, and Fe has a better tolerance to coking<sup>19</sup>. Figure 6-11 shows the O<sub>2</sub>-TPO profiles of various fresh materials after treatment with syngas for 24 h at 850°C.

The CO<sub>2</sub> peak areas were  $3.1 \times 10^{-7}$ ,  $1.63 \times 10^{-7}$ , and  $6.1 \times 10^{-9}$  for LSCNi, LSCNi-Fe and LSCFe, respectively. Based on these results, it can be concluded that the addition of Fe effectively suppresses the formation of carbon deposition on the material. However, it can also be found by comparing the curves that the peak position of the CO<sub>2</sub> of the material shifts from 650°C to ~590°C when Fe is added to LSCNi. For LSCFe, the location of the primary peak is ~450 °C. Based on previous studies of the density functional theory (DFT) calculation, a bi-metallic alloy can preferentially remove carbon deposition on the surface of the electro-catalyst rather than facilitate the formation of carbon-carbon bonds, as monometallic Ni does [18, 40]. This conclusion is consistent with our experimental results, which show that the introduction of Fe significantly facilitates the removal of carbon deposits.

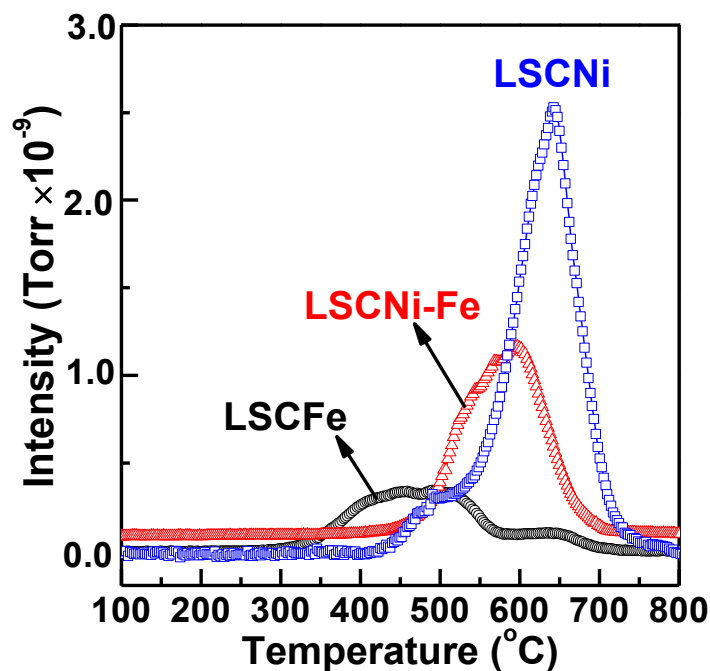


Fig.6- 11. TPO curves of various materials treated with syngas in 850°C for 24 h.

#### 6.4 Discussion

A-site-deficient LSC perovskite with co-doping of Ni and Fe was successfully fabricated, and the phenomenon of *in situ* exsolution of the nano Ni-Fe alloy was detected at SOFC operating conditions. The bimetallic anode has been identified as being catalytically active in sour gas and significantly more carbon tolerant than monometallic Ni anodes. The XRD patterns for fresh samples show that after sintering, all dopants have dissolved into the perovskite lattice, and no impurities are present in the fresh samples. The *in situ* treatment with the reducing atmosphere on the samples forces the reducible ions (e.g., Fe and Ni) to exsolve out of the lattice to form metallic nano particles. This process has been identified by the XRD results for the reduced samples.

Compared to a monometallic catalyst, the LSCNi-Fe sample showed multiple steps of the reduction process. It is postulated that in the first step, the  $\text{Ni}^{2+}$  and  $\text{Fe}^{3+}$  or  $\text{Fe}^{2+}$  are synchronously reduced to form Ni and Fe, anchored to the surface of the perovskite, respectively. Based on the description in the experimental procedures, the stoichiometric ratio of Ni to Fe is 3:1. The phase diagram shows that formation of the Ni-Fe alloy with a ratio of 3:1 is thermodynamically favorable under these reduction conditions. Consequently, it is reasonable to conclude that the exsolved Fe and Ni migrate to the surface at similar diffusion velocities to form the Ni-Fe alloy in the second step because they have approximately the same Tammann temperature. Thus, the aggregation of metallic Ni and metallic Fe occurs simultaneously during the process of alloy formation. However, the XRD results for the reduced samples did not show any significant diffraction peaks that could be attributed to Ni and Fe. In this case, these particles likely exist with sizes below the detection limitation of XRD analysis.

The formation of the alloy has a significant influence on the reducibility of the Fe and Ni, which is shown in the results of the  $\text{H}_2$ -TPR and TGA analyses in the reducing atmosphere. Only one wide  $\text{H}_2$  consumption peak from 380°C to 600°C is shown for the LSCNi-Fe sample, which could be attributed to the similar reduction behavior of Ni and Fe. In comparison, the monometallic catalyst has reduction peaks only between 400°C and 700°C. The shift of the reduction peaks to lower temperatures indicates that the formation of the alloy facilitates the exsolution of Ni and Fe out of the lattice. Additionally, the results of the TGA analysis suggest the promotion effect on the

reduction of metals; the temperature at which the LSCNi-Fe began to lose weight is ~380 °C. This value is consistent with the results in the TPR analysis and is lower than that of the monometallic catalysts. The bimetallic material shows a total weight loss of 3%, which is 20% and 33% higher than those of LSCNi and LSCFe, respectively, demonstrating that a larger amount of metal combined with more oxygen vacancies form during this process. Both of these two factors will benefit the electrochemical reaction and further enhance the catalytic performance of the material.

However, co-doping of Ni and Fe in the LSC perovskite is shown to enhance the electrical conductivity of the material because charge compensation (e.g., Cr<sup>3+</sup> to Cr<sup>4+</sup>) occurs after the doping of low valence metals into B sites for partial substitution of Cr<sup>3+</sup> to ensure charge neutralization within the materials and create more charge carriers. In addition, the exsolution of the metals contributes to electron transport during the reaction. As a result, the electrochemical performance tends to be improved.

Additionally, it is widely accepted that carbon deposition may block the pores and cover the reaction sites in the material, influencing fuel diffusion and leading to a decrease in catalytic activity. The results of the calculation of the activation energy ( $E_a$ ) for each polarization resistance behavior show that the rate-determining step of the reaction is the fuel diffusion ( $R_2$ ) for the LSCNi-Fe and LSCNi materials, which have an  $E_a$  of 98.35 KJ mol<sup>-1</sup> and 121.83 KJ mol<sup>-1</sup>, respectively. The TPO results show that the LSCNi-Fe anode has a better carbon deposition tolerance than the LSCNi anode.

The addition of Fe decreases the activation energy for fuel diffusion by suppressing the formation of carbon deposition. Consequently, the performance tends to be enhanced.

## 6 Conclusions

The Ni- and Fe-co-doped LSC bimetallic perovskite anode material with A-site deficiencies was successfully prepared by the glycine combustion method. The exsolution of the Ni-Fe nano alloy was detected on the *in situ* reduced samples using SEM and TEM. The TGA and H<sub>2</sub>-TPR profiles showed that the addition of Fe helped create more oxygen vacancies and promoted the reducibility of the materials. The anode material with the exsolved Ni-Fe alloy showed a desirable electrical conductivity, electrochemical performance in sour H<sub>2</sub> and syngas, and better resistance to carbon deposition compared to a Ni monometallic anode.

## 6.5 References

1. Kitla A, Safonova OV, Fottinger K. Infrared Studies on Bimetallic Copper/Nickel Catalysts Supported on Zirconia and Ceria/Zirconia. *Catal Letters*. 2013;143(6):517-30.
2. Gonzalez-delaCruz VM, Pereñíguez R, Ternero F, Holgado JP, Caballero A. In Situ XAS Study of Synergic Effects on Ni–Co/ZrO<sub>2</sub> Methane Reforming Catalysts. *The Journal of Physical Chemistry C*. 2012;116(4):2919-26.
3. Grgicak CM, Pakulska MM, O'Brien JS, Giorgi JB. Synergistic effects of Ni<sub>1-x</sub>Co<sub>x</sub>-YSZ and Ni<sub>1-x</sub>Cu<sub>x</sub>-YSZ alloyed cermet SOFC anodes for oxidation

of hydrogen and methane fuels containing H<sub>2</sub>S. *Journal of Power Sources*. 2008;183(1):26-33.

4. Tao F. Synthesis, catalysis, surface chemistry and structure of bimetallic nanocatalysts. *Chemical Society Reviews*. 2012;41(24):7977-9.

5. Lu ZG, Zhu JH, Bi ZH, Lu XC. A Co–Fe alloy as alternative anode for solid oxide fuel cell. *Journal of Power Sources*. 2008;180(1):172-5.

6. Ringuedé A, Labrincha JA, Frade JR. A combustion synthesis method to obtain alternative cermet materials for SOFC anodes. *Solid State Ionics*. 2001;141–142(0):549-57.

7. An W, Gatewood D, Dunlap B, Turner CH. Catalytic activity of bimetallic nickel alloys for solid-oxide fuel cell anode reactions from density-functional theory. *Journal of Power Sources*. 2011;196(10):4724-8.

8. Huang B, Wang SR, Liu RZ, Wen TL. Preparation and performance characterization of the Fe–Ni/ScSZ cermet anode for oxidation of ethanol fuel in SOFCs. *Journal of Power Sources*. 2007;167(2):288-94.

9. Fu CJ, Chan SH, Ge XM, Liu QL, Pasciak G. A promising Ni–Fe bimetallic anode for intermediate-temperature SOFC based on Gd-doped ceria electrolyte. *International Journal of Hydrogen Energy*. 2011;36(21):13727-34.

11. Lu XC, Zhu JH, Bi ZH. Fe alloying effect on the performance of the Ni anode in hydrogen fuel. *Solid State Ionics*. 2009;180(2–3):265-70.

12. Kan H, Lee H. Enhanced stability of Ni–Fe/GDC solid oxide fuel cell anodes for dry methane fuel. *Catalysis Communications*. 2010;12(1):36-9.
13. Shi-zhong W, Jie G. High Performance Ni - Fe - Lanthanum Gallate Composite Anodes for Dimethyl Ether Fuel Cells. *Electrochemical and Solid-State Letters*. 2006;9(9):A395-A8.
14. da Paz Fiuza R, Aurélio da Silva M, Boaventura JS. Development of Fe–Ni/YSZ–GDC electrocatalysts for application as SOFC anodes: XRD and TPR characterization and evaluation in the ethanol steam reforming reaction. *International Journal of Hydrogen Energy*. 2010;35(20):11216-28.
15. Jiang SP. Nanoscale and nano-structured electrodes of solid oxide fuel cells by infiltration: Advances and challenges. *International Journal of Hydrogen Energy*. 2012;37(1):449-70.
16. Neagu D, Tsekouras G, Miller DN, Menard H, Irvine JT. In situ growth of nanoparticles through control of non-stoichiometry. *Nature chemistry*. 2013;5(11):916-23.
17. Yaqub A, Janjua NK, Savaniu C, Irvine JTS. Synthesis and characterization of B-site doped  $\text{La}_{0.20}\text{Sr}_{0.25}\text{Ca}_{0.45}\text{TiO}_3$  as SOFC anode materials. *International Journal of Hydrogen Energy*. (0).
1. Kitla A, Safonova OV, Fottinger K. Infrared Studies on Bimetallic Copper/Nickel Catalysts Supported on Zirconia and Ceria/Zirconia. *Catal Letters*. 2013;143(6):517-30.

2. Gonzalez-delaCruz VM, Pereñiguez R, Ternero F, Holgado JP, Caballero A. In Situ XAS Study of Synergic Effects on Ni–Co/ZrO<sub>2</sub>Methane Reforming Catalysts. *The Journal of Physical Chemistry C*. 2012;116(4):2919-26.
3. Grgicak CM, Pakulska MM, O'Brien JS, Giorgi JB. Synergistic effects of Ni<sub>1-x</sub>Co<sub>x</sub>-YSZ and Ni<sub>1-x</sub>Cu<sub>x</sub>-YSZ alloyed cermet SOFC anodes for oxidation of hydrogen and methane fuels containing H<sub>2</sub>S. *Journal of Power Sources*. 2008;183(1):26-33.
4. Tao F. Synthesis, catalysis, surface chemistry and structure of bimetallic nanocatalysts. *Chemical Society Reviews*. 2012;41(24):7977-9.
5. Lu ZG, Zhu JH, Bi ZH, Lu XC. A Co–Fe alloy as alternative anode for solid oxide fuel cell. *Journal of Power Sources*. 2008;180(1):172-5.
6. Ringuedé A, Labrincha JA, Frade JR. A combustion synthesis method to obtain alternative cermet materials for SOFC anodes. *Solid State Ionics*. 2001;141–142(0):549-57.
7. An W, Gatewood D, Dunlap B, Turner CH. Catalytic activity of bimetallic nickel alloys for solid-oxide fuel cell anode reactions from density-functional theory. *Journal of Power Sources*. 2011;196(10):4724-8.
8. Huang B, Wang SR, Liu RZ, Wen TL. Preparation and performance characterization of the Fe–Ni/ScSZ cermet anode for oxidation of ethanol fuel in SOFCs. *Journal of Power Sources*. 2007;167(2):288-94.

9. Fu CJ, Chan SH, Ge XM, Liu QL, Pasciak G. A promising Ni–Fe bimetallic anode for intermediate-temperature SOFC based on Gd-doped ceria electrolyte. *International Journal of Hydrogen Energy*. 2011;36(21):13727-34.
10. <NI-FE-LSGM.pdf>.
11. Lu XC, Zhu JH, Bi ZH. Fe alloying effect on the performance of the Ni anode in hydrogen fuel. *Solid State Ionics*. 2009;180(2–3):265-70.
12. Kan H, Lee H. Enhanced stability of Ni–Fe/GDC solid oxide fuel cell anodes for dry methane fuel. *Catalysis Communications*. 2010;12(1):36-9.
13. Shi-zhong W, Jie G. High Performance Ni - Fe - Lanthanum Gallate Composite Anodes for Dimethyl Ether Fuel Cells. *Electrochemical and Solid-State Letters*. 2006;9(9):A395-A8.
14. da Paz Fiuza R, Aurélio da Silva M, Boaventura JS. Development of Fe–Ni/YSZ–GDC electrocatalysts for application as SOFC anodes: XRD and TPR characterization and evaluation in the ethanol steam reforming reaction. *International Journal of Hydrogen Energy*. 2010;35(20):11216-28.
15. Jiang SP. Nanoscale and nano-structured electrodes of solid oxide fuel cells by infiltration: Advances and challenges. *International Journal of Hydrogen Energy*. 2012;37(1):449-70.
16. Neagu D, Tsekouras G, Miller DN, Menard H, Irvine JT. In situ growth of nanoparticles through control of non-stoichiometry. *Nature chemistry*. 2013;5(11):916-23.

17. Yaqub A, Janjua NK, Savaniu C, Irvine JTS. Synthesis and characterization of B-site doped  $\text{La}_{0.20}\text{Sr}_{0.25}\text{Ca}_{0.45}\text{TiO}_3$  as SOFC anode materials. International Journal of Hydrogen Energy. (0).

## **Chapter 7. A-site deficient chromite perovskite with in-situ exsolution of nano Fe : A promising bi-functional catalyst bridging growth of CNTs and SOFCs**

### 7.1 Introduction

The development of advanced devices that enhance the efficiency of fuel utilization has been a research focus for scientists worldwide in light of the impact of a potential energy crisis. SOFCs have been regarded as one of the most promising technologies which can continuously produce electricity as long as the fuel inputs are supplied. For the SOFCs fed with hydrocarbon such as methane, the fuel usually decomposes, at elevated temperature, to form amorphous carbon species which degrade the catalytic activity by blocking the active sites(1). To overcome this challenge, modification of the anode(2) and addition of water vapor to hydrocarbons (3) are the two main methods to mitigate the negative influence of coking.

In recent years, carbon nanotubes (CNTs) have drawn increasing attention since they were found to be able to significantly enhance the performance of various energy storage systems including super capacitors(4) and fuel cells.(5) In addition, the CNTs also exhibit attractive properties of high thermal conductivity and superior electrical conductivity, which accelerate heat transfer and increases the reaction rate during the electrochemical reactions (6, 7).

Catalytic chemical vapor deposition (CCVD) is the most widely accepted CNTs growth technology, in which a variety of active metals such as Ni, Fe, and Co(8, 9) as well as some of their corresponding alloys(10) play the role of being the localized growth sites for the prepared CNTs. Two steps involved in the process of CCVD consist of formation of active nanoparticles and the introduction of carbon sources. It was also revealed that the dimension parameters of CNTs are controlled by the size and distribution of metallic particles(11, 12). In-situ exsolution of metallic nanoparticles on perovskites(13) is regarded as a time-efficient and effective way to generate well-dispersed metallic particles compared to the traditional impregnation method. However, the exsolution amount was strongly restricted by the stoichiometric composition of perovskite. Recent research on A-site deficient perovskite found that alternation of the A/B ratio can noticeably facilitate the in-situ exsolution of well-dispersed metallic particles with uniform particle sizes(14). Therefore, the A-site deficient perovskite with uniform metallic particles strongly anchored on could be seen as a promising alternative catalyst for the growth of tailored CNTs.

So far, the information on the enhancing effect of MWCNTs on SOFCs is scarce. Only the addition of multiple-walled carbon nanotubes (MWCNTs) to  $\text{Pr}_{0.6}\text{Sr}_{0.4}\text{Fe}_{0.8}\text{Co}_{0.2}\text{O}_3$  (PSFC) perovskite cathode material was reported and it could control the size of nanoparticles, which reduced the area specific resistance of the material.(15) However, the fabrication process is complicated and time-consuming.

Herein, we report a novel fabrication method in which the iron doped lanthanum strontium chromite perovskite with A-site deficiency (A-LSCFe) was used to *in-situ* exsolve nano particles on which a considerable amount of MWCNTs are grown. The material thus fabricated was used as the anode catalyst for SOFC. The properties of the MWCNTs and the electrochemical performance of SOFCs were studied.

## 7.2 Experimental Procedure

The glycine nitrate combustion method was used to fabricate the  $\text{La}_{0.7}\text{Sr}_{0.3}\text{CrO}_{3-y}$ ,  $\text{La}_{0.7}\text{Sr}_{0.3}\text{Cr}_{0.85}\text{Fe}_{0.15}\text{O}_{3-\xi}$  and  $\text{La}_{0.6}\text{Sr}_{0.3}\text{Cr}_{0.85}\text{Fe}_{0.15}\text{O}_{3-\xi}$  anode materials for the fuel cell test, denoted as LSC, sto-LSCFe and A-LSCFe, respectively. Certain amounts of  $\text{La}(\text{NO}_3)_2 \cdot 6\text{H}_2\text{O}$ ,  $\text{Sr}(\text{NO}_3)_2$ ,  $\text{Fe}(\text{NO}_3)_3 \cdot 9\text{H}_2\text{O}$ ,  $\text{Cr}(\text{NO}_3)_3 \cdot 9\text{H}_2\text{O}$  and glycine were first dissolved in deionized water. The molar ratio of glycine to the total content of the metal cations was 2:1. The solution was stirred thoroughly and then heated on a hot plate at 500 °C until self-combustion started. The generated powders were ground and further calcined at 1300 °C in air for 3 h to produce different anode materials. All the prepared materials and their corresponding denotation are shown as follow, LSC for  $\text{La}_{0.7}\text{Sr}_{0.3}\text{CrO}_{3-\xi}$ , Sto-LSCFe for  $\text{La}_{0.7}\text{Sr}_{0.3}\text{Cr}_{0.85}\text{Fe}_{0.15}\text{O}_{3-\xi}$  and A-LSCFe for  $\text{La}_{0.6}\text{Sr}_{0.3}\text{Cr}_{0.85}\text{Fe}_{0.15}\text{O}_{3-\xi}$ , respectively.

## 7.3 Results and discussion

The crystallographic structure of the fresh and reduced compounds was examined by XRD Analysis of the data shows that both A-LSCFe and Sto-LSCFe as well as LSC

materials exhibit perovskite-type structure and all main peaks match well with those of  $\text{LaCrO}_3$  (JCPDS no.24-1016). Besides, no peak attributed to an impurity was detected. The A-site deficient LSCFe was treated in 5% $\text{H}_2$ - $\text{N}_2$  at 800 °C for 4 h (denoted as Re-A-LSCFe) and the XRD pattern for the corresponding material is also shown in Figure 7-1. It is found that the diffraction peak ascribed to metallic Fe could be detected, indicating the exsolution of metallic Fe. Scherrer formula was utilized to estimate the average size of nano iron particles, and the calculated result was  $\sim 26$  nm. Also, the A-LSCFe was mechanically mixed with YSZ and the mixture was sintered at 1000 °C and analyzed by XRD in order to test the compatibility between YSZ and A-LSCFe. The pattern in Figure 7-1 shows that only diffractions belonging to YSZ and A-LSCFe could be found and no peak assigned to an impurity could be detected, indicating their good chemical compatibility.

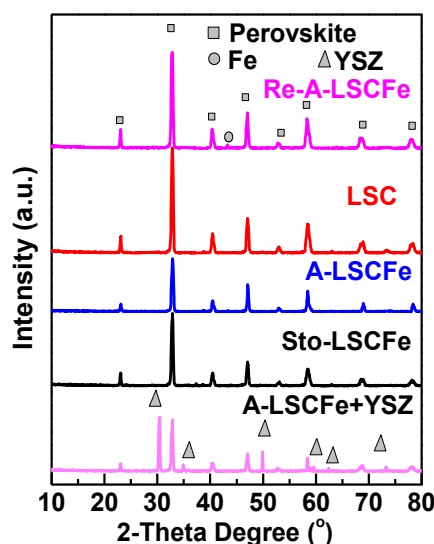


**Fig 7- 1. XRD patterns of fresh (LSC, A-LSCFe and Sto-LSCFe) and reduced (Re-A-LSCFe) materials.**

The H<sub>2</sub>-TPR analysis was conducted to evaluate the influence of A-site deficiency on the reducibility of Fe doped LSC materials. It can be obviously seen in Figure 7-2 that both A-LSCFe and sto-LSCFe materials exhibited the same shape and three multiple reduction peaks from 400 °C to 800 °C could be distinguished. Specifically, the first reduction peak at around 600 °C for Sto-LSCFe can be assigned to the reduction of Fe<sup>3+</sup> to Fe<sup>2+</sup> (16) and this process is combined with the formation of a certain amount of oxygen vacancies. Thermodynamically, this step is more likely to happen compared with the reduction of Fe<sup>3+</sup> and Fe<sup>2+</sup> to Fe directly. In comparison, this reduction peak shifts to a lower temperature zone at around 550 °C for A-LSCFe anode material, indicating that the reducibility of Fe in perovskite was enhanced and the creation of oxygen vacancies became easier. Similarly, the higher temperature multiple reduction peaks ascribed to Fe<sup>2+</sup> to Fe<sup>0</sup> and Fe<sup>3+</sup> to Fe<sup>0</sup>, respectively, also shifted backward by around 50 °C from 700 °C to 650 °C, when A-site deficiency was introduced to sto-LSCFe. This result suggests that reduction of Fe ions in B-sites to form metallic nano Fe could also be facilitated and the electrochemical performance could be further enhanced.

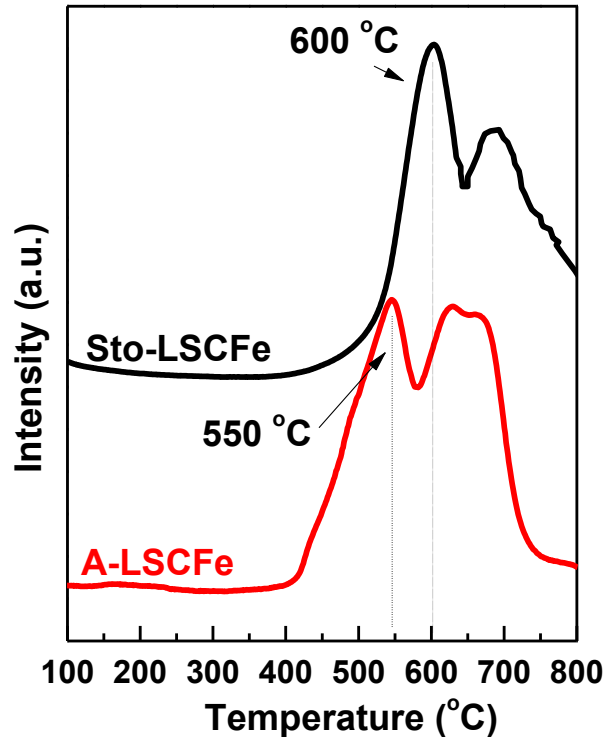


**Fig 7- 2. H<sub>2</sub>-TPR results of sto-LSCFe and A-LSCFe materials**

TGA analysis was conducted in 10%H<sub>2</sub>/N<sub>2</sub> for A-LSCFe and sto-LSCFe to evaluate the oxygen mobility and stability of the materials in a reducing atmosphere, and the curves are shown in Figure 7-3. The slight mass loss in the low temperature range lower than 400 °C is due to the loss of absorbed water, which may happen at room temperature. The A-LSCFe started to significantly lose weight at ~ 400 °C which is 100 °C lower than that of sto-LSCFe. The total weight loss percentage due to the formation of oxygen vacancies for A-LSCFe could reach 2.5 wt%. In comparison, the sto-LSCFe only showed 1.8 wt% weight loss, indicating that the introduction of A-site deficiency facilitates the mobility of oxygen and promotes the formation of oxygen vacancy. After ramping up to 800 °C, the system was stabilized at 800 °C for a prolonged stability test. The results shown in Figure 7-3 exhibit that there was no further

weight change during this period, suggesting that both materials are chemically stable under our reaction condition without the further formation of oxygen vacancies. Generally, the formation of Schottky vacancies consists of the loss of oxygen anions and various kinds of valence changes of B-site cations (Fe and Cr), during which the formation of metallic Fe would occur.

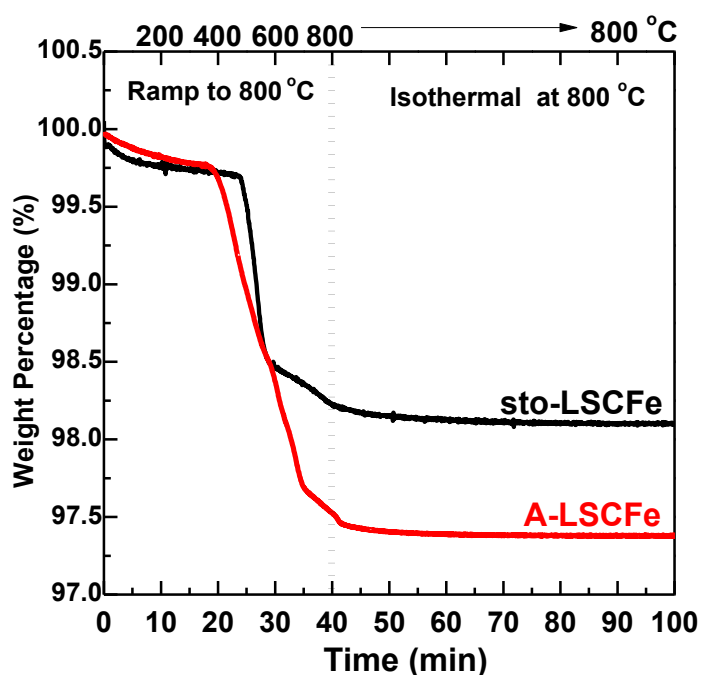


**Fig 7- 3. TGA results of sto-LSCFe and A-LSCFe materials**

As the figure illustrates, both materials have no weight loss during the prolonged stability test, giving the information that the formation of metallic Fe is quite fast, which happens during the ramping process and may be accomplished within a short period of time.

Comparison of SEM images for reduced A-LSCFe and reduced sto-LSCFe is shown in Figure 7-4. Both samples were treated in 5% $H_2$ - $N_2$  at 800 °C for 4 h. The results obviously demonstrate that numerous well dispersed metallic Fe nanoparticles

with uniform diameter of  $\sim 25$  nm were formed on the surface of A-LSCFe. By comparison, only limited Fe particles were produced on the sto-LSCFe, even though the contents of Fe in both samples were the same (15%). The comparison indicates that the introduction of A-site deficiency plays a key role in the exsolution of Fe nanoparticles.

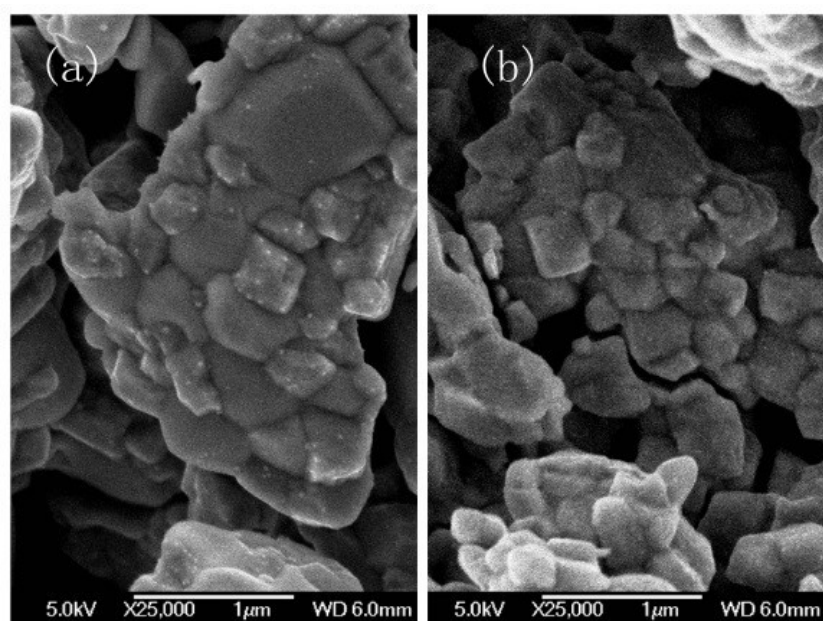


**Fig 7- 4. The comparison of SEM images of (a) reduced A-LSCFe and (b) Sto-LSCFe materials.**

The MWCNTs were prepared by the in-situ decomposition of  $\text{CH}_4$  at  $600$  °C for 4 h over the pre- reduced A-LSCFe and sto-LSCFe materials mentioned above, and the SEM images of the growth of MWCNTs on each material are shown in Figures 7-5(a) and 5(b), respectively. CNTs with crooked and entangled shapes could be found on both materials and all had the length in the order of micro. The morphology of the MWCNTs is similar to those reported elsewhere.(17) After reaction in  $\text{CH}_4$  for 4 h, 1.37 g CNTs were synthesized with 0.5 g A-LSCFe catalyst, compared to 0.43 g CNTs on

0.5 g sto-LSCFe catalysts. Such a difference is consistent with the results of the SEM images in Figure 7-5 in which less CNTs were formed over sto-LSCFe catalyst.

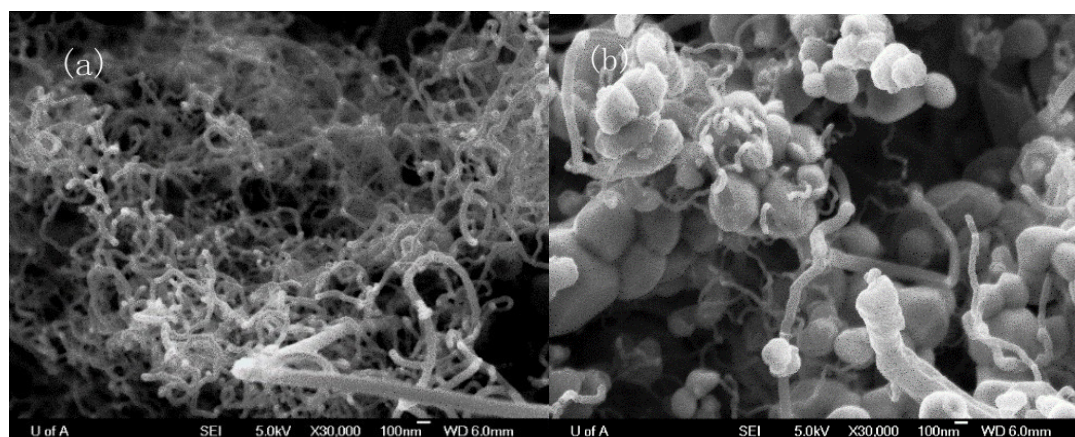
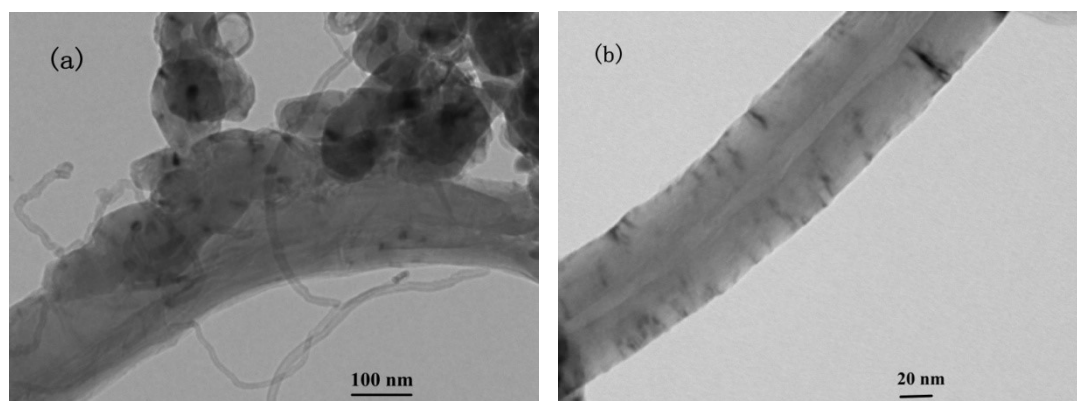


**Fig 7- 5 SEM images of MWCNTs prepared by decomposition of CH<sub>4</sub> at 600 °C for 4h over pre-reduced (a) A-LSCFe and (b) sto-LSCFe.**

TEM images for MWCNTs over A-LSCFe catalysts are shown in Figure 7-6. Figure 7-6a indicates that many rope structure carbon nanotubes with outer diameters ranging from 10 to 40 nm were detected. Figure 7-6b shows a tubular segment of a MWCNT whereas Figure 7-6c depicts a closer view of a ~25 nm Fe nanoparticle [indicated by EDX analysis in Figure 7-6c located at the end of a MWCNT and encapsulated within the nanotube, which is consistent with a tip growth mechanism for CNTs.(18) It is worth noting, in Figure 7-6d, that the growth direction of graphene layers is almost parallel to the tube axial direction. The average spacing between two parallel layers is about 0.33 nm, which agrees well with the (002) plane lattice parameter of CNTs.

The I-V and power density curves (after current-resistance (IR) compensation) for fuel cells with various anode catalysts and temperatures in H<sub>2</sub> are shown in Figure 7-

7a. The fuel cell with an A-LSCFe anode can generate the maximum power density of  $\sim 430 \text{ mW cm}^{-2}$  which is about 1.4 times the value for cell with a sto-LSCFe anode. Similar performance difference could also be detected when the anode of the cell was exposed to methane. The fuel cell with an A-LSCFe anode in methane exhibited the maximum power density of around  $300 \text{ mW/cm}^2$  at  $800 \text{ }^\circ\text{C}$  (shown in Figure 7-7(b)), which was more than one and a half times higher than that of the cell with sto-LSCFe. The performance illustrates that the introduction of A-site deficiency into a perovskite anode could significantly facilitate its electrochemical performance. The I-V and power density curves for a fuel cell with an A-LSCFe anode in  $\text{H}_2$  at different temperature are shown in Figure 7-7c. As the temperature increased from  $700 \text{ }^\circ\text{C}$  to  $800 \text{ }^\circ\text{C}$ , the maximum current density and power density of the cell increased from  $\sim 380 \text{ mA cm}^{-2}$  to  $1080 \text{ mA cm}^{-2}$  and  $\sim 210 \text{ mW cm}^{-2}$  to  $\sim 430 \text{ mW cm}^{-2}$ , respectively.



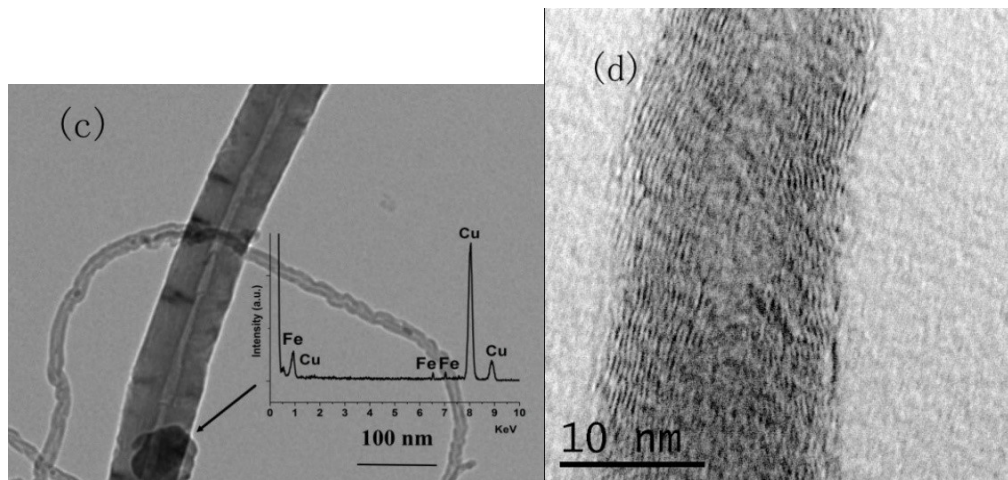


**Fig 7- 6 TEM images of (a) CNTs with different diameters, (b) segment of a CNT, (c) Fe nano particle encapsulated within a CNT as well as its corresponding EDX scan results, and (d) CNTs composed of well graphitized layers.**

The I-V and power density curves for the cell with an A-LSCFe anode with different treatments are shown in Figure 7-7d. The fuel cell with an A-LSCFe anode was in-situ exposed to 5% H<sub>2</sub>/N<sub>2</sub> for 4 h at 800 °C for the in-situ growth of nano Fe particles. After that, the temperature of the operating system was reduced to 700 °C and the fuel was switched back to pure H<sub>2</sub>. It can be found in the figure that the in-situ exsolution of nano Fe particles promotes the electrochemical performance with the maximum power density of ~330 mW cm<sup>-2</sup>, compared to the value of 210 mW cm<sup>-2</sup> (shown in Figure 7-7c) of the cell without this treatment. After that, the cells were further in-situ treated at 600 °C for 4 h with CH<sub>4</sub> which provided the carbon resource for the growth of MWCNTs. After the treatment, the fuel was switched back to pure H<sub>2</sub>. It can be seen from Figure 7-4c that the maximum powder density increased to ~460 mW cm<sup>-2</sup>, almost 1.4 times higher than that of the cell without growth of the MWCNTs.

The treatment dependence of the electrochemical properties of various composites was measured by electrochemical impedance spectroscopy (EIS) technology in H<sub>2</sub> atmosphere and the results are shown in Figure 7-7e. The best fitting results to the equivalent circuit of LR<sub>Ω</sub>(R<sub>1</sub>Q<sub>1</sub>)(R<sub>2</sub>Q<sub>2</sub>) for all the EIS have been obtained where R<sub>Ω</sub> represents the pure ohmic resistance. Each of the parallel circuits of resistance R<sub>i</sub> and constant phase element Q<sub>i</sub> accounts for the respective depressed semicircle going from high to low frequencies. A parasitic inductance L was added to take into account the contribution of the equipment. This fitting result reveals that two different electrode processes (R<sub>1</sub> and R<sub>2</sub>) corresponding to high and low-frequency arcs control the electrochemical reaction. The value of total activation polarization resistance (APR) can be approximately calculated taking into account the difference between the low frequency and the high-frequency intercepts on the real axis of the impedance (Z'). It can be found from the figure that the treatment exhibited no influence on ohmic resistance of the cell (~ 0.55 Ω cm<sup>2</sup>). However, the activation polarization resistance dropped from ~1.8 Ω cm<sup>2</sup> to ~1.2 Ω cm<sup>2</sup>, suggesting that the exsolution of nano iron particles (shown in SEM images) provided more active sites for the oxidation reaction of H<sub>2</sub>.

After introducing CH<sub>4</sub> for 4 h at 600 °C, the growth of MWCNTs could be detected. It can be seen that the MWCNTs showed enhancing effect on cell performance, which results in a further decrease of activation polarization from ~1.2 Ω cm<sup>2</sup> to ~0.85 Ω cm<sup>2</sup>. Previous study in the literature ascribed the phenomenon of R<sub>1</sub> to charge transfer and

that of  $R_2$  to concentration polarization(19). After the decoration of CNTs, the value of  $R_1$  decreased from  $0.35 \Omega \text{ cm}^2$  to  $0.15 \Omega \text{ cm}^2$ . Meanwhile, the value of  $R_2$  declined from  $0.85 \Omega \text{ cm}^2$  to  $0.7 \Omega \text{ cm}^2$ . Consequently, it can be speculated that the enhancing effect of CNTs is mainly due to the excellent conductivity of CNTs which facilitates electron transport during the reaction. The increasing charge transfer efficiency further promoted the mass transfer phenomenon.

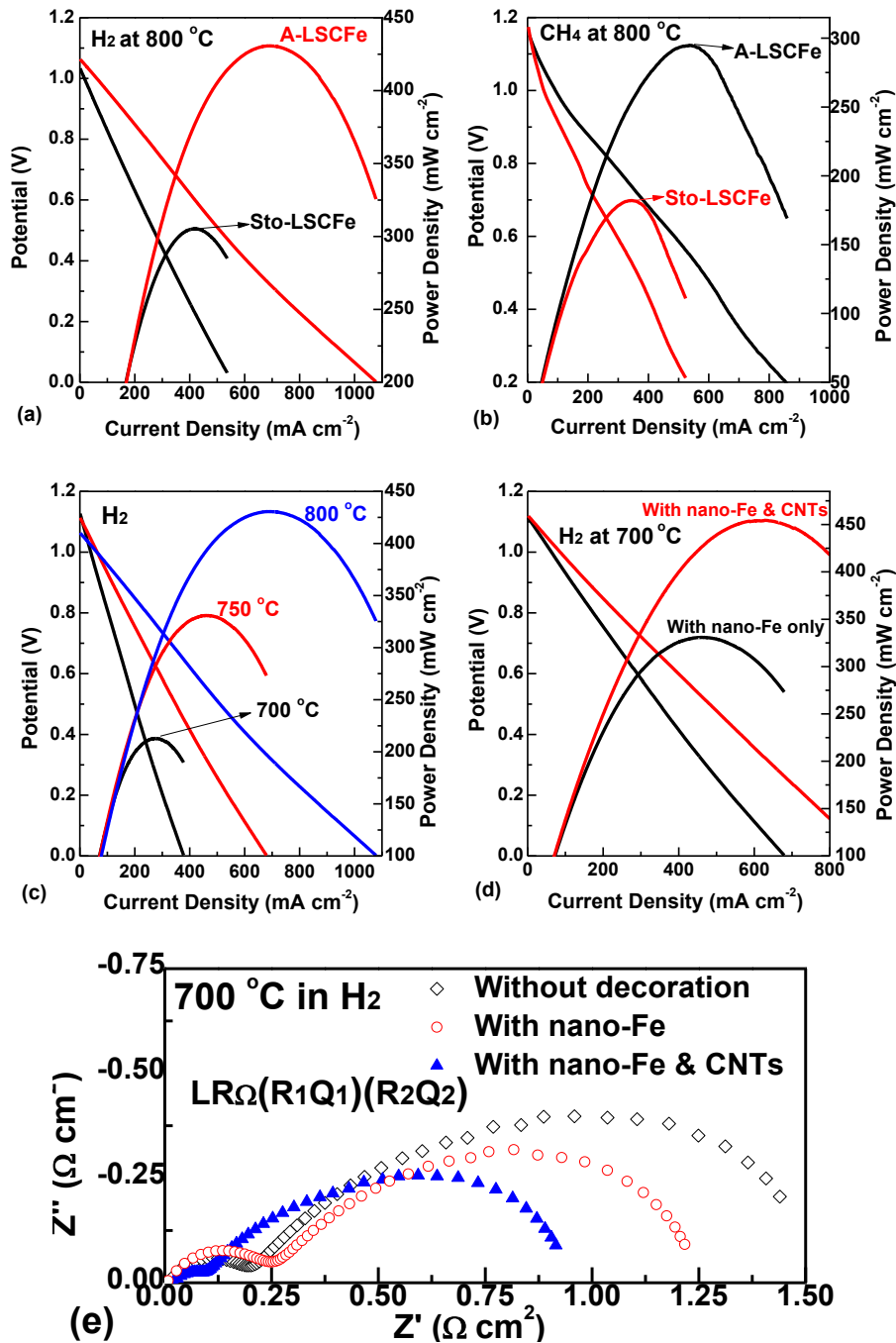


**Fig 7- 7 The I-V and power density curve of fuel cells with A-LSCFe and sto-LSCFe anodes in H<sub>2</sub> (a) and in CH<sub>4</sub> (b) at 800 °C, (c) with A-LSCFe anode fed with H<sub>2</sub> at different temperatures, (d) with A-LSCFe anode with and without CNT in H<sub>2</sub> at 700 °C, and (e) The corresponding EIS of the fuel cells with different treatments.**

## 7.4 Conclusions

In conclusion, we have developed functional A-site deficient LSCFe perovskite materials which can be utilized as anode materials for SOFCs. It can also act as the catalyst at the same time for the growth of MWCNTs. Compared to the sto-LSFC, the introduction of A-site deficiency in A-LSCFe facilitated the in-situ exsolution of iron nano particles which provided more active sites for both the fuel oxidation reaction for SOFCs and for the growth of MWCNTs. The carbon nanotubes can be produced in-situ and can promote the electrochemical performance of the cell. The superior conductivity of MWCNTs makes themselves a type of promising promoter for diverse energy storage devices.

## 7.5 References

1. He H, Hill JM. Carbon deposition on Ni/YSZ composites exposed to humidified methane. *Applied Catalysis A: General*. 2007;317(2):284-92.
2. Atkinson A, Barnett S, Gorte RJ, Irvine JTS, McEvoy AJ, Mogensen M, et al. Advanced anodes for high-temperature fuel cells. *Nat Mater*. 2004;3(1):17-27.
3. Huang B, Ye XF, Wang SR, Nie HW, Shi J, Hu Q, et al. Performance of Ni/ScSZ cermet anode modified by coating with Gd<sub>0.2</sub>Ce<sub>0.8</sub>O<sub>2</sub> for an SOFC running on methane fuel. *Journal of Power Sources*. 2006;162(2):1172-81.
4. Liu C, Li F, Ma L-P, Cheng H-M. Advanced Materials for Energy Storage. *Advanced Materials*. 2010;22(8):E28-E62.
5. Brandon NP, Skinner S, Steele BCH. RECENT ADVANCES IN MATERIALS FOR FUEL CELLS. *Annual Review of Materials Research*. 2003;33(1):183-213.
6. Zhang J, Liu X, Blume R, Zhang A, Schlögl R, Su DS. Surface-Modified Carbon Nanotubes Catalyze Oxidative Dehydrogenation of n-Butane. *Science*. 2008;322(5898):73-7.
7. Zhang W, Sherrell P, Minett AI, Razal JM, Chen J. Carbon nanotube architectures as catalyst supports for proton exchange membrane fuel cells. *Energy & Environmental Science*. 2010;3(9):1286-93.

8. Heresanu V, Castro C, Cambedouzou J, Pinault M, Stephan O, Reynaud C, et al. Nature of the Catalyst Particles in CCVD Synthesis of Multiwalled Carbon Nanotubes Revealed by the Cooling Step Study. *The Journal of Physical Chemistry C*. 2008;112(19):7371-8.
9. Halonen N, Kordás K, Tóth G, Mustonen T, Mäklin J, Vähäkangas J, et al. Controlled CCVD Synthesis of Robust Multiwalled Carbon Nanotube Films. *The Journal of Physical Chemistry C*. 2008;112(17):6723-8.
10. Coquay P, Flahaut E, De Grave E, Peigney A, Vandenberghe RE, Laurent C. Fe/Co Alloys for the Catalytic Chemical Vapor Deposition Synthesis of Single- and Double-Walled Carbon Nanotubes (CNTs). 2. The CNT–Fe/Co–MgAl<sub>2</sub>O<sub>4</sub> System. *The Journal of Physical Chemistry B*. 2005;109(38):17825-30.
11. Rummeli MH, Schäffel F, Kramberger C, Gemming T, Bachmatiuk A, Kalenczuk RJ, et al. Oxide-Driven Carbon Nanotube Growth in Supported Catalyst CVD. *Journal of the American Chemical Society*. 2007;129(51):15772-3.
12. Takagi D, Homma Y, Hibino H, Suzuki S, Kobayashi Y. Single-Walled Carbon Nanotube Growth from Highly Activated Metal Nanoparticles. *Nano Letters*. 2006;6(12):2642-5.
13. Adijanto L, Balaji Padmanabhan V, Kungas R, Gorte RJ, Vohs JM. Transition metal-doped rare earth vanadates: a regenerable catalytic material for SOFC anodes. *Journal of Materials Chemistry*. 2012;22(22):11396-402.

14. Neagu D, Tsekouras G, Miller DN, Menard H, Irvine JT. In situ growth of nanoparticles through control of non-stoichiometry. *Nature chemistry*. 2013;5(11):916-23.
15. Pinedo R, Ruiz de Larramendi I, Jimenez de Aberasturi D, Gil de Muro I, Aguayo AT, Ruiz de Larramendi JI, et al. A straightforward synthesis of carbon nanotube-perovskite composites for solid oxide fuel cells. *Journal of Materials Chemistry*. 2011;21(28):10273-6.
16. Gao W, Li C, Chen H, Wu M, He S, Wei M, et al. Supported nickel-iron nanocomposites as a bifunctional catalyst towards hydrogen generation from  $N_2H_4 \cdot H_2O$ . *Green Chemistry*. 2014;16(3):1560-8.
17. Mordkovich VZ, Dolgova EA, Karaeva AR, Kharitonov DN, Maslov IA, Kamenev AA, et al. Synthesis of carbon nanotubes by catalytic conversion of methane: Competition between active components of catalyst. *Carbon*. 2007;45(1):62-9.
18. Snoeck JW, Froment GF, Fowles M. Filamentous Carbon Formation and Gasification: Thermodynamics, Driving Force, Nucleation, and Steady-State Growth. *Journal of Catalysis*. 1997;169(1):240-9.
19. Vincent AL, Hanifi AR, Luo J-L, Chuang KT, Sanger AR, Etsell TH, et al. Porous YSZ impregnated with  $La_{0.4}Sr_{0.5}Ba_{0.1}TiO_3$  as a possible composite anode for SOFCs fueled with sour feeds. *Journal of Power Sources*. 2012;215(0):301-6.



## **Appendix I :Carbon Deposition and Sulfur Tolerant $\text{La}_{0.4}\text{Sr}_{0.5}\text{Ba}_{0.1}\text{TiO}_3$ - $\text{La}_{0.4}\text{Ce}_{0.6}\text{O}_{1.8}$ Anode Catalysts for Solid Oxide Fuel Cell**

### Introduction

With the continuous exploration and discovery of natural gas reserves worldwide, the solid oxide fuel cell (SOFC) directly using hydrocarbon as feed, rather than expensive  $\text{H}_2$ , has drawn increasing attention in recent years (1-3). The Ni-YSZ cermet is the most widely used anode material which shows excellent electronic conductivity and catalytic activity (4-6). However, many problems with Ni-YSZ cermets remain to be solved before successfully using hydrocarbon from natural gas as fuel in SOFCs. For example, the carbon deposition generated at higher temperature may block the active sites and reduce the length of triple phase boundary (TPB) (7), thus decreasing the performance of the cells significantly(8). Another severe problem from utilizing hydrocarbon feed is the impurities contained in the feed. Even trace amounts of  $\text{H}_2\text{S}$  in the feed may cause serious and irreversible poisoning on the anode catalysts (9). It has been shown that nickel-based cermets will react with  $\text{H}_2\text{S}$  in the feed at the concentration as low as 10 ppm (10), resulting in the formation of irreversible metal sulfide with a concentration of  $\text{H}_2\text{S}$  higher than 100 ppm (11) .

So far, much effort has been dedicated to developing doped perovskite structure ( $ABO_3$ ) materials that can function effectively and stably in a reducing environment. The high capacity of lattice vacancies of these anode materials allows them to have mixed ionic and electronic conductivity (12). Furthermore, the perovskite oxides exhibit promising resistance against carbon deposition and  $H_2S$  (13, 14). So far, La-doped  $SrTiO_3$  (LST) anode materials have been paid much attention because the doping of the higher valence cation of  $La^{3+}$  can facilitate the transport of oxygen ions (15-20), increase the ionic conductivity and improve the fuel cell performance. Previous work done by Adrien et al. (18, 21) in our group showed that the partial substitution of Ba for Sr in LST ( $La_{0.4}Sr_{0.6-x}Ba_xTiO_3$ ,  $0 < x < 0.2$  (LSBT)) prepared by the solid state method (18) could increase its ionic conductivity, catalytic activity towards the oxidation of  $CH_4$  and improve the stability of the LST structure. Besides, the fuel cell performance was significantly enhanced when  $H_2S$  was present in either  $CH_4$  or  $H_2$  fuel.

For the preparation of catalysts, the impregnation or infiltration method has been widely used (22-24). Also, impregnation technology could be regarded as a promising method for fabrication of high performance electrode materials for SOFCs. For example, the performance of LSBT prepared by impregnation was several times higher than that by the solid state method, which exhibited a maximum power density of  $84 \text{ mW/cm}^2$  when the feed was  $CH_4 + 0.5\% H_2S$  (15). Even so, its

electrochemical performance still needs to be further enhanced, and its resistance against carbon deposition is still questionable.

Previous researches have shown that cerium based oxides could be applied as an effective promoter for anode catalysts. The solutions of  $\text{Ce}(\text{NO}_3)_2$  with other metal nitrates could be infiltrated into the porous matrix of the anode through the capillary effect to form doped cerium oxides (25, 26), and the anode performance and its resistance against carbon deposition could thus be enhanced. On one hand, the polarization resistance of a pure LSM electrode in  $\text{H}_2$  at 700 °C could be reduced very significantly from around  $50 \text{ } \Omega \text{ cm}^2$  to less than  $0.21 \text{ } \Omega \text{ cm}^2$  after the impregnation of  $\text{Ce}(\text{NO}_3)_3$  and  $\text{Gd}(\text{NO}_3)_3$  (GDC) solutions to form a LSM/GDC composite (27). Other research showed that the addition of GDC speeded up the process of oxygen diffusion, which reduced the activation energy of the reaction (28). However, not many reports about the promotion effect of GDC on LST-based anodes are available because it will probably introduce a new Ga-rich phase. On the other hand,  $\text{La}_2\text{O}_3$ -doped  $\text{CeO}_2$  (LDC) is a good candidate for improving the anode performance of LST-based anodes (29). It not only shows excellent tolerance to sulfur containing fuel and but also has substantial catalytic activity for fuel oxidation.

In this paper, based on the investigation of our previous work on LSBT based anode materials, we introduce the addition of LDC into the porous YSZ matrix together with the LSBT. The electrochemical performance of this anode catalyst and its resistance against carbon deposition and sulfur were also investigated.

## Experimental Procedures

In order to achieve a high level of porosity, the YSZ powder and 20 wt% polymer microspheres (polymethylmethacrylate, PMMA) (Sigma Aldrich) were thoroughly mixed by ball mill and then sintered at 1350 °C. The final materials had, approximately, 55% porosity. The powder was then mixed with 5 wt% poly solution. The next step was to screen print the paste onto one side of commercial YSZ disks with a thickness of 300 µm and diameter of 25 mm, which were further sintered at 1200 °C for 5 h to form membrane electrode assemblies with circular 1 cm<sup>2</sup> anodes. The LSBT solution was prepared using the procedure demonstrated by Vicent et al (21). Certain amounts of titanium(IV) propoxide (98%, Aldrich) and triethanolamine (Aldrich) (mole ratio of 1:4) were dissolved into an aqueous solution containing the appropriate amounts of lanthanum(III) nitrate hexahydrate (99.999%, Aldrich) and strontium nitrate (Aldrich). LDC solution was prepared by dissolving lanthanum(III) nitrate hexahydrate, ammonium cerium(IV) nitrate (99.99%, Aldrich) and glycine (Aldrich) in 0.2:0.3:1 molar ratio. The total metal ion concentration was 0.5 mol L<sup>-1</sup> for both solutions. After each impregnation step, the cell was decomposed at 400 °C for 4 h. LBST was impregnated three times to form electrodes having 15 wt% deposits. An LDC-LBST sample was prepared by impregnating LDC twice (10 wt%) before LBST (15 wt%). After all the

impregnation processes, the composite lanthanum strontium manganite (LSM) was employed as the cathode prepared by screen printing and sintered at 1200 °C for 1 h. The cells were denoted as LSBT and LSBT-LDC, respectively.

A gas chromatograph (GC) (Agilent 6890N) equipped with a thermal conductivity detector (TCD) and column of Polapak Q ( $3\phi \times 2$  m) was used to analyze the exhausted gases. The Ar was applied as carrier gas for GC. The formation rate ( $r$ ) of carbon was evaluated from the material balance and the formation rates of CO, CO<sub>2</sub>, and H<sub>2</sub>:

$$r(C) = [r(H_2) - 3r(CO) - 4r(CO_2)]/2 \quad (30), \quad \text{Eq (1)}$$

The unit of  $r$  is mmol min<sup>-1</sup>.

The temperature-programmed oxidation (TPO) method was employed to characterize and quantify carbon deposition on the anode materials after various treatments. The samples were put in an alumina tube that was loaded into the TPO apparatus and exposed to a flow of 10% O<sub>2</sub> balanced with He at 50 mL/min for 1 h. The temperature was then increased from room temperature to 850 °C at 20 °C/min and the effluents were analyzed with a mass spectrometer (Thermo star 301). The signals monitored during the TPO experiment included  $m/z = 44$  (CO<sub>2</sub>),  $m/z = 28$  (CO only, excluding the contributions of the residual N<sub>2</sub> and CO<sub>2</sub>),  $m/z = 32$  (O<sub>2</sub>),  $m/z = 18$  (H<sub>2</sub>O),  $m/z = 34$  (H<sub>2</sub>S),  $m/z = 60$  (COS),  $m/z = 64$  (SO<sub>2</sub>) and  $m/z = 76$

(CS<sub>2</sub>). Prior to the TPO analysis, the mass spectrometer signals were calibrated using gas mixtures of known concentrations.

All the samples were treated with H<sub>2</sub>S-CH<sub>4</sub> at 850 °C for 24 h. The heating and cooling processes were done in 10%H<sub>2</sub>-N<sub>2</sub> with a flow rate of 20 mL/min.

## Results and discussion

An SEM image of the cross-section of LSBT-LDC after electrochemical testing is shown in Fig. 1. The electrolyte/electrode can be clearly identified in terms of their different porosities in the corresponding layers. The screen printing technique provided the estimated thickness of about 100 μm for the anode. The good connection at the interface between electrode and electrolyte could be observed and indicated that prolonged period of experiment had little influence on the adhesion and contact between electrolyte and electrode.

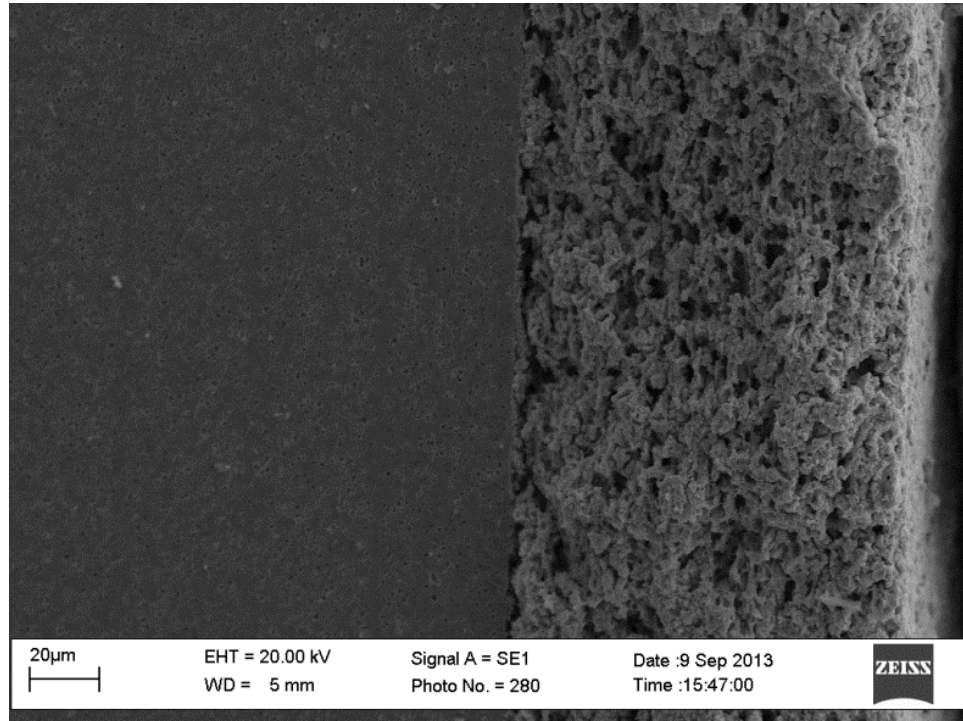


**Fig. 1 Cross-section SEM images of the interfaces of YSZ electrolyte with LSBT-LDC anode.**

To examine the chemical structure of the material, XRD analyses were performed. In Fig. 2, the LSBT showed a single cubic perovskite structure similar to LST with PDF of 35-0734 and no peaks for barium titanate or other impurities could be detected. The XRD results of synthesized LDC in Figure 2(b) exhibit that the structure was related to the cubic fluorite structure of  $\text{CeO}_2$  (PDF 65-2975).

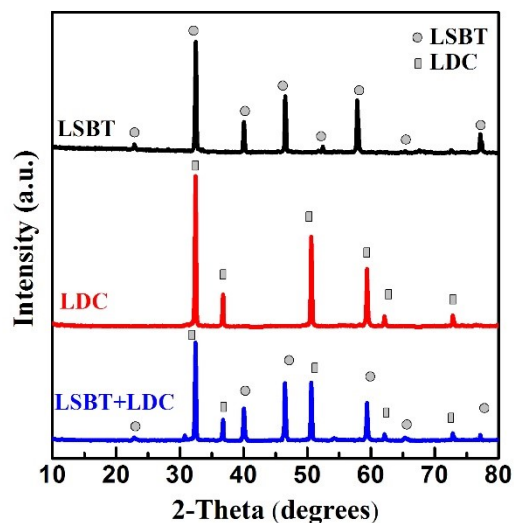


**Fig. 2 XRD patterns of pure LSBT, LDC and mixture of LSBT + LDC materials calcined at 1200 °C for 6 h.**

The electrochemical performances of fuel cells are demonstrated by I-V and powder density curves in Fig. 3(a) and (b). For the cell with LSBT-LDC anode in CH<sub>4</sub>-H<sub>2</sub>S, the data from the Figure 3(a) demonstrated that the maximum power density and current density of the cell were 80 mW cm<sup>-2</sup> and 150 mA cm<sup>-2</sup> at 800 °C, respectively. The maximum power density output and maximum current density increased when the reaction temperature rose from 800 °C to 850 °C. It can be seen from Figure 3(b) that the maximum power density of LSBT was approximately 75 mW cm<sup>-2</sup> at 850 °C in sour fuel while LSBT-LDC more than doubled the value to reach around 160 mW cm<sup>-2</sup>. Similarly, the maximum current density of LSBT was predicted to be 170 mA cm<sup>-2</sup> which was less than half of that of LSBT-LDC (predicted to reach 300 mA cm<sup>-2</sup>). Fig. 4 (a) and (b) show the results of EIS for cells in sour

fuel, and parts of the fitting curves were plotted using hollow patterns. The curves could be divided into two parts: the initial zone where the imaginary part of the impedance is zero was referred to as ohmic resistance and the semi-circular section as activation polarization and transfer of charge. It could be found from Fig. 4 (a) that the ohmic resistance and polarization resistance of the cell decreased as the reaction temperature increased from 800 °C to 850 °C. And the results in Fig. 4 (b) show that the difference in ohmic resistance between LSBT and LSBT-LDC was negligible since both materials had an ohmic resistance of around  $0.3 \Omega/\text{cm}^2$  attributed to the thickness of the electrolyte. Conversely, the difference in polarization resistance between LSBT and LSBT-LDC was apparent. It is known that the activation polarization resistance of LSM-YSZ cathode material was  $< 0.2 \Omega \text{ cm}^2$ , indicating that the polarization arcs were primarily due to anode., the activation polarization resistance of the LSBT-LDC anode catalyst reached around  $9 \Omega \text{ cm}^2$ , while that of LSBT was predicted to be higher than  $14 \Omega \text{ cm}^2$ . With the cathode materials being the same for different cells, it could be inferred that the LSBT-LDC material had better catalytic activity with a lower polarization resistance.

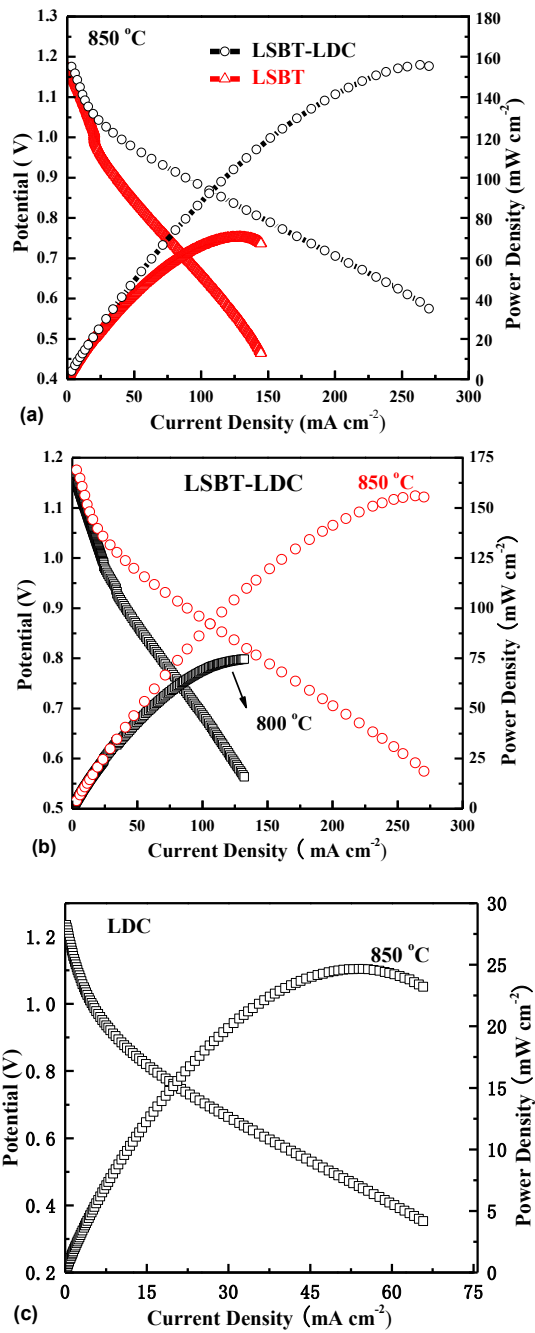


**Fig. 3** The I-V and power density curve of (a) the various cells at  $850\text{ }^{\circ}\text{C}$ ; (b) the cell with LSBT-LDC anode at different reaction temperatures and (c) the cell with LDC anode at  $850\text{ }^{\circ}\text{C}$  in  $\text{H}_2\text{S-CH}_4$ .

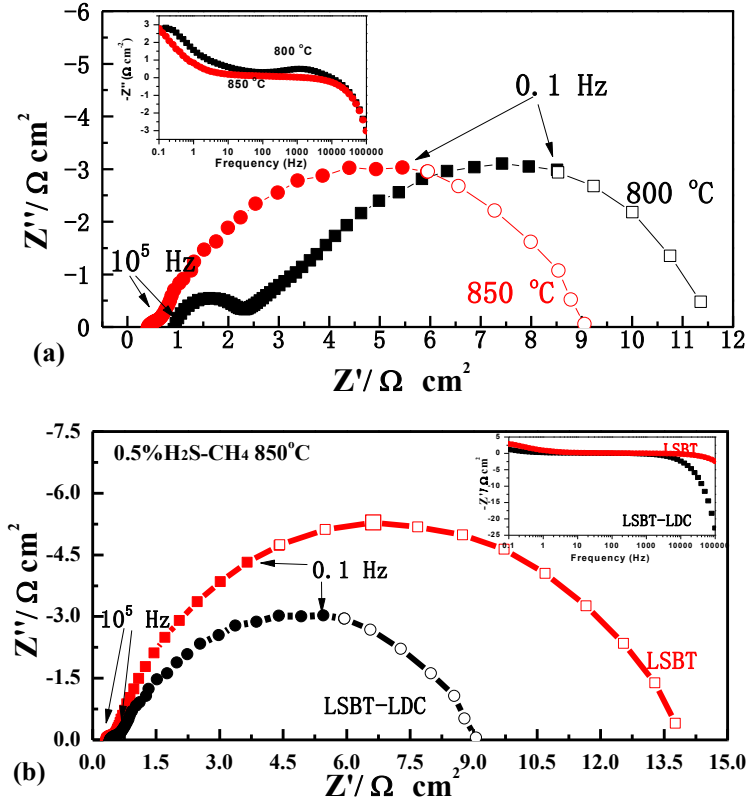


**Fig. 4** The electrochemical impedance spectra of (a) the cell with LSBT-LDC anode at different temperature and (b) the various cells at 850 °C in  $\text{H}_2\text{S}-\text{CH}_4$ .

An electrochemical stability test was performed with the LSBT-LDC cell in  $\text{H}_2\text{S}-\text{CH}_4$  at 850 °C and a potential of 0.65 V for 100 hours (in Fig.5). As shown in the figure, in the 100 hours' stability test, the fuel cell could generate a stable current density of around  $0.23 \text{ A}/\text{cm}^2$  under 0.65V at 850 °C without an obvious current drop, indicating that the LSBT-LDC material has good electrochemical stability under these operating conditions.

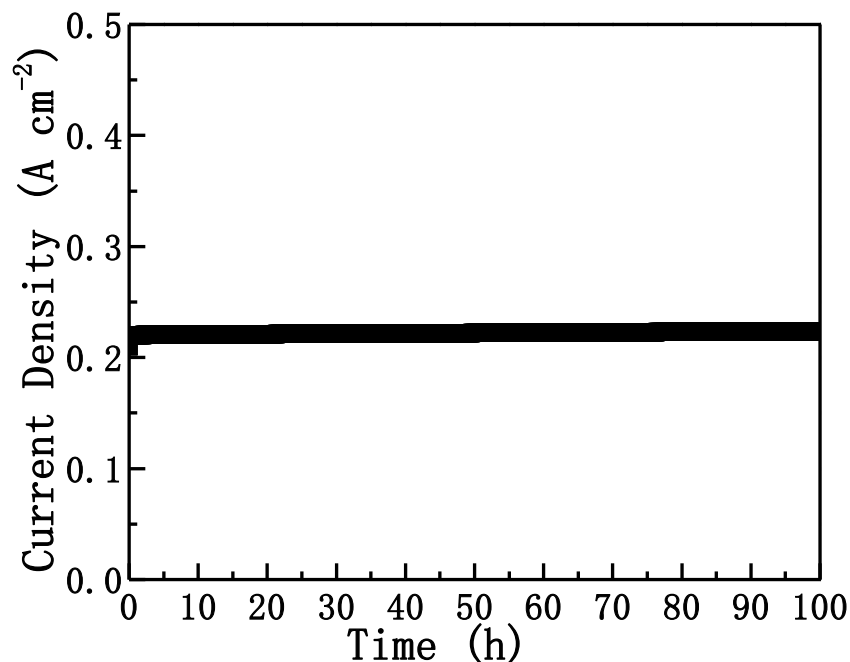


**Fig. 5 The electrochemical stability test of the LSBT-LDC cell in H<sub>2</sub>S-CH<sub>4</sub> at 850 °C at the potential of 0.65 V.**

The line-scan model of EDX shown in Fig .6 was performed to identify the distribution of the impregnated oxides within the porous YSZ framework. The length of the yellow line was 60 μm. The line-scan was not performed in an absolutely vertical direction because it is necessary to avoid the pores in the anode where no element signal could be detected. As shown in the figure, the distribution of each impregnated element was uniform and no element-rich zone could be found. The good distribution of anode catalyst ensured longer TPB, thereby facilitating the electrochemical reaction.

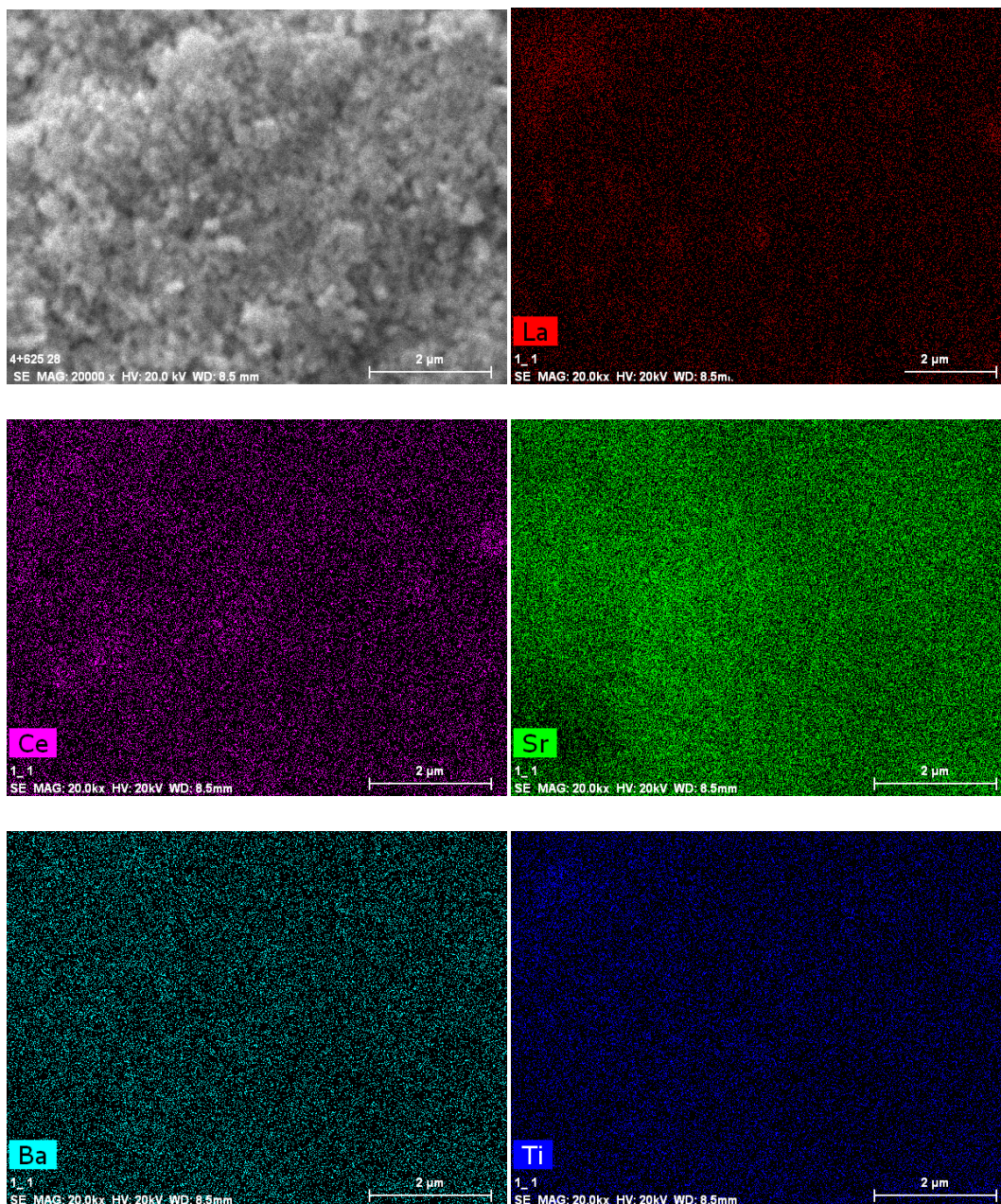


**Fig. 6 SEM image and the corresponding elemental EDX mappings of the LSBT-LDC anode.**

XPS analysis was used to identify the near-surface composition and the ion electronic states of various materials. The data in Table 1 show the atomic concentration of each cation element in the LSBT material. The exact stoichiometry of LSBT materials is almost

equal to the feed ratio, where the concentration of Ba in LST is 6.21%. This result indicates that the doping of Ba in LST is successful and no element loss occurred during the calcination process.

The XPS spectra of C<sub>1s</sub> for CH<sub>4</sub> treated samples (shown in Fig. 7a) had an asymmetric peak located at 284.5 eV with an extended tail at the higher energy region, which could be ascribed to sp<sup>2</sup> hybridized graphite-like carbon(31). By comparing the areas underneath the peaks, we could see that the amount of carbon deposition on LSBT was much larger than that on LSBT-LDC. The expanded region corresponding to sulfur species is shown in Fig. 7b. The sulfur 2p peak of both samples was split with peaks at binding energies of 160.9 eV, 161.5eV, 163.7 eV, 164.8 eV and 168.4 eV. The first two peaks could correspond to TiS<sub>2</sub>(32); the third peak could be elemental sulfur(33) or carbon disulfide(34); the fourth and last peaks may correspond to titanium oxysulfide(35) and sulfate(36), respectively.

Since H<sub>2</sub>S could decompose at high temperature to form H<sub>2</sub> and sulfur, sulfur was inevitably found on the materials surfaces. However, the sulfur adsorbent had no influence on the electrochemical stability of the materials, indicating that the LSBT-LDC has good sulfur tolerance.

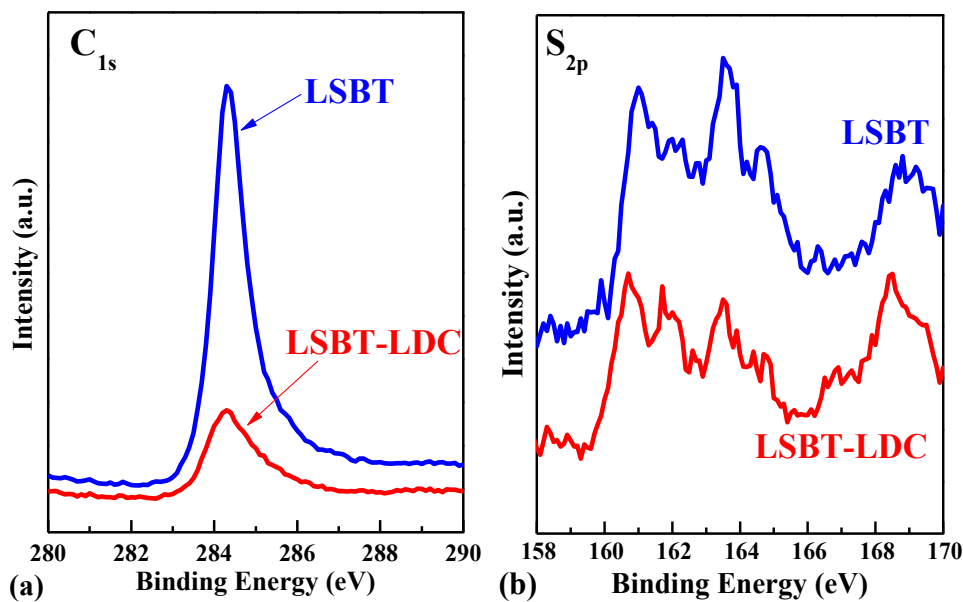


**Fig. 7 XPS spectra of LSBT and LSBT-LDC powders exposed to H<sub>2</sub>S-CH<sub>4</sub> for 24 h at 850 °C in (a) C 1s and (b) S 2p binding energy region.**

Carbon deposition on both anode materials was also examined by the TPO and the results are shown in Fig. 8. For different materials, the temperatures at which the carbon could be removed by an oxidation reaction were different. For LSBT-LDC material, the TPO peak range for CO<sub>2</sub> evolution started from 443 °C and ended at around 577 °C with apparent peaks at 427 °C and 527 °C. For the LSBT material, the high temperature peak shifted to 727 °C, indicating that a larger amount of less reactive carbon was formed on the surface of the anode. From the integration of the curve, it could be seen that the carbon deposition formed on LSBT-LDC was six times more than that on LSBT-LDC. The combination of the results of examination via XPS and TPO provided evidence to prove that the LSBT-LDC had better carbon resistance than LSBT.

In order to further investigate the influence of the addition of LDC on the performance and carbon deposition, the GC was utilized to analyze the composition of effluents of the reactions. Previous research found that only trace amounts of H<sub>2</sub>S could be consumed and it might not function as the fuel(37). 1.0 g anode catalyst was added to a ceramic container placed inside a quartz tubular reactor. The samples were reduced in H<sub>2</sub> for 12 h at 850 °C and atmospheric pressure. The reactor with the reduced sample was purged with helium flow for 30 min and then fed with sour gas (50 mL/min) to start the decomposition of methane. The formation rate could be obtained and the carbon deposits could be determined by the weight gain of the catalyst after reaction.

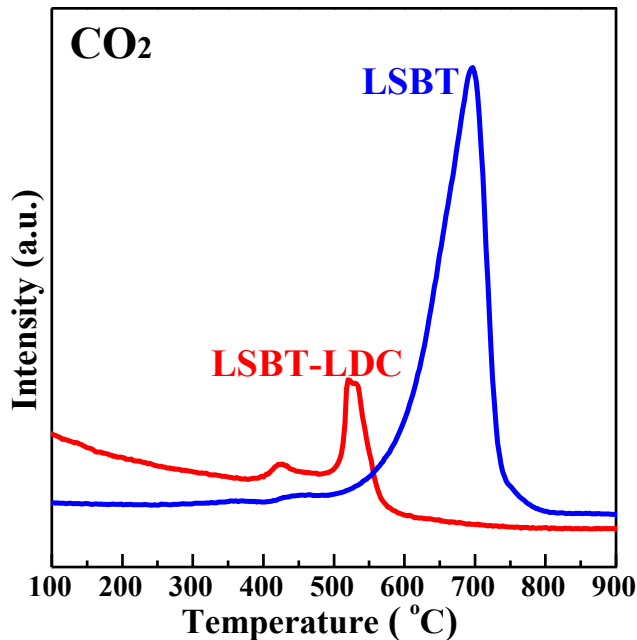
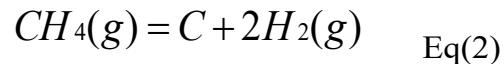


**Fig. 8 CO<sub>2</sub> production during TPO analysis of LSBT-LDC and LSBT materials.**

Fig.9 illustrates how the H<sub>2</sub> formation rates changed with the reaction times for the decomposition of methane at 850 °C. LSBT-LDC had a higher initial formation rate of H<sub>2</sub> and then gradually reached a plateau at a lower level (around 0.13 mmol/min). LSBT, on the other hand, had a lower initial formation rate of H<sub>2</sub>, which descended rapidly during the entire time range and reached its lowest level of approximately 0.04mmol/ml. This difference revealed that the addition of LDC improved the catalytic activity of the anode material in the process of decomposing methane, which may significantly facilitate the next step of the oxidation reaction of methane. According to the reaction below:



The more H<sub>2</sub> was detected, the larger amount of carbon should be deposited on the anode. However, the weight gain of LSBT-LDC after the reaction was measured to be 2.9%, much less than that of LSBT (6.1%). It could be, therefore, deduced that the addition of LDC might not be able to suppress the formation of carbon deposits but instead, it might have helped remove the carbon deposit from the surface of anode after its formation.

In the actual electrochemical reaction on the anode during SOFC operation, the oxygen ions are transferred through the electrolyte to the anode where the oxidation reaction of fuel will occur. Although the addition of LDC could inhibit the carbon deposition and promote the decomposition of methane, it remained unclear if the

inhibit effect was achieved via preventing the activation of C-H bonds for the oxidation reaction. Steam reforming of  $\text{CH}_4$  was, therefore, conducted in order to simulate the real reaction on the anode: a mixture of feed and steam with ratio of 1:1 was introduced as feed at the flow rate of 50 mL/min. Several reactions may take place for the steam reforming of methane and the main products were  $\text{CO}$ ,  $\text{CO}_2$ ,  $\text{H}_2$  and  $\text{C}$ .

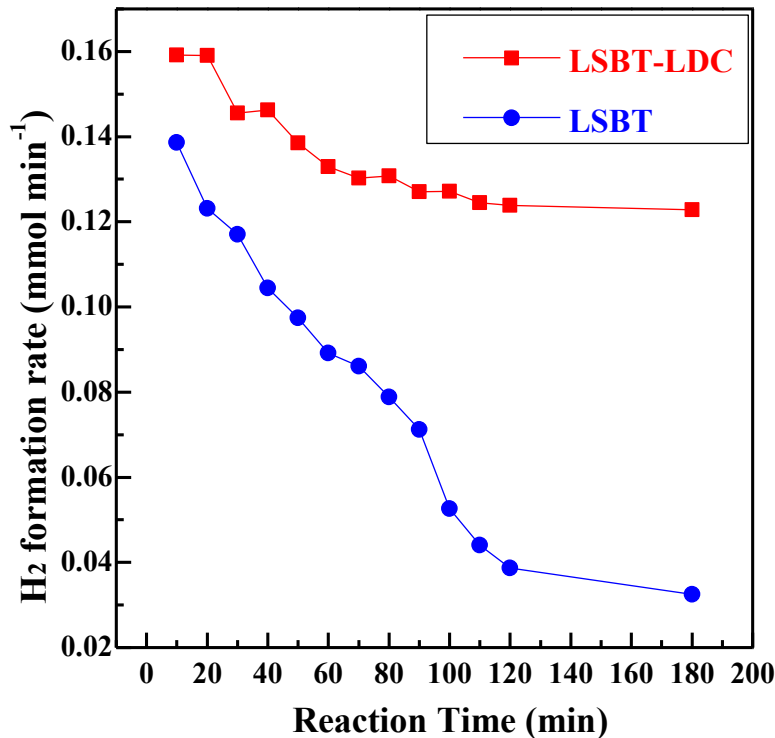


**Fig. 9 Time courses of  $\text{H}_2$  formation rates of different anode catalysts.**

Fig 10 (a) shows the catalytic activation of LSBT anode catalyst to activate C-H bonds in methane for the oxidative reaction. Initially, the formation rate of  $\text{H}_2$  was relatively high at around 0.28 mmol/min and the majority of the products were monoxides with negligible amount of carbon dioxide; the deposited carbon could be

detected at this stage. However, as the reaction proceeded, the formation rate of  $H_2$  decreased sharply to the same level of catalyst in the dry feed. The amount of carbon deposit increased while the formation rate of monoxide dropped to 0.02 mmol/min. This showed that the formation of a carbon deposit might have deactivated the catalyst.

Different results of the LSBT-LDC anode catalyst are shown in Fig.10 (b). The formation rates of all products remained stable at a certain level without obvious fluctuation during the test. The monoxide was the main product while trace amounts of deposited carbon and carbon dioxide were formed. It became evident, based on Fig.10 (a) and (b), that the addition of LDC facilitated the oxidation of methane without forming large amounts of carbon deposit. The LSBT-LDC anode catalyst proved to be able to provide better catalytic activity for the oxidation of methane as well as better resistance to carbon deposit.

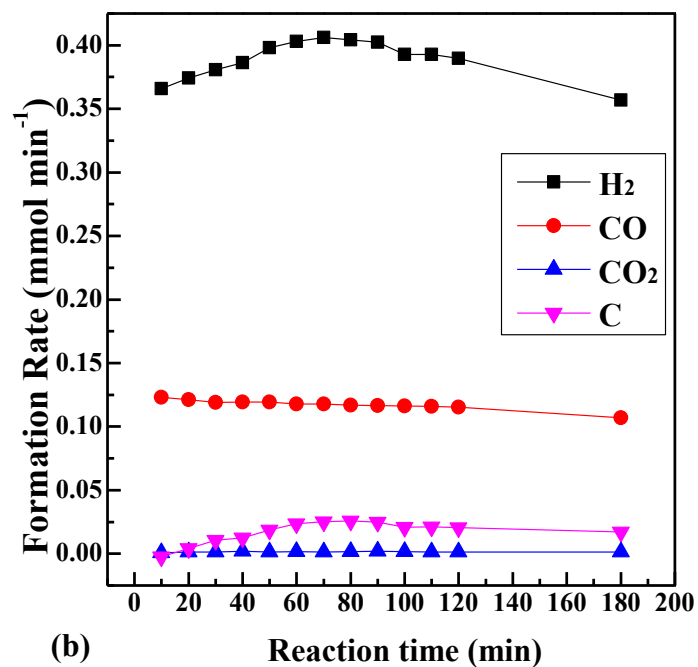
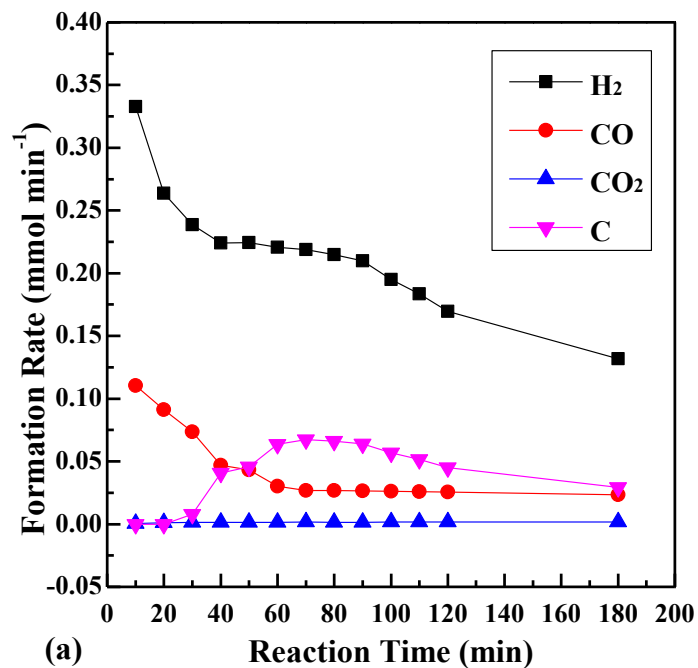


**Fig. 10** Formation rate of all products of the steam reforming reaction of methane on (a) LSBT and (b) LSBT-LDC anode catalysts.

## Conclusions

As a promising anode material, LSBT-LDC was prepared by impregnating LSBT and LDC solutions into a YSZ matrix and its electrochemical performance in sour gas ( $\text{CH}_4+5000\text{ppm H}_2\text{S}$ ) was tested and evaluated. Based on the results from this work, the following conclusions can be drawn:

(1) The better power output could be achieved on LSBT-LDC anode which showed a much smaller activation polarization resistance than a LSBT anode.

(2) The better sulfur tolerance and resistance against carbon deposition of a LSBT-LDC could be proved by the results of XPS and TPO. The results of GC showed that the addition of LDC assisted the activation of methane and the removal of a carbon deposit after its formation on the anode materials.

## References

1. Atkinson A, Barnett S, Gorte RJ, Irvine JT, McEvoy AJ, Mogensen M, et al. Advanced anodes for high-temperature fuel cells. *Nature materials*. 2004;3(1):17-27.
2. Lo Faro M, Antonucci V, Antonucci PL, Aricò AS. Fuel flexibility: A key challenge for SOFC technology. *Fuel*. 2012;102:554-9.
3. Cowin PI, Petit CTG, Lan R, Irvine JTS, Tao S. Recent Progress in the Development of Anode Materials for Solid Oxide Fuel Cells. *Advanced Energy Materials*. 2011;1(3):314-32.
4. Cheng Z, Wang J-H, Choi Y, Yang L, Lin MC, Liu M. From Ni-YSZ to sulfur-tolerant anode materials for SOFCs: electrochemical behavior, in situ characterization, modeling, and future perspectives. *Energy & Environmental Science*. 2011;4(11):4380.
5. Choi S, Wang J, Cheng Z, Liu M. Surface Modification of Ni-YSZ Using Niobium Oxide for Sulfur-Tolerant Anodes in Solid Oxide Fuel Cells. *Journal of The Electrochemical Society*. 2008;155(5):B449.
6. Cheng Z, Liu M. Characterization of sulfur poisoning of Ni-YSZ anodes for solid oxide fuel cells using in situ Raman microspectroscopy. *Solid State Ionics*. 2007;178(13-14):925-35.

7. Chen T, Wang WG, Miao H, Li T, Xu C. Evaluation of carbon deposition behavior on the nickel/yttrium-stabilized zirconia anode-supported fuel cell fueled with simulated syngas. *Journal of Power Sources*. 2011;196(5):2461-8.
8. Gorte RJ, Vohs JM. Catalysis in solid oxide fuel cells. *Annual review of chemical and biomolecular engineering*. 2011;2:9-30.
9. Matsuzaki Y, Yasuda I. The poisoning effect of sulfur-containing impurity gas on a SOFC anode: Part I. Dependence on temperature, time, and impurity concentration. *Solid State Ionics*. 2000;132(3-4):261-9.
10. Rasmussen JFB, Hagen A. The effect of H<sub>2</sub>S on the performance of Ni-YSZ anodes in solid oxide fuel cells. *Journal of Power Sources*. 2009;191(2):534-41.
11. Wang W, Su C, Wu Y, Ran R, Shao Z. Progress in Solid Oxide Fuel Cells with Nickel-Based Anodes Operating on Methane and Related Fuels. *Chemical Reviews*. 2013;113(10):8104-51.
12. Ge X-M, Chan S-H, Liu Q-L, Sun Q. Solid Oxide Fuel Cell Anode Materials for Direct Hydrocarbon Utilization. *Advanced Energy Materials*. 2012;2(10):1156-81.
13. Kee RJ, Zhu H, Goodwin DG. Solid-oxide fuel cells with hydrocarbon fuels. *Proceedings of the Combustion Institute*. 2005;30(2):2379-404.
14. Roushanafshar M, Luo J-L, Vincent AL, Chuang KT, Sanger AR. Effect of hydrogen sulfide inclusion in syngas feed on the electrocatalytic activity of LST-

YDC composite anodes for high temperature SOFC applications. *International Journal of Hydrogen Energy*. 2012;37(9):7762-70.

15. Zhou X, Yan N, Chuang KT, Luo J. Progress in La-doped SrTiO<sub>3</sub> (LST)-based anode materials for solid oxide fuel cells. *RSC Advances*. 2014;4(1):118-31.

16. Vincent AL, Luo J-L, Chuang KT, Sanger AR. Promotion of activation of CH<sub>4</sub> by H<sub>2</sub>S in oxidation of sour gas over sulfur tolerant SOFC anode catalysts. *Applied Catalysis B: Environmental*. 2011.

17. Périllat-Merceroz C, Gauthier G, Roussel P, Huvé M, Gélin P, Vannier R-N. Synthesis and Study of a Ce-Doped La/Sr Titanate for Solid Oxide Fuel Cell Anode Operating Directly on Methane. *Chemistry of Materials*. 2011;23(6):1539-50.

18. Vincent A, Luo J-L, Chuang KT, Sanger AR. Effect of Ba doping on performance of LST as anode in solid oxide fuel cells. *Journal of Power Sources*. 2010;195(3):769-74.

19. Sun X, Wang S, Wang Z, Ye X, Wen T, Huang F. Anode performance of LST-xCeO<sub>2</sub> for solid oxide fuel cells. *Journal of Power Sources*. 2008;183(1):114-7.

20. Canales-Vázquez J, Ruiz-Morales JC, Marrero-López D, Peña-Martínez J, Núñez P, Gómez-Romero P. Fe-substituted (La,Sr)TiO<sub>3</sub> as potential electrodes for symmetrical fuel cells (SFCs). *Journal of Power Sources*. 2007;171(2):552-7.

21. Vincent AL, Hanifi AR, Luo J-L, Chuang KT, Sanger AR, Etsell TH, et al. Porous YSZ impregnated with  $\text{La}_{0.4}\text{Sr}_{0.5}\text{Ba}_{0.1}\text{TiO}_3$  as a possible composite anode for SOFCs fueled with sour feeds. *Journal of Power Sources*. 2012;215(0):301-6.
22. Liu Z, Liu B, Ding D, Liu M, Chen F, Xia C. Fabrication and modification of solid oxide fuel cell anodes via wet impregnation/infiltration technique. *Journal of Power Sources*. 2013;237:243-59.
23. Yun JW, Yoon SP, Han J, Park S, Kim HS, Nam SW. Ceria Coatings Effect on  $\text{H}_2\text{S}$  Poisoning of Ni/YSZ Anodes for Solid Oxide Fuel Cells. *Journal of The Electrochemical Society*. 2010;157(12):B1825.
24. Wang S, Zhong H. High performance Pd promoted  $\text{Sm}_{0.5}\text{Sr}_{0.5}\text{CoO}_3\text{-La}_{0.8}\text{Sr}_{0.2}\text{Ga}_{0.8}\text{Mg}_{0.15}\text{Co}_{0.05}\text{O}_{3-\delta}$  composite cathodes for intermediate temperature solid oxide fuel cells. *Journal of Power Sources*. 2007;165(1):58-64.
25. Jiang SP, Leng YJ, Chan SH, Khor KA. Development of (La, Sr)  $\text{MnO}_3$ -Based Cathodes for Intermediate Temperature Solid Oxide Fuel Cells. *Electrochemical and Solid-State Letters*. 2003;6(4):A67-A70.
26. Uchida H, Arisaka Si, Watanabe M. High Performance Electrode for Medium - Temperature Solid Oxide Fuel Cells  $\text{La}(\text{Sr})\text{CoO}_3$  Cathode with Ceria Interlayer on Zirconia Electrolyte. *Electrochemical and Solid-State Letters*. 1999;2(9):428-30.

27. Jiang SP, Wang W. Fabrication and Performance of GDC-Impregnated (La, Sr) MnO<sub>3</sub> Cathodes for Intermediate Temperature Solid Oxide Fuel Cells. *Journal of The Electrochemical Society*. 2005;152(7):A1398-A408.
28. Steele BCH. Appraisal of Ce<sub>1-y</sub>Gd<sub>y</sub>O<sub>2-y/2</sub> electrolytes for IT-SOFC operation at 500°C. *Solid State Ionics*. 2000;129(1-4):95-110.
29. Zhu XD, Sun KN, Zhang NQ, Chen XB, Wu LJ, Jia DC. Improved electrochemical performance of SrCo<sub>0.8</sub>Fe<sub>0.2</sub>O<sub>3-δ</sub>-La<sub>0.45</sub>Ce<sub>0.55</sub>O<sub>2-δ</sub> composite cathodes for IT-SOFC. *Electrochemistry Communications*. 2007;9(3):431-5.
30. Nabae Y, Yamanaka I, Hatano M, Otsuka K. Mechanism of Suppression of Carbon Deposition on the Pd-Ni/Ce(Sm)O<sub>2</sub>-La(Sr)CrO<sub>3</sub> Anode in Dry CH<sub>4</sub> Fuel. *The Journal of Physical Chemistry C*. 2008;112(27):10308-15.
31. Lee SW, Kim B-S, Chen S, Shao-Horn Y, Hammond PT. Layer-by-Layer Assembly of All Carbon Nanotube Ultrathin Films for Electrochemical Applications. *Journal of the American Chemical Society*. 2008;131(2):671-9.
32. Moreau P, Ouvrard G, Gressier P, Ganal P, Rouxel J. Electronic structures and charge transfer in lithium and mercury intercalated titanium disulfides. *Journal of Physics and Chemistry of Solids*. 1996;57(6-8):1117-22.
33. Kelemen SR, George GN, Gorbaty ML. Direct determination and quantification of sulphur forms in heavy petroleum and coals: 1. The X-ray photoelectron spectroscopy (XPS) approach. *Fuel*. 1990;69(8):939-44.

34. Gelius U, Hedén PF, Hedman J, Lindberg BJ, Manne R, Nordberg R, et al. Molecular Spectroscopy by Means of ESCA III. Carbon compounds. *Physica Scripta*. 1970;2(1-2):70.
35. Gonbeau D, Guimon C, Pfister-Guillouzo G, Levasseur A, Meunier G, Dormoy R. XPS study of thin films of titanium oxysulfides. *Surface Science*. 1991;254(1–3):81-9.
36. Sinharoy S, Wolfe AL. X-ray photoelectron spectra of barium and sulfur in BaS and BaSO<sub>4</sub>. *Journal of Electron Spectroscopy and Related Phenomena*. 1980;18(3):369-71.
37. Roushanafshar M, Luo J-L, Chuang KT, Sanger AR. Effect of Hydrogen Sulfide on Electrochemical Oxidation of Syngas for SOFC Applications. *ECS Transactions*. 2011;35(1):2799-804.

## Bibliography

1. Cowin PI, Petit CTG, Lan R, Irvine JTS, Tao S. Recent Progress in the Development of Anode Materials for Solid Oxide Fuel Cells. *Advanced Energy Materials*. 2011;1(3):314-32.
2. Adams EE. *Carbon Emissions*. Earth Policy Institute. 2013.
3. Ormerod RM. Solid oxide fuel cells. *Chemical Society reviews*. 2003;32(1):17-28.
4. Wang W, Ran R, Su C, Guo Y, Farrusseng D, Shao Z. Ammonia-mediated suppression of coke formation in direct-methane solid oxide fuel cells with nickel-based anodes. *Journal of Power Sources*. 2013;240:232-40.
5. Roushanafshar M, Luo J-L, Chuang KT, Sanger AR. Effect of Hydrogen Sulfide on Electrochemical Oxidation of Syngas for SOFC Applications. *ECS Transactions*. 2011;35(1):2799-804.
6. Services EG. *Fuel Cell Handbook (Fifth Edition)* 2000.
7. Alzate-Restrepo V, Hill JM. Effect of anodic polarization on carbon deposition on Ni/YSZ anodes exposed to methane. *Applied Catalysis A: General*. 2008;342(1-2):49-55.

8. Jung HY, Hong K-S, Jung H-G, Kim H, Kim H-R, Son J-W, et al. SOFCs with Sc-Doped Zirconia Electrolyte and Co-Containing Perovskite Cathodes. *Journal of The Electrochemical Society*. 2007;154(5):B480.
9. Ge X-M, Chan S-H, Liu Q-L, Sun Q. Solid Oxide Fuel Cell Anode Materials for Direct Hydrocarbon Utilization. *Advanced Energy Materials*. 2012;2(10):1156-81.
10. Wang W, Su C, Wu Y, Ran R, Shao Z. Progress in Solid Oxide Fuel Cells with Nickel-Based Anodes Operating on Methane and Related Fuels. *Chemical reviews*. 2013.
11. Mailley SC, Kelaidopoulou A, Siddle A, Dicks AL, Holtappels P, Hatchwell CE, et al. Electrocatalytic activity of a  $\text{Gd}_2\text{Ti}_{0.6}\text{Mo}_{1.2}\text{Sc}_{0.2}\text{O}_{7-\delta}$  anode towards hydrogen and methane electro-oxidation in a solid oxide fuel cell. *Ionics*. 2000;6(5-6):331-9.
12. Hui S, Roller J, Yick S, Zhang X, Decès-Petit C, Xie Y, et al. A brief review of the ionic conductivity enhancement for selected oxide electrolytes. *Journal of Power Sources*. 2007;172(2):493-502.

13. Choi YM, Compson C, Lin MC, Liu M. A mechanistic study of H<sub>2</sub>S decomposition on Ni- and Cu-based anode surfaces in a solid oxide fuel cell. *Chemical Physics Letters*. 2006;421(1–3):179-83.
14. Grgicak CM, Green RG, Du W-F, Giorgi JB. Synthesis and Characterization of NiO-YSZ Anode Materials: Precipitation, Calcination, and the Effects on Sintering. *Journal of the American Ceramic Society*. 2005;88(11):3081-7.
15. Gross MD, Vohs JM, Gorte RJ. A study of thermal stability and methane tolerance of Cu-based SOFC anodes with electrodeposited Co. *Electrochimica Acta*. 2007;52(5):1951-7.
16. Cimenti M, Hill JM. Direct utilization of ethanol on ceria-based anodes for solid oxide fuel cells. *Asia-Pacific Journal of Chemical Engineering*. 2009;4(1):45-54.
17. McIntosh S, Vohs JM, Gorte RJ. Effect of Precious-Metal Dopants on SOFC Anodes for Direct Utilization of Hydrocarbons. *Electrochemical and Solid-State Letters*. 2003;6(11):A240.
18. Aguilar L, Zha S, Cheng Z, Winnick J, Liu M. A solid oxide fuel cell operating on hydrogen sulfide (H<sub>2</sub>S) and sulfur-containing fuels. *Journal of Power Sources*. 2004;135(1–2):17-24.

19. Danilovic N, Luo J-L, Chuang KT, Sanger AR. Effect of substitution with Cr<sup>3+</sup> and addition of Ni on the physical and electrochemical properties of Ce<sub>0.9</sub>Sr<sub>0.1</sub>VO<sub>3</sub> as a H<sub>2</sub>S-active anode for solid oxide fuel cells. *Journal of Power Sources*. 2009;194(1):252-62.
20. Vernoux P, Guillodo M, Fouletier J, Hammou A. Alternative anode material for gradual methane reforming in solid oxide fuel cells. *Solid State Ionics*. 2000;135(1–4):425-31.
21. Marina OA, Canfield NL, Stevenson JW. Thermal, electrical, and electrocatalytical properties of lanthanum-doped strontium titanate. *Solid State Ionics*. 2002;149(1–2):21-8.
22. Sun X-F, Guo R-S, Li J. Preparation and properties of yttrium-doped SrTiO<sub>3</sub> anode materials. *Ceramics International*. 2008;34(1):219-23.
23. Canales-Vázquez J, Ruiz-Morales JC, Marrero-López D, Peña-Martínez J, Núñez P, Gómez-Romero P. Fe-substituted (La,Sr)TiO<sub>3</sub> as potential electrodes for symmetrical fuel cells (SFCs). *Journal of Power Sources*. 2007;171(2):552-7.
24. Tao S, Irvine JTS. Synthesis and Characterization of (La<sub>0.75</sub>Sr<sub>0.25</sub>)Cr<sub>0.5</sub>Mn<sub>0.5</sub>O<sub>3-δ</sub>, a Redox-Stable, Efficient Perovskite Anode for SOFCs. *Journal of The Electrochemical Society*. 2004;151(2):A252.

25. Sauvet A. Catalytic activity for steam methane reforming and physical characterisation of  $\text{La}_{1-x}\text{Sr}_x\text{Cr}_{1-y}\text{Ni}_y\text{O}_{3-\delta}$ . *Solid State Ionics*. 2004;167(1-2):1-8.
26. Primdahl S, Hansen JR, Grahl-Madsen L, Larsen PH. Sr-Doped  $\text{LaCrO}_3$  Anode for Solid Oxide Fuel Cells. *Journal of The Electrochemical Society*. 2001;148(1):A74-A81.
27. Jung S, Lu C, He H, Ahn K, Gorte RJ, Vohs JM. Influence of composition and Cu impregnation method on the performance of  $\text{Cu/CeO}_2/\text{YSZ}$  SOFC anodes. *Journal of Power Sources*. 2006;154(1):42-50.
28. Jin Y, Yasutake H, Yamahara K, Ihara M. Suppressed Carbon Deposition Behavior in Nickel/Yittria-Stablized Zirconia Anode with  $\text{SrZr}_{0.95}\text{Y}_{0.05}\text{O}_{3-\alpha}$  in Dry Methane Fuel. *Journal of The Electrochemical Society*. 2010;157(1):B130.
29. Park CY, Azzarello FV, Jacobson AJ. The oxygen non-stoichiometry and electrical conductivity of  $\text{La}_{0.7}\text{Sr}_{0.3}\text{Cu}_{0.2}\text{Fe}_{0.8}\text{O}_3$  Journal of Materials Chemistry. 2006;16(36):3624.
30. Chen XJ, Khor KA, Chan SH. Suppression of Carbon Deposition at  $\text{CeO}_2$ -Modified Ni/YSZ Anodes in Weakly Humidified  $\text{CH}_4$  at  $850^\circ\text{C}$ . *Electrochemical and Solid-State Letters*. 2005;8(2):A79-A82.

31. Lay E, Benamira M, Pirovano C, Gauthier G, Dessemond L. Effect of Ce-Doping on the Electrical and Electrocatalytical Behavior of La/Sr Chromo-Manganite Perovskite as New SOFC Anode. *Fuel Cells*. 2012;12(2):265-74.
32. Périllat-Merceroz C, Gauthier G, Roussel P, Huvé M, Gélín P, Vannier R-N. Synthesis and Study of a Ce-Doped La/Sr Titanate for Solid Oxide Fuel Cell Anode Operating Directly on Methane. *Chemistry of Materials*. 2011;23(6):1539-50.
33. Shannon RD, Prewitt CT. Effective ionic radii in oxides and fluorides. *Acta Crystallographica Section B*. 1969;25(5):925-46.
34. Levasseur B, Kaliaguine S. Effects of iron and cerium in  $\text{La}_{1-y}\text{Ce}_y\text{Co}_{1-x}\text{Fe}_x\text{O}_3$  perovskites as catalysts for VOC oxidation. *Applied Catalysis B: Environmental*. 2009;88(3-4):305-14.
35. Seiyama T, Yamazoe N, Eguchi K. Characterization and activity of some mixed metal oxide catalysts. *Industrial & Engineering Chemistry Product Research and Development*. 1985;24(1):19-27.
36. Choi H, Fuller A, Davis J, Wielgus C, Ozkan US. Ce-doped strontium cobalt ferrite perovskites as cathode catalysts for solid oxide fuel cells: Effect of dopant concentration. *Applied Catalysis B: Environmental*. 2012;127(0):336-41.

37. Levasseur B, Kaliaguine S. Effect of the rare earth in the perovskite-type mixed oxides  $AMnO_3$  ( $A=Y, La, Pr, Sm, Dy$ ) as catalysts in methanol oxidation. *Journal of Solid State Chemistry*. 2008;181(11):2953-63.
38. Konyshева E, Francis SM, Irvine JTS. Crystal Structure, Oxygen Nonstoichiometry, and Conductivity of Mixed Ionic–Electronic Conducting Perovskite Composites with  $CeO_2$ . *Journal of The Electrochemical Society*. 2010;157(1):B159.
39. Konyshева E, Irvine JTS. Electronic conductivity of modified  $La_{0.95}Ni_{0.6}Fe_{0.4}O_{3-\delta}$  perovskites. *Journal of Power Sources*. 2009;193(1):175-9.
40. Tuller HL, Nowick AS. Defect Structure and Electrical Properties of Nonstoichiometric  $CeO_2$  Single Crystals. *Journal of The Electrochemical Society*. 1979;126(2):209-17.
41. Nielsen J, Hjelm J. Impedance of SOFC electrodes: A review and a comprehensive case study on the impedance of LSM:YSZ cathodes. *Electrochimica Acta*. 2014;115(0):31-45.
42. Tanaka H, Taniguchi M, Uenishi M, Kajita N, Tan I, Nishihata Y, et al. Self-regenerating Rh- and Pt-based perovskite catalysts for automotive-emissions control. *Angewandte Chemie*. 2006;45(36):5998-6002.

43. Nishihata Y, Mizuki J, Akao T, Tanaka H, Uenishi M, Kimura M, et al. Self-regeneration of a Pd-perovskite catalyst for automotive emissions control. *Nature*. 2002;418(6894):164-7.
44. Jiang SP. Nanoscale and nano-structured electrodes of solid oxide fuel cells by infiltration: Advances and challenges. *International Journal of Hydrogen Energy*. 2012;37(1):449-70.
45. Lee S, Kim G, Vohs JM, Gorte RJ. SOFC Anodes Based on Infiltration of  $\text{La}_{0.3}\text{Sr}_{0.7}\text{TiO}_3$ . *Journal of The Electrochemical Society*. 2008;155(11):B1179.
46. Lu J, Fu B, Kung MC, Xiao G, Elam JW, Kung HH, et al. Coking- and sintering-resistant palladium catalysts achieved through atomic layer deposition. *Science*. 2012;335(6073):1205-8.
47. Lintanf A. Pt/YSZ electrochemical catalysts prepared by electrostatic spray deposition for selective catalytic reduction of NO by  $\text{C}_3\text{H}_6$ . *Solid State Ionics*. 2008;178(39-40):1998-2008.
48. Adijanto L, Balaji Padmanabhan V, Kungas R, Gorte RJ, Vohs JM. Transition metal-doped rare earth vanadates: a regenerable catalytic material for SOFC anodes. *Journal of Materials Chemistry*. 2012;22(22):11396-402.

49. Arrivé C, Delahaye T, Joubert O, Gauthier G. Exsolution of nickel nanoparticles at the surface of a conducting titanate as potential hydrogen electrode material for solid oxide electrochemical cells. *Journal of Power Sources*. 2013;223:341-8.
50. Vert VB, Melo FV, Navarrete L, Serra JM. Redox stability and electrochemical study of nickel doped chromites as anodes for H<sub>2</sub>/CH<sub>4</sub>-fueled solid oxide fuel cells. *Applied Catalysis B: Environmental*. 2012;115-116:346-56.
51. Kobsiriphat W, Madsen BD, Wang Y, Shah M, Marks LD, Barnett SA. Nickel- and Ruthenium-Doped Lanthanum Chromite Anodes: Effects of Nanoscale Metal Precipitation on Solid Oxide Fuel Cell Performance. *Journal of The Electrochemical Society*. 2010;157(2):B279.
52. Neagu D, Tsekouras G, Miller DN, Menard H, Irvine JT. In situ growth of nanoparticles through control of non-stoichiometry. *Nature chemistry*. 2013;5(11):916-23.
53. Yaqub A, Janjua NK, Savaniu C, Irvine JTS. Synthesis and characterization of B-site doped La<sub>0.20</sub>Sr<sub>0.25</sub>Ca<sub>0.45</sub>TiO<sub>3</sub> as SOFC anode materials. *International Journal of Hydrogen Energy*. (0).

54. Wang Y, Wang L, Gan N, Lim Z-Y, Wu C, Peng J, et al. Evaluation of Ni/Y<sub>2</sub>O<sub>3</sub>/Al<sub>2</sub>O<sub>3</sub> catalysts for hydrogen production by autothermal reforming of methane. *International Journal of Hydrogen Energy*. 2014;39(21):10971-9.
55. Li W, Reimers JN, Dahn JR. In situ x-ray diffraction and electrochemical studies of Li<sub>1-x</sub>NiO<sub>2</sub>. *Solid State Ionics*. 1993;67(1-2):123-30.
56. Jahangiri A, Aghabozorg H, Pahlavanzadeh H. Effects of Fe substitutions by Ni in La-Ni-O perovskite-type oxides in reforming of methane with CO<sub>2</sub> and O<sub>2</sub>. *International Journal of Hydrogen Energy*. 2013;38(25):10407-16.
57. Rida K, Peña MA, Sastre E, Martinez-Arias A. Effect of calcination temperature on structural properties and catalytic activity in oxidation reactions of LaNiO<sub>3</sub> perovskite prepared by Pechini method. *Journal of Rare Earths*. 2012;30(3):210-6.
58. Cui S-H, Li J-H, Zhou X-W, Wang G-Y, Luo J-L, Chuang KT, et al. Cobalt doped LaSrTiO<sub>3-δ</sub> as an anode catalyst: effect of Co nanoparticle precipitation on SOFCs operating on H<sub>2</sub>S-containing hydrogen. *Journal of Materials Chemistry A*. 2013;1(34):9689.
59. Roushanafshar M, Luo J-L, Vincent AL, Chuang KT, Sanger AR. Effect of hydrogen sulfide inclusion in syngas feed on the electrocatalytic activity of LST-

YDC composite anodes for high temperature SOFC applications. *International Journal of Hydrogen Energy*. 2012;37(9):7762-70.

60. Li J-H, Fu X-Z, Luo J-L, Chuang KT, Sanger AR. Application of BaTiO<sub>3</sub> as anode materials for H<sub>2</sub>S-containing CH<sub>4</sub> fueled solid oxide fuel cells. *Journal of Power Sources*. 2012;213:69-77.

61. Ettler M, Timmermann H, Malzbender J, Weber A, Menzler NH. Durability of Ni anodes during reoxidation cycles. *Journal of Power Sources*. 2010;195(17):5452-67.

62. Wang J-H, Liu M. Surface regeneration of sulfur-poisoned Ni surfaces under SOFC operation conditions predicted by first-principles-based thermodynamic calculations. *Journal of Power Sources*. 2008;176(1):23-30.

63. Sauvet AL, Irvine JTS. Catalytic activity for steam methane reforming and physical characterisation of La<sub>1-x</sub>Sr<sub>x</sub>Cr<sub>1-y</sub>Ni<sub>y</sub>O<sub>3-δ</sub>. *Solid State Ionics*. 2004;167(1-2):1-8.

64. Neagu D, Irvine JTS. Enhancing Electronic Conductivity in Strontium Titanates through Correlated A and B-Site Doping. *Chemistry of Materials*. 2011;23(6):1607-17.

65. Tanaka H, Taniguchi M, Uenishi M, Kajita N, Tan I, Nishihata Y, et al. Self-Regenerating Rh- and Pt-Based Perovskite Catalysts for Automotive-Emissions Control. *Angewandte Chemie International Edition*. 2006;45(36):5998-6002.
66. Bierschenk DM, Potter-Nelson E, Hoel C, Liao Y, Marks L, Poepelmeier KR, et al. Pd-substituted  $(\text{La,Sr})\text{CrO}_{3-\delta}\text{-Ce}_{0.9}\text{Gd}_{0.1}\text{O}_{2-\delta}$  solid oxide fuel cell anodes exhibiting regenerative behavior. *Journal of Power Sources*. 2011;196(6):3089-94.
67. Kitla A, Safonova OV, Föttinger K. Infrared Studies on Bimetallic Copper/Nickel Catalysts Supported on Zirconia and Ceria/Zirconia. *Catal Letters*. 2013;143(6):517-30.
68. Gonzalez-delaCruz VM, Pereñíguez R, Ternero F, Holgado JP, Caballero A. In Situ XAS Study of Synergic Effects on Ni-Co/ZrO<sub>2</sub> Methane Reforming Catalysts. *The Journal of Physical Chemistry C*. 2012;116(4):2919-26.
69. Grgicak CM, Pakulska MM, O'Brien JS, Giorgi JB. Synergistic effects of Ni<sub>1-x</sub>Co<sub>x</sub>-YSZ and Ni<sub>1-x</sub>Cu<sub>x</sub>-YSZ alloyed cermet SOFC anodes for oxidation of hydrogen and methane fuels containing H<sub>2</sub>S. *Journal of Power Sources*. 2008;183(1):26-33.
70. Tao F. Synthesis, catalysis, surface chemistry and structure of bimetallic nanocatalysts. *Chemical Society Reviews*. 2012;41(24):7977-9.

71. Lu ZG, Zhu JH, Bi ZH, Lu XC. A Co–Fe alloy as alternative anode for solid oxide fuel cell. *Journal of Power Sources*. 2008;180(1):172-5.
72. Ringuedé A, Labrincha JA, Frade JR. A combustion synthesis method to obtain alternative cermet materials for SOFC anodes. *Solid State Ionics*. 2001;141–142(0):549-57.
73. An W, Gatewood D, Dunlap B, Turner CH. Catalytic activity of bimetallic nickel alloys for solid-oxide fuel cell anode reactions from density-functional theory. *Journal of Power Sources*. 2011;196(10):4724-8.
74. Huang B, Wang SR, Liu RZ, Wen TL. Preparation and performance characterization of the Fe–Ni/ScSZ cermet anode for oxidation of ethanol fuel in SOFCs. *Journal of Power Sources*. 2007;167(2):288-94.
75. Fu CJ, Chan SH, Ge XM, Liu QL, Pasciak G. A promising Ni–Fe bimetallic anode for intermediate-temperature SOFC based on Gd-doped ceria electrolyte. *International Journal of Hydrogen Energy*. 2011;36(21):13727-34.
76. <NI-FE-LSGM.pdf>.
77. Lu XC, Zhu JH, Bi ZH. Fe alloying effect on the performance of the Ni anode in hydrogen fuel. *Solid State Ionics*. 2009;180(2–3):265-70.

78. Kan H, Lee H. Enhanced stability of Ni–Fe/GDC solid oxide fuel cell anodes for dry methane fuel. *Catalysis Communications*. 2010;12(1):36-9.
79. Shi-zhong W, Jie G. High Performance Ni - Fe - Lanthanum Gallate Composite Anodes for Dimethyl Ether Fuel Cells. *Electrochemical and Solid-State Letters*. 2006;9(9):A395-A8.
80. da Paz Fiuza R, Aurélio da Silva M, Boaventura JS. Development of Fe–Ni/YSZ–GDC electrocatalysts for application as SOFC anodes: XRD and TPR characterization and evaluation in the ethanol steam reforming reaction. *International Journal of Hydrogen Energy*. 2010;35(20):11216-28.
81. He H, Hill JM. Carbon deposition on Ni/YSZ composites exposed to humidified methane. *Applied Catalysis A: General*. 2007;317(2):284-92.
82. Atkinson A, Barnett S, Gorte RJ, Irvine JTS, McEvoy AJ, Mogensen M, et al. Advanced anodes for high-temperature fuel cells. *Nat Mater*. 2004;3(1):17-27.
83. Huang B, Ye XF, Wang SR, Nie HW, Shi J, Hu Q, et al. Performance of Ni/ScSZ cermet anode modified by coating with Gd<sub>0.2</sub>Ce<sub>0.8</sub>O<sub>2</sub> for an SOFC running on methane fuel. *Journal of Power Sources*. 2006;162(2):1172-81.
84. Liu C, Li F, Ma L-P, Cheng H-M. Advanced Materials for Energy Storage. *Advanced Materials*. 2010;22(8):E28-E62.

85. Brandon NP, Skinner S, Steele BCH. RECENT ADVANCES IN MATERIALS FOR FUEL CELLS. *Annual Review of Materials Research*. 2003;33(1):183-213.
86. Zhang J, Liu X, Blume R, Zhang A, Schlögl R, Su DS. Surface-Modified Carbon Nanotubes Catalyze Oxidative Dehydrogenation of n-Butane. *Science*. 2008;322(5898):73-7.
87. Zhang W, Sherrell P, Minett AI, Razal JM, Chen J. Carbon nanotube architectures as catalyst supports for proton exchange membrane fuel cells. *Energy & Environmental Science*. 2010;3(9):1286-93.
88. Heresanu V, Castro C, Cambedouzou J, Pinault M, Stephan O, Reynaud C, et al. Nature of the Catalyst Particles in CCVD Synthesis of Multiwalled Carbon Nanotubes Revealed by the Cooling Step Study. *The Journal of Physical Chemistry C*. 2008;112(19):7371-8.
89. Halonen N, Kordás K, Tóth G, Mustonen T, Mäklin J, Vähäkangas J, et al. Controlled CCVD Synthesis of Robust Multiwalled Carbon Nanotube Films. *The Journal of Physical Chemistry C*. 2008;112(17):6723-8.
90. Coquay P, Flahaut E, De Grave E, Peigney A, Vandenberghe RE, Laurent C. Fe/Co Alloys for the Catalytic Chemical Vapor Deposition Synthesis of Single- and

Double-Walled Carbon Nanotubes (CNTs). 2. The CNT–Fe/Co–MgAl<sub>2</sub>O<sub>4</sub> System.

The Journal of Physical Chemistry B. 2005;109(38):17825-30.

91. Rümmeli MH, Schäffel F, Kramberger C, Gemming T, Bachmatiuk A, Kalenczuk RJ, et al. Oxide-Driven Carbon Nanotube Growth in Supported Catalyst CVD. Journal of the American Chemical Society. 2007;129(51):15772-3.

92. Takagi D, Homma Y, Hibino H, Suzuki S, Kobayashi Y. Single-Walled Carbon Nanotube Growth from Highly Activated Metal Nanoparticles. Nano Letters. 2006;6(12):2642-5.

93. Pinedo R, Ruiz de Larramendi I, Jimenez de Aberasturi D, Gil de Muro I, Aguayo AT, Ruiz de Larramendi JI, et al. A straightforward synthesis of carbon nanotube-perovskite composites for solid oxide fuel cells. Journal of Materials Chemistry. 2011;21(28):10273-6.

94. Gao W, Li C, Chen H, Wu M, He S, Wei M, et al. Supported nickel-iron nanocomposites as a bifunctional catalyst towards hydrogen generation from N<sub>2</sub>H<sub>4</sub>[middle dot]H<sub>2</sub>O. Green Chemistry. 2014;16(3):1560-8.

95. Mordkovich VZ, Dolgova EA, Karaeva AR, Kharitonov DN, Maslov IA, Kamenev AA, et al. Synthesis of carbon nanotubes by catalytic conversion of

methane: Competition between active components of catalyst. Carbon. 2007;45(1):62-9.

96. Snoeck JW, Froment GF, Fowles M. Filamentous Carbon Formation and Gasification: Thermodynamics, Driving Force, Nucleation, and Steady-State Growth. Journal of Catalysis. 1997;169(1):240-9.

97. Vincent AL, Hanifi AR, Luo J-L, Chuang KT, Sanger AR, Etsell TH, et al. Porous YSZ impregnated with  $\text{La}_{0.4}\text{Sr}_{0.5}\text{Ba}_{0.1}\text{TiO}_3$  as a possible composite anode for SOFCs fueled with sour feeds. Journal of Power Sources. 2012;215(0):301-6.

98. Atkinson A, Barnett S, Gorte RJ, Irvine JT, McEvoy AJ, Mogensen M, et al. Advanced anodes for high-temperature fuel cells. Nature materials. 2004;3(1):17-27.

99. Lo Faro M, Antonucci V, Antonucci PL, Aricò AS. Fuel flexibility: A key challenge for SOFC technology. Fuel. 2012;102:554-9.

100. Cheng Z, Wang J-H, Choi Y, Yang L, Lin MC, Liu M. From Ni-YSZ to sulfur-tolerant anode materials for SOFCs: electrochemical behavior, in situ characterization, modeling, and future perspectives. Energy & Environmental Science. 2011;4(11):4380.

101. Choi S, Wang J, Cheng Z, Liu M. Surface Modification of Ni-YSZ Using Niobium Oxide for Sulfur-Tolerant Anodes in Solid Oxide Fuel Cells. *Journal of The Electrochemical Society*. 2008;155(5):B449.
102. Cheng Z, Liu M. Characterization of sulfur poisoning of Ni-YSZ anodes for solid oxide fuel cells using in situ Raman microspectroscopy. *Solid State Ionics*. 2007;178(13-14):925-35.
103. Chen T, Wang WG, Miao H, Li T, Xu C. Evaluation of carbon deposition behavior on the nickel/yttrium-stabilized zirconia anode-supported fuel cell fueled with simulated syngas. *Journal of Power Sources*. 2011;196(5):2461-8.
104. Gorte RJ, Vohs JM. Catalysis in solid oxide fuel cells. *Annual review of chemical and biomolecular engineering*. 2011;2:9-30.
105. Matsuzaki Y, Yasuda I. The poisoning effect of sulfur-containing impurity gas on a SOFC anode: Part I. Dependence on temperature, time, and impurity concentration. *Solid State Ionics*. 2000;132(3-4):261-9.
106. Rasmussen JFB, Hagen A. The effect of H<sub>2</sub>S on the performance of Ni-YSZ anodes in solid oxide fuel cells. *Journal of Power Sources*. 2009;191(2):534-41.

107. Wang W, Su C, Wu Y, Ran R, Shao Z. Progress in Solid Oxide Fuel Cells with Nickel-Based Anodes Operating on Methane and Related Fuels. *Chemical Reviews*. 2013;113(10):8104-51.
108. Kee RJ, Zhu H, Goodwin DG. Solid-oxide fuel cells with hydrocarbon fuels. *Proceedings of the Combustion Institute*. 2005;30(2):2379-404.
109. Zhou X, Yan N, Chuang KT, Luo J. Progress in La-doped SrTiO<sub>3</sub> (LST)-based anode materials for solid oxide fuel cells. *RSC Advances*. 2014;4(1):118-31.
110. Vincent AL, Luo J-L, Chuang KT, Sanger AR. Promotion of activation of CH<sub>4</sub> by H<sub>2</sub>S in oxidation of sour gas over sulfur tolerant SOFC anode catalysts. *Applied Catalysis B: Environmental*. 2011.
111. Vincent A, Luo J-L, Chuang KT, Sanger AR. Effect of Ba doping on performance of LST as anode in solid oxide fuel cells. *Journal of Power Sources*. 2010;195(3):769-74.
112. Sun X, Wang S, Wang Z, Ye X, Wen T, Huang F. Anode performance of LST-xCeO<sub>2</sub> for solid oxide fuel cells. *Journal of Power Sources*. 2008;183(1):114-7.

113. Liu Z, Liu B, Ding D, Liu M, Chen F, Xia C. Fabrication and modification of solid oxide fuel cell anodes via wet impregnation/infiltration technique. *Journal of Power Sources*. 2013;237:243-59.
114. Yun JW, Yoon SP, Han J, Park S, Kim HS, Nam SW. Ceria Coatings Effect on H<sub>2</sub>S Poisoning of Ni/YSZ Anodes for Solid Oxide Fuel Cells. *Journal of The Electrochemical Society*. 2010;157(12):B1825.
115. Wang S, Zhong H. High performance Pd promoted Sm<sub>0.5</sub>Sr<sub>0.5</sub>CoO<sub>3</sub>-La<sub>0.8</sub>Sr<sub>0.2</sub>Ga<sub>0.8</sub>Mg<sub>0.15</sub>Co<sub>0.05</sub>O<sub>3-δ</sub> composite cathodes for intermediate temperature solid oxide fuel cells. *Journal of Power Sources*. 2007;165(1):58-64.
116. Jiang SP, Leng YJ, Chan SH, Khor KA. Development of (La, Sr) MnO<sub>3</sub>-Based Cathodes for Intermediate Temperature Solid Oxide Fuel Cells. *Electrochemical and Solid-State Letters*. 2003;6(4):A67-A70.
117. Uchida H, Arisaka Si, Watanabe M. High Performance Electrode for Medium - Temperature Solid Oxide Fuel Cells La ( Sr ) CoO<sub>3</sub> Cathode with Ceria Interlayer on Zirconia Electrolyte. *Electrochemical and Solid-State Letters*. 1999;2(9):428-30.

118. Jiang SP, Wang W. Fabrication and Performance of GDC-Impregnated (La, Sr) MnO<sub>3</sub> Cathodes for Intermediate Temperature Solid Oxide Fuel Cells. *Journal of The Electrochemical Society*. 2005;152(7):A1398-A408.
119. Steele BCH. Appraisal of Ce<sub>1-y</sub>Gd<sub>y</sub>O<sub>2-y/2</sub> electrolytes for IT-SOFC operation at 500°C. *Solid State Ionics*. 2000;129(1-4):95-110.
120. Zhu XD, Sun KN, Zhang NQ, Chen XB, Wu LJ, Jia DC. Improved electrochemical performance of SrCo<sub>0.8</sub>Fe<sub>0.2</sub>O<sub>3-δ</sub>-La<sub>0.45</sub>Ce<sub>0.55</sub>O<sub>2-δ</sub> composite cathodes for IT-SOFC. *Electrochemistry Communications*. 2007;9(3):431-5.
121. Nabaie Y, Yamanaka I, Hatano M, Otsuka K. Mechanism of Suppression of Carbon Deposition on the Pd-Ni/Ce(Sm)O<sub>2</sub>-La(Sr)CrO<sub>3</sub> Anode in Dry CH<sub>4</sub> Fuel. *The Journal of Physical Chemistry C*. 2008;112(27):10308-15.
122. Lee SW, Kim B-S, Chen S, Shao-Horn Y, Hammond PT. Layer-by-Layer Assembly of All Carbon Nanotube Ultrathin Films for Electrochemical Applications. *Journal of the American Chemical Society*. 2008;131(2):671-9.
123. Moreau P, Ouvrard G, Gressier P, Ganal P, Rouxel J. Electronic structures and charge transfer in lithium and mercury intercalated titanium disulfides. *Journal of Physics and Chemistry of Solids*. 1996;57(6-8):1117-22.

124. Kelemen SR, George GN, Gorbaty ML. Direct determination and quantification of sulphur forms in heavy petroleum and coals: 1. The X-ray photoelectron spectroscopy (XPS) approach. *Fuel*. 1990;69(8):939-44.
125. Gelius U, Hedén PF, Hedman J, Lindberg BJ, Manne R, Nordberg R, et al. Molecular Spectroscopy by Means of ESCA III. Carbon compounds. *Physica Scripta*. 1970;2(1-2):70.
126. Gonbeau D, Guimon C, Pfister-Guillouzo G, Levasseur A, Meunier G, Dormoy R. XPS study of thin films of titanium oxysulfides. *Surface Science*. 1991;254(1-3):81-9.
127. Sinharoy S, Wolfe AL. X-ray photoelectron spectra of barium and sulfur in BaS and BaSO<sub>4</sub>. *Journal of Electron Spectroscopy and Related Phenomena*. 1980;18(3):369-71.
128. Atkinson A, Barnett S, Gorte RJ, Irvine JT, McEvoy AJ, Mogensen M, et al. Advanced anodes for high-temperature fuel cells. *Nature materials*. 2004;3(1):17-27.
129. Lo Faro M, Antonucci V, Antonucci PL, Aricò AS. Fuel flexibility: A key challenge for SOFC technology. *Fuel*. 2012;102:554-9.

130. Cowin PI, Petit CTG, Lan R, Irvine JTS, Tao S. Recent Progress in the Development of Anode Materials for Solid Oxide Fuel Cells. *Advanced Energy Materials*. 2011;1(3):314-32.
131. Cheng Z, Wang J-H, Choi Y, Yang L, Lin MC, Liu M. From Ni-YSZ to sulfur-tolerant anode materials for SOFCs: electrochemical behavior, in situ characterization, modeling, and future perspectives. *Energy & Environmental Science*. 2011;4(11):4380.
132. Choi S, Wang J, Cheng Z, Liu M. Surface Modification of Ni-YSZ Using Niobium Oxide for Sulfur-Tolerant Anodes in Solid Oxide Fuel Cells. *Journal of The Electrochemical Society*. 2008;155(5):B449.
133. Cheng Z, Liu M. Characterization of sulfur poisoning of Ni-YSZ anodes for solid oxide fuel cells using in situ Raman microspectroscopy. *Solid State Ionics*. 2007;178(13-14):925-35.
134. Chen T, Wang WG, Miao H, Li T, Xu C. Evaluation of carbon deposition behavior on the nickel/yttrium-stabilized zirconia anode-supported fuel cell fueled with simulated syngas. *Journal of Power Sources*. 2011;196(5):2461-8.
135. Gorte RJ, Vohs JM. Catalysis in solid oxide fuel cells. *Annual review of chemical and biomolecular engineering*. 2011;2:9-30.

136. Matsuzaki Y, Yasuda I. The poisoning effect of sulfur-containing impurity gas on a SOFC anode: Part I. Dependence on temperature, time, and impurity concentration. *Solid State Ionics*. 2000;132(3–4):261-9.
137. Rasmussen JFB, Hagen A. The effect of H<sub>2</sub>S on the performance of Ni–YSZ anodes in solid oxide fuel cells. *Journal of Power Sources*. 2009;191(2):534-41.
138. Wang W, Su C, Wu Y, Ran R, Shao Z. Progress in Solid Oxide Fuel Cells with Nickel-Based Anodes Operating on Methane and Related Fuels. *Chemical Reviews*. 2013;113(10):8104-51.
139. Ge X-M, Chan S-H, Liu Q-L, Sun Q. Solid Oxide Fuel Cell Anode Materials for Direct Hydrocarbon Utilization. *Advanced Energy Materials*. 2012;2(10):1156-81.
140. Kee RJ, Zhu H, Goodwin DG. Solid-oxide fuel cells with hydrocarbon fuels. *Proceedings of the Combustion Institute*. 2005;30(2):2379-404.
141. Roushanafshar M, Luo J-L, Vincent AL, Chuang KT, Sanger AR. Effect of hydrogen sulfide inclusion in syngas feed on the electrocatalytic activity of LST-YDC composite anodes for high temperature SOFC applications. *International Journal of Hydrogen Energy*. 2012;37(9):7762-70.
142. Zhou X, Yan N, Chuang KT, Luo J. Progress in La-doped SrTiO<sub>3</sub> (LST)-based anode materials for solid oxide fuel cells. *RSC Advances*. 2014;4(1):118-31.

143. Vincent AL, Luo J-L, Chuang KT, Sanger AR. Promotion of activation of CH<sub>4</sub> by H<sub>2</sub>S in oxidation of sour gas over sulfur tolerant SOFC anode catalysts. *Applied Catalysis B: Environmental*. 2011.
144. Périllat-Merceroz C, Gauthier G, Roussel P, Huvé M, Gélin P, Vannier R-N. Synthesis and Study of a Ce-Doped La/Sr Titanate for Solid Oxide Fuel Cell Anode Operating Directly on Methane. *Chemistry of Materials*. 2011;23(6):1539-50.
145. Vincent A, Luo J-L, Chuang KT, Sanger AR. Effect of Ba doping on performance of LST as anode in solid oxide fuel cells. *Journal of Power Sources*. 2010;195(3):769-74.
146. Sun X, Wang S, Wang Z, Ye X, Wen T, Huang F. Anode performance of LST-xCeO<sub>2</sub> for solid oxide fuel cells. *Journal of Power Sources*. 2008;183(1):114-7.
147. Canales-Vázquez J, Ruiz-Morales JC, Marrero-López D, Peña-Martínez J, Núñez P, Gómez-Romero P. Fe-substituted (La,Sr)TiO<sub>3</sub> as potential electrodes for symmetrical fuel cells (SFCs). *Journal of Power Sources*. 2007;171(2):552-7.
148. Vincent AL, Hanifi AR, Luo J-L, Chuang KT, Sanger AR, Etsell TH, et al. Porous YSZ impregnated with La<sub>0.4</sub>Sr<sub>0.5</sub>Ba<sub>0.1</sub>TiO<sub>3</sub> as a possible composite anode for SOFCs fueled with sour feeds. *Journal of Power Sources*. 2012;215(0):301-6.

149. Liu Z, Liu B, Ding D, Liu M, Chen F, Xia C. Fabrication and modification of solid oxide fuel cell anodes via wet impregnation/infiltration technique. *Journal of Power Sources*. 2013;237:243-59.
150. Yun JW, Yoon SP, Han J, Park S, Kim HS, Nam SW. Ceria Coatings Effect on H<sub>2</sub>S Poisoning of Ni/YSZ Anodes for Solid Oxide Fuel Cells. *Journal of The Electrochemical Society*. 2010;157(12):B1825.
151. Wang S, Zhong H. High performance Pd promoted Sm<sub>0.5</sub>Sr<sub>0.5</sub>CoO<sub>3</sub>–La<sub>0.8</sub>Sr<sub>0.2</sub>Ga<sub>0.8</sub>Mg<sub>0.15</sub>Co<sub>0.05</sub>O<sub>3</sub>– $\delta$  composite cathodes for intermediate temperature solid oxide fuel cells. *Journal of Power Sources*. 2007;165(1):58-64.
152. Jiang SP, Leng YJ, Chan SH, Khor KA. Development of (La, Sr) MnO<sub>3</sub>-Based Cathodes for Intermediate Temperature Solid Oxide Fuel Cells. *Electrochemical and Solid-State Letters*. 2003;6(4):A67-A70.
153. Uchida H, Arisaka Si, Watanabe M. High Performance Electrode for Medium - Temperature Solid Oxide Fuel Cells La ( Sr ) CoO<sub>3</sub> Cathode with Ceria Interlayer on Zirconia Electrolyte. *Electrochemical and Solid-State Letters*. 1999;2(9):428-30.
154. Jiang SP, Wang W. Fabrication and Performance of GDC-Impregnated (La, Sr) MnO<sub>3</sub> Cathodes for Intermediate Temperature Solid Oxide Fuel Cells. *Journal of The Electrochemical Society*. 2005;152(7):A1398-A408.

155. Steele BCH. Appraisal of  $\text{Ce}_{1-y}\text{Gd}_y\text{O}_{2-y/2}$  electrolytes for IT-SOFC operation at  $500^\circ\text{C}$ . *Solid State Ionics*. 2000;129(1-4):95-110.
156. Zhu XD, Sun KN, Zhang NQ, Chen XB, Wu LJ, Jia DC. Improved electrochemical performance of  $\text{SrCo}_{0.8}\text{Fe}_{0.2}\text{O}_{3-\delta}\text{-La}_{0.45}\text{Ce}_{0.55}\text{O}_{2-\delta}$  composite cathodes for IT-SOFC. *Electrochemistry Communications*. 2007;9(3):431-5.
157. Nabaie Y, Yamanaka I, Hatano M, Otsuka K. Mechanism of Suppression of Carbon Deposition on the Pd-Ni/Ce(Sm) $\text{O}_2\text{-La(Sr)CrO}_3$  Anode in Dry  $\text{CH}_4$  Fuel. *The Journal of Physical Chemistry C*. 2008;112(27):10308-15.
158. Lee SW, Kim B-S, Chen S, Shao-Horn Y, Hammond PT. Layer-by-Layer Assembly of All Carbon Nanotube Ultrathin Films for Electrochemical Applications. *Journal of the American Chemical Society*. 2008;131(2):671-9.
159. Moreau P, Ouvrard G, Gressier P, Ganal P, Rouxel J. Electronic structures and charge transfer in lithium and mercury intercalated titanium disulfides. *Journal of Physics and Chemistry of Solids*. 1996;57(6-8):1117-22.
160. Kelemen SR, George GN, Gorbaty ML. Direct determination and quantification of sulphur forms in heavy petroleum and coals: 1. The X-ray photoelectron spectroscopy (XPS) approach. *Fuel*. 1990;69(8):939-44.
161. Gelius U, Hedén PF, Hedman J, Lindberg BJ, Manne R, Nordberg R, et al. Molecular Spectroscopy by Means of ESCA III. Carbon compounds. *Physica Scripta*. 1970;2(1-2):70.

162. Gonbeau D, Guimon C, Pfister-Guillouzo G, Levasseur A, Meunier G, Dormoy R. XPS study of thin films of titanium oxysulfides. *Surface Science*. 1991;254(1-3):81-9.
163. Sinharoy S, Wolfe AL. X-ray photoelectron spectra of barium and sulfur in BaS and BaSO<sub>4</sub>. *Journal of Electron Spectroscopy and Related Phenomena*. 1980;18(3):369-71.
164. Roushanafshar M, Luo J-L, Chuang KT, Sanger AR. Effect of Hydrogen Sulfide on Electrochemical Oxidation of Syngas for SOFC Applications. *ECS Transactions*. 2011;35(1):2799-804.